Quantitative Poly-energetic Reconstruction Schemes for Single Spectrum CT Scanners

by

Yuan Lin

Department of Physics
Duke University

Date:_____

Approved:

_____
Ehsan Samei, Supervisor

_____
Shailesh Chandrasekharan

_____
James Dobbins

_____
Daniel J. Gauthier

_____
Chris Walter

Dissertation submitted in partial fulfillment of
the requirements for the degree of Doctor
of Philosophy, in the Department of
Physics in the Graduate School
of Duke University

2014

ABSTRACT

Quantitative Poly-energetic Reconstruction Schemes for Single Spectrum CT Scanners

by

Yuan Lin

Department of Physics
Duke University

Date:_____
Approved:

_____
Samei Ehsan, Supervisor

_____
Shailesh Chandrasekharan

_____
James Dobbins

_____
Daniel J. Gauthier

_____
Chris Walter

An abstract of a dissertation submitted in partial
fulfillment of the requirements for the degree
of Doctor of Philosophy in the Department of
Physics in the Graduate School of
Duke University

2014

Abstract

X-ray computed tomography (CT) is a non-destructive medical imaging technique for assessing the cross-sectional images of an object in terms of attenuation. As it is designed based on the physical processes involved in the x-ray and matter interactions, faithfully modeling the physics in the reconstruction procedure can yield accurate attenuation distribution of the scanned object. Otherwise, unrealistic physical assumptions can result in unwanted artifacts in reconstructed images. For example, the current reconstruction algorithms assume the photons emitted by the x-ray source are mono-energetic. This oversimplified physical model neglects the poly-energetic properties of the x-ray source and the nonlinear attenuations of the scanned materials, and results in the well-known beam-hardening artifacts (BHAs). The purpose of this work was to incorporate the poly-energetic nature of the x-ray spectrum and then to eliminate BHAs. By accomplishing this, I can improve the image quality, enable the quantitative reconstruction ability of the single-spectrum CT scanner, and potentially reduce unnecessary radiation dose to patients.

In this thesis, in order to obtain accurate spectrum for poly-energetic reconstruction, I first presented a novel spectral estimation technique, with which spectra across a large range of angular trajectories of the imaging field of view can be estimated with a single phantom and a single axial acquisition. The experimental results with a 16 cm diameter cylindrical phantom (composition: ultra-high-molecular-weight polyethylene [UHMWPE])

on a clinical scanner showed that the averaged absolute mean energy differences and the normalized root mean square differences with respect to the actual spectra across kVp settings (i.e., 80, 100, 120, 140) and angular trajectories were less than 0.61 keV and 3.41%, respectively

With the previous estimation of the x-ray spectra, three poly-energetic reconstruction algorithms are proposed for different clinical applications. The first algorithm (i.e., poly-energetic iterative FBP [piFBP]) can be applied to routine clinical CT exams, as the spectra of the x-ray source and the nonlinear attenuations of diverse body tissues and metal implant materials are incorporated to eliminate BHAs and to reduce metal artifacts. The simulation results showed that the variation range of the relative errors of various tissues across different phantom sizes (i.e., 16, 24, 32, and 40 cm in diameter) and kVp settings (80, 100, 120, 140) were reduced from [-7.5%, 17.5%] for conventional FBP to [-0.1%, 0.1%] for piFBP, while the noise was maintained at the same low level (about [0.3%, 1.7%]).

When iodinated contrast agents are involved and patient motions are not readily correctable (e.g., in myocardial perfusion exam), a second algorithm (i.e., poly-energetic simultaneous algebraic reconstruction technique [pSART]) can be applied to eliminate BHAs and to quantitatively determine the iodine concentrations of blood-iodine mixtures with our new technique. The phantom experiment on a clinical CT scanner indicated that the maximum absolute relative error across material inserts was reduced from 4.1% for conventional simultaneous algebraic reconstruction technique [SART] to 0.4% for pSART.

Extending the work beyond minimizing BHAs, if patient motions are correctable or negligible, a third algorithm (i.e., poly-energetic dynamic perfusion algorithm [pDP]) is developed to retrieve iodine maps of any iodine-tissue mixtures in any perfusion exams, such as breast, lung, or brain perfusion exams. The quantitative results of the simulations with a dynamic anthropomorphic thorax phantom indicated that the maximum error of iodine concentrations can be reduced from 1.1 mg/cc for conventional FBP to less than 0.1 mg/cc for pDP.

Two invention disclosure forms based on the work presented in this thesis have been submitted to Office of Licensing & Ventures of Duke University.

Acknowledgements

Most of all, I would like to express my heartfelt gratitude to my mother (**Hongfang**), father (**Zhihai**), and my wife (**Na**) for the constant support and encouragement. Their support and encouragement made my doctoral study possible.

Besides my family, I would like to acknowledge the advice and guidance of my academic advisor, **Prof. Ehsan Samei**. I thank him for his encouragement, patience, and financial support throughout my doctoral study.

Additionally, I also wish to express my sincere gratitude to my committee members **Prof. Shailesh Chandrasekharan**, **Prof. James Dobbins**, **Prof. Daniel J. Gauthier**, and **Prof. Chris Walter** for their unfailing support in my doctoral study. Their advice on technical matters, encouragement, motivation and constructive criticism are greatly acknowledged.

Finally, many thanks to **Dr. Karl Stierstorfer**, senior scientist at Siemens Healthcare (Forchheim, Germany), for providing the detailed technical information of the Somatom Definition Flash CT scanner (Siemens Healthcare, Germany). The experimental work would not have been possible without the help of **Dr. Juan Carlos Ramirez-Giraldo**, senior scientist at Siemens Medical Solutions (Malvern, PA, USA). I am grateful to **Mr. Tom Milledge**, senior IT analyst at the Scalable Computing Support Center of Duke University, for his technical support of the Blue Devil GPU cluster.

Dedication

献给我的妈妈和爸爸 – **袁红芳**和**林治海**。

To my mother and father - **Hongfang Yuan** and **Zhihai Lin**.

献给我的妻子 – **陈娜**。

To my wife - **Na Chen**.

Contents

List of Tables

List of Figures

List of Symbols

Symbols	Definitions
$\boldsymbol{\mathcal{B}}$	Filtered Backprojection (FBP) operator
E_0	Reference energy, at which the mono-energetic image will be reconstructed
$\boldsymbol{\mathcal{F}}(\boldsymbol{\mathcal{F}_w})$	Logarithmic poly-energetic forward projection operator (with water correction)
I_e	X-ray photon intensity at the *e-th* energy bin
$I(\varepsilon)$	X-ray photon intensity at energy level ε
N	Total number of the voxels in the measured ROI
N_E	Total number of the spectrum energy bins
N_M	Total number of the base materials
N_R	Total number of the x-ray paths from x-ray source to detector modules
N_S	Total number of the spectra
N_V	Total number of the voxels of the volume
$\boldsymbol{S}$	Smoothing operator
T_v	Region type mask of the *v-th* voxel
Y_{rs}	CT Measurement through the *r-th* x-ray with the *s-th* incident spectrum
$\bar{Y}_{rs}$	Estimated measurement through the *r-th* x-ray with the *s-th* incident spectrum
a_{rv}	Contribution of the *v-th* voxel to the *r-th* ray
c_v	Iodine concentration of the *v-th* voxel
e	Index for spectrum energy bins
l_{rm}	Accumulated effective length of the *m-th* material along the *r-th* ray
$l_{mr}^{pre}/l_{mr}^{post}$	Accumulated effective length of the *m-th* material along the *r-th* ray in the pre-/post-contrast phase
m	Index for the base materials
$\bar{\mathbf{p}}^{pre}$ ($\bar{\mathbf{p}}_w^{pre}$)	Column vector of estimated logarithmic poly-energetic measurements (after water correction) in the pre-contrast phase
p_r^{pre}/p_r^{post}	Logarithmic measurement along the *r-th* ray in the pre-/post-contrast phase

$\bar{p}_r^{pre}/\bar{p}_r^{post}$	Estimated logarithmic measurement along the *r-th* ray in the pre-/post-contrast phase
r	Index for the x-ray paths
s	Index for the spectra
t_v	Attenuation coefficient of the *v-th* voxel at reference energy E_0
$\mathbf{t}^{pre}$	Column vector of voxels of the target volume in terms of the attenuation coefficient at ε in the pre-contrast phase
t_v^{pre}/t_v^{post}	Attenuation coefficient of the *v-th* voxel at reference energy E_0 in the pre-/post-contrast phase
t_v^{iodine}	Iodine map in the post-contrast phase
$\tilde{t}_v^{pre}$	Intermediate pre-contrast image obtained by registering t_v^{pre} to t_v^{post}
$\tilde{t}_v^{post}$	Intermediate post-contrast image reconstructed from post-contrast projections as motion correction reference
$t(\vec{x})$	Attenuation coefficient at location $\vec{x}$ at reference energy E_0
v	Index for the voxels
ε	Energy level within the spectrum range
ε_0	Reference energy, at which the mono-energetic image will be reconstructed
μ_m	Attenuation coefficient of the *m-th* base material at reference energy E_0
η_v^b	Beam hardening error to the *v-th* voxel
η_v^n	Noise error to the *v-th* voxel
μ_{me}	Attenuation coefficient of the *m-th* base material at the *e-th* energy bin
$\mu_m(\varepsilon)$	Attenuation coefficient of the *m-th* base material at energy ε
$\mu(\vec{x},\varepsilon)$	Attenuation coefficient at location $\vec{x}$ at reference energy ε
ρ_m	Density of the *m-th* base material
ρ_v	Density of the *v-th* voxel
τ	Attenuation coefficient due to photoelectric effect
σ_{Co}	Attenuation coefficient due to Compton scattering
σ_{Ra}	Attenuation coefficient due to Rayleigh (coherent) scattering

Chapter 1

Introduction

1.1 Computed Tomography and Physics Modeling

In 1895, a German physicist W. C. Röentgen produced and detected electromagnetic radiation in a wavelength range today known as x-rays or Röentgen rays [1,]. Because of this achievement, he was awarded the Nobel Prize in Physics in 1901. After nearly 80 years, G. N. Hounsfield made use of x-ray and designed the first x-ray computed tomography (CT) scanning system, which won him the Nobel Prize in 1979. Since then advances in hardware technology [1], such as slip-ring gantry designs and helical scanning trajectories, has enabled modern day acquisition of an entire volume of CT data in a few seconds.

This evolution of the hardware was paralleled by new developments in image reconstruction algorithms. There is a growing interest in developing new reconstruction algorithms to improve the image quality and reduce x-ray dose by faithfully modeling the physics of the CT scanner system into the reconstruction procedure. Generally, physics models are developed to mitigate four possible causes of image quality loss [3] : blur, Compton scatter, noise, and beam hardening (BH) effect.

1) The loss of the spatial resolution can be caused by several ignored physical aspects of the CT system, such as the finite size of the system components [4] (e.g., the focal spot size, the voxel size, detector size, and x-ray beam width) and the detector properties [5] (e.g.,

crosstalk and afterglow). Recent algorithms can account for the finite size effects and detector properties via new ray-tracing methods (e.g., distance-driven [6] or separable footprint [4] and realistic detector models [5, 7-9].

2) The influence of the Compton scatter has been steadily growing in x-ray CT due to the increase of the detector size [1], which significantly decrease image contrast-to-noise ratio. Compton scatter can be reduced either by scatter reduction techniques and scatter measurement techniques. The former ones can be implemented by judicious selection of imaging geometry (e.g., using long air gaps or anti-scatter grids [10]). The latter ones can be further categorized to measurement-based approaches [11, 12], projection-based approaches [13, 14], and Monte-Carlo-based approaches [15, 16]. With the improvement of computing ability, there is great potential to integrate the Monte-Carlo-based approaches into the iterative reconstruction to quickly estimate the scatter and correct the target volume.

3) Noise models for x-ray CT reconstruction are also important especially for low dose scans. There are numerous sources of noise, such as fluctuations due to x-ray source [17], x-ray photon interactions in the object and detector [2], and electronic circuits [18]. Though the statistical properties of these noise sources are complex, most of the algorithms seem likely to continue using simple approximations [19, 20], such as the Poisson + Gaussian model or the standard Poisson model.

4) One important physics property of the CT scanner that has been largely neglected by the current reconstruction algorithms is the poly-energetic nature of the x-ray spectrum. If not correctly modeled, it can result in strong artifacts known as beam hardening (e.g., cupping or streaking) [1, 21, 22]. In addition, the energy distribution of the x-ray photons has significant influence on the aforementioned physics models (i.e., the physics models of detector, Compton scatter, and noise). Therefore, it is significantly beneficial to model the x-ray spectrum and material attenuations into the reconstruction procedure.

Several approaches have been proposed to incorporate the poly-energetic nature of the spectrum into the CT imaging scheme. However, several issues still limit their application:

1) There is no convenient method to accurately estimate or to routinely calibrate the x-ray spectrum across angular trajectories of the imaging field of view.
2) The linearization approaches [1, 23-28] are fast, but can only reduce visible artifacts and have limited quantitative reconstruction abilities.
3) The iterative base material approaches [19, 29-32] are only accurate for limited base materials (e.g., water and bone), and they cannot be widely used in clinical practice due to slow computational speed.
4) To retrieve the iodine maps of the perfusion exams, the current reconstruction algorithms [29, 33] are limited by the segmentation and registration techniques.

5) The dual energy approaches [34-36] are fast and accurate but the sophisticated hardware and cost limit their applications.

In view of the importance of modeling spectrum in reconstruction and the limitations of the current poly-energetic approaches, this thesis aims to develop several novel quantitative poly-energetic reconstruction schemes for single spectrum CT scanners to obtain quantitative reconstruction results.

1.2 Organization and Contributions

This chapter discusses the motivation behind this thesis, and concludes with an outline of the organization and contributions of this thesis. Chapter 2 introduces the background knowledge related with this thesis including x-ray computed tomography, x-ray physics, reconstruction algorithm, beam hardening effect, CT applications, and the developed GPU-based simulation platform. The main novel contributions of this thesis lie in Chapters 3-6. The connections between the chapters are illustrated in Figure 1-1. Chapter 3 describes an angle-dependent estimation technique of x-ray spectrum, demonstrating a convenient technique to measure the spectra across the angular trajectories of the CT field of view. A fast poly-energetic iterative FBP (piFBP) is proposed in Chapter 4, which can be applied to general CT exams. For perfusion exams, in order to account for iodine contrast agent, two algorithms (i.e., poly-energetic SART [pSART] and poly-energetic dynamic perfusion algorithm [pDP]) are presented in Chapter 5 and Chapter 6, respectively. If the pre-contrast projections are not available or usable due to uncorrectable patient motions (e.g.,

in myocardial perfusion exam), the former one can be applied to retrieve the iodine concentrations of any iodine-blood mixtures; otherwise, the latter one can be used to take the pre-contrast projections into consideration as prior information to reconstruct the artifact-free iodine map for any iodine-tissue mixtures (e.g., lung, breast, and brain perfusion exams, etc.). Finally, Chapter 7 concludes the thesis with a summary of the accomplished research work and a discussion on the future work.

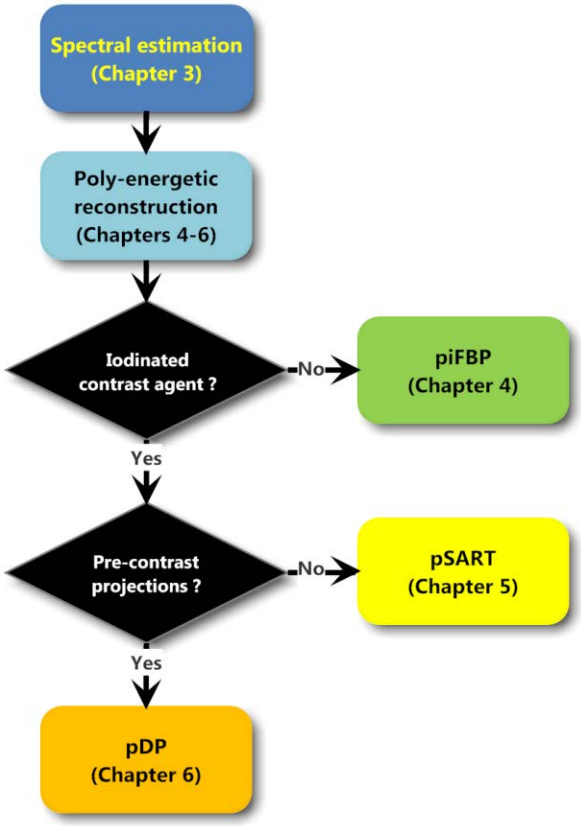

Figure 1-1: Flowchart of the quantitative poly-energetic reconstruction schemes.

Chapter 2

Background

In this chapter, we introduce the necessary background knowledge related to this thesis. In Section 2.1, the basic concept of x-ray computed tomography is presented. In Section 2.2, the x-ray physics including x-ray generation, x-ray interaction with matter, and x-ray detection is discussed. A wildly used reconstruction algorithm (i.e., Filtered Backprojection algorithm) is derived in Section 2.3. The beam hardening effect that is caused by the inconsistency between the poly-energetic nature of the CT system and the mono-energetic nature of the reconstruction algorithms is explained in Section 2.4. Finally, some CT applications are introduced in Section 2.5.

2.1 X-ray Computed Tomography

X-ray computed tomography (CT) is a noninvasive diagnostic imaging technique. This technique involves the acquisition of a series of projection data (called sinogram, Figure 2-1a) using x-rays from different angles. With the aid of a reconstruction algorithm, the sinogram data are reconstructed to yield cross-sectional images of the scanned patient body (Figure 2-1b) for diagnostic purposes.

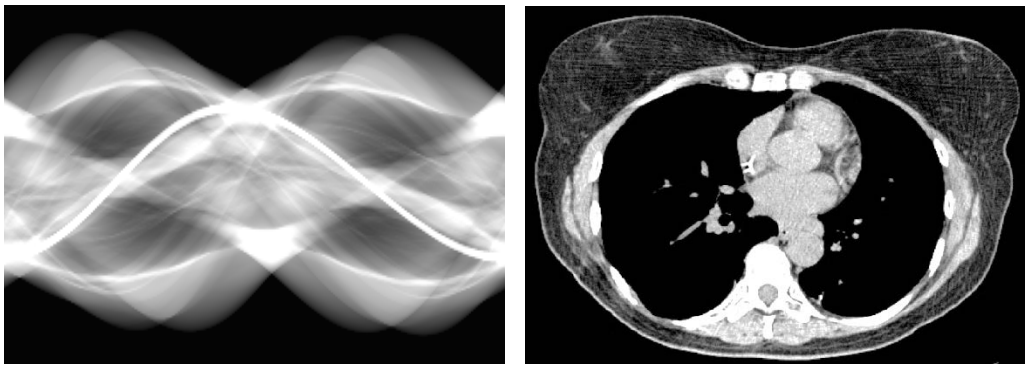

(a) (b)

Figure 2-1: (a) Sinogram, and (b) one slice of the reconstructed cross-sectional images of the scanned patient.

As an x-ray CT scanner is a physical system and it is designed based on x-ray physics including the x-ray generation, x-ray-matter interactions, and x-ray detection (Figure 2-2). Faithfully modeling the x-ray physics into the reconstruction procedure can theoretically yield accurate and reliable images. Therefore, we are going to quickly review the x-ray physics in the following section. As our simulations and experiments were conducted based on the Somatom Definition Flash (SDF) scanner (Siemens Healthcare, Germany) shown in Figure 2-3, some of the unique features of this scanner will also be included.

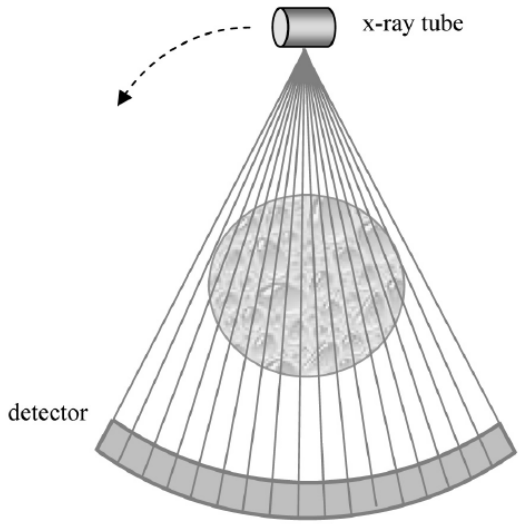

Figure 2-2: CT scanner geometry.

Figure 2-3: Photograph shows Somatom Definition Flash scanner (Siemens Healthcare, Germany).

2.2 X-ray Physics

X-rays are a form of electromagnetic radiation as are radio waves, microwaves, infrared, visible light, and ultraviolet. The wavelength of x-rays ranges from a few

picometers to a few nanometers. The energy E is proportional to the frequency ν of the photons [1]

$$E = h\nu = h\frac{c}{\lambda} = \frac{1.24keV \times nm}{\lambda} \qquad 2\text{-}1$$

where h is Plank's constant (6.63×10^{-34} Js), c is the speed of light in free space (3×10^{8} m/s), and λ is the wavelength of the x-ray radiation. Therefore, x-ray photons with longer wavelengths have lower energies than the photons of shorter wavelengths.

In the following sections, we outline the mechanics that produce x-rays and the types of interactions of the x-rays with matter. The common types of x-ray detectors are also described.

2.2.1 X-ray Generation

As shown in Figure 2-4, a modern x-ray tube consists of a cathode and an anode inside a vacuum tube.

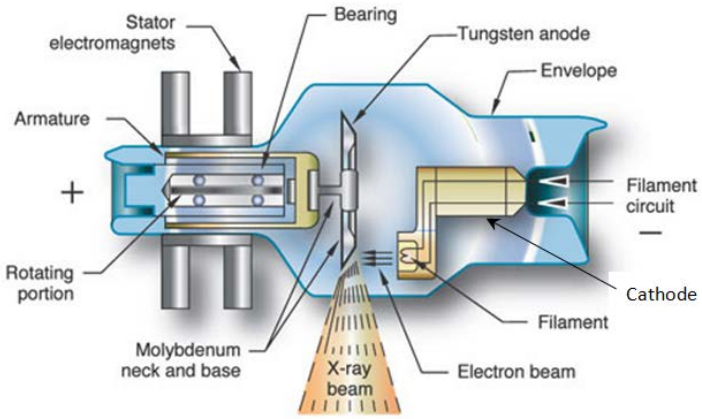

Figure 2-4: Schematic over view of a modern x-ray tube and its components. Source: http://whs.wsd.wednet.edu/faculty/busse/mathhomepage/busseclasses/radiation physics/lecturenotes/chapter6/chapter6.html.

In the x-ray tube, the source of electrons is the cathode, which consists of a helical filament made up of tungsten wire. By the high potential difference between the cathode and anode, the electrons are accelerated across the tube from the filament of the cathode to the target anode. When electrons are retarded by the anode, the strong interactions between electrons and the atoms of anode result in x-ray radiation. The potential difference between the cathode and anode determines the spectrum of the generated x-ray.

The generation process of x-rays is very inefficient, as most of the kinetic energy is converted into heat (over 99%), which can increase the temperature of the target substantially (i.e., 2600℃). To avoid melting the target, high-melting point materials, most commonly tungsten (W, Z=74, melting point 3,422℃), are usually used as the target materials. Besides, the anode rotates at a high speed (3,000 ~ 10,000 rpm) for efficient thermal dissipation.

X-rays produced in an x-ray tube contains two types of radiation, i.e., Bremsstrahlung and Characteristic radiation.

When high-speed electrons are decelerated by atomic nuclei via coulomb's force, partial loss of kinetic energy of the high-speed electrons is converted into photons because of energy conservation. This produced electromagnetic radiation is called Bremsstrahlung radiation.

The energy of the emitted radiation depends on the amount of kinetic energy loss of the electrons. If an electron does not strongly interact with the atomic coulomb field, only low energy bremsstrahlung radiation can be generated. In a rare case, a high-speed electron collides directly with nucleus and all of its kinetic energy is converted to a photon with the highest energy in the bremsstrahlung spectrum. For instance, if an x-ray tube operates at 100 kVp, the highest energy of generated photons is then 100 keV (Figure 2-5 [37]). However, as the chance for this type of interaction is very low, negligible magnitude is observable in the x-ray spectrum at that energy.

The unfiltered bremsstrahlung spectrum presents a ram-shaped relationship between the number and the energy of the x-ray photons. The inherent filtration and bowtie filters gradually remove the lower-energy x-rays, and result in harder x-rays.

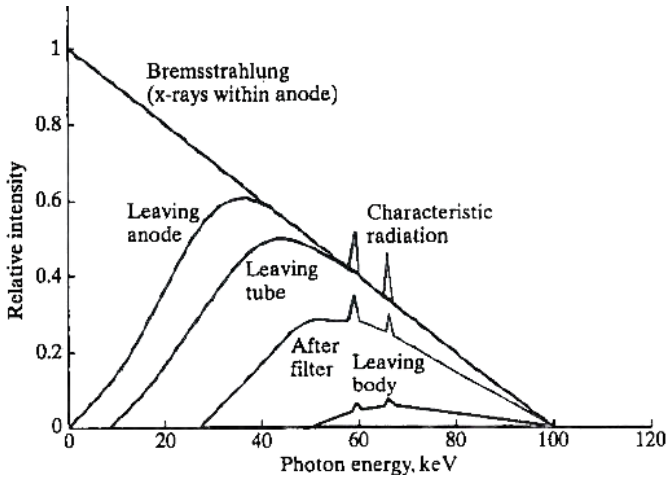

Figure 2-5: The bremsstrahlung energy distribution for a 100 kVp acceleration potential [2].

Another interesting interaction occurs when an electron collides with one of the inner-shell electrons of the target atom (Figure 2-5). If the kinetic energy of the high-speed electron is larger than the binding energy of the inner-shell electron, the inner-shell electron will be ejected from the inner shell of the atom. The vacancy will be quickly filled by an electron dropping down from higher levels with characteristic radiation emitted. The frequency of the emitted characteristic x-ray can be predicted by the Bohr model. Each element has a unique set of energy levels, therefore the x-rays produced by the transition from higher to lower energy levels have frequencies characterized by that element.

Sometimes, instead of radiating a single x-ray photon, an atom with an electron vacancy in the innermost (K) shell can eject one or more electrons. This phenomenon is known as the Auger effect and the ejected electrons are called Auger electrons. This process competes with the characteristic x-ray production.

The SDF scanner employs a novel flying focal spot acquisition scheme (Figure 2-6), which can deflect the electron beam to make the focal spot periodically wobble both in the longitudinal direction (z direction) and in the radial direction. Therefore, the number of simultaneously acquired slices can be doubled to improve the longitudinal resolution and reduce the spiral artifacts. Detail information of this technique can be found in these literatures [38-40].

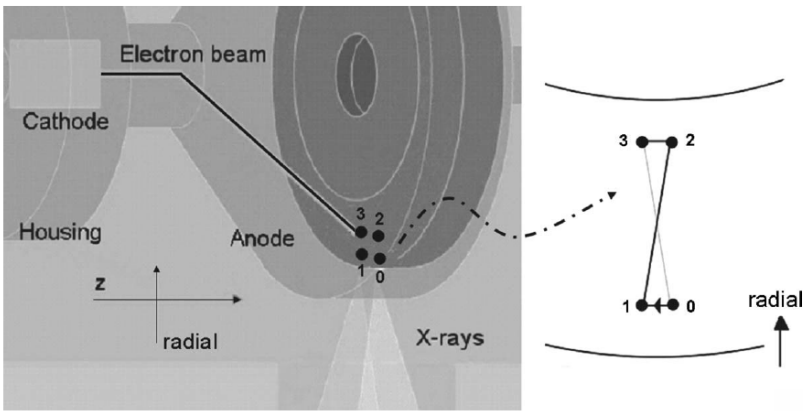

Figure 2-6: The focal spot wobbles between four different positions on the anode plate controlled by an electromagnetic deflection system [38].

2.2.2 X-ray Interaction with Matter

The wavelengths of x-rays are comparable to the sizes of the atoms and hence x-rays can strongly interact with an atom. For the x-rays with energy from 50 eV to 1GeV, the major interaction processes are coherent (Rayleigh) scattering, Compton scattering, photoelectric effect, and electron-positron pair production. The probability for other interactions, such as photonuclear absorption, is very small, so they are disregarded in this thesis.

Coherent (Rayleigh) scattering is the process by which a x-ray photon (about 10 keV) interacts with the bound atomic electrons without excitation of the target atom. The scattered photon has the same energy as that of the incident photon. In this type of interaction, negligible energy is transferred and no ionization occurs. The main effect is that the direction of propagation is changed (Figure 2-7).

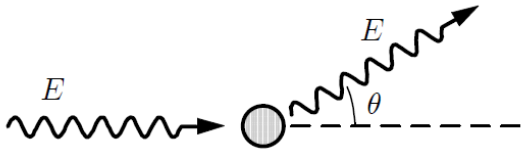

Figure 2-7: Illustration of the coherent scattering [41].

For coherent scattering, the atomic differential cross section (DCS) per unit solid angle can be approximated as

$$\frac{d\sigma_{Ra}}{d\Omega} = r_e^2 \frac{1+\cos^2\theta}{2}[\mathrm{F(q, Z)}]^2, \qquad 2\text{-}2$$

where r_e is the classical electron radius, θ is the polar scattering angle as shown in Figure 2-7, and $F(q, Z)$ is the atomic form factor [42]. The atomic form factor is the Fourier transform of a spatial density distribution of the scattering electron density $\rho(\boldsymbol{r})$ from real space to momentum space, which characterizes the scattering amplitude of a x-ray photon by an isolated atom.

In Compton scattering, also called inelastic or non-classical scattering, a photon of energy E interacts with an atomic electron, which absorbs the photon and re-emits a secondary (Compton) photon of energy E' in the direction $\Omega = (\theta, \phi)$ relative to the direction of the original photon (Figure 2-8).

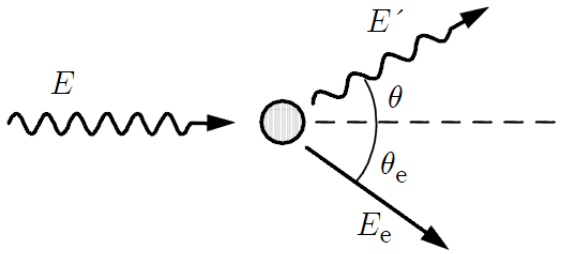

Figure 2-8: Illustration of the Compton scattering [41].

This scattering occurs when the incident x-ray photon has energy considerably higher than the binding energy of an outer-shell (free or valence) electron. The energy loss of the incident x-ray photon depends on its initial energy and the angle of deflection. For an incident photon of energy E, the scattered photon energy E' can be computed as

$$E' = \frac{E}{1 + \frac{E}{m_e c^2}(1 - \cos\theta)}, \qquad 2\text{-}3$$

where m_e is the rest mass of the election, c is the speed of light in free space, and θ is the scattering angle.

In the photoelectric effect, if the energy of an x-ray photon E is larger than the binding energy U_i of the *i-th* shell in the target atom, this photon may be absorbed by the interacting electron, ejecting the electron off from an inner electronic shell deep inside the

atom leaving behind a hole. The free electron is called a photoelectron, the kinetic energy of which is $E_e = E - U_i$. The hole will be filled by an electron from a higher-energy-state outer shell, generating characteristic x-rays with energy equal to the difference between the two energy states. Figure 2-9 illustrates this effect.

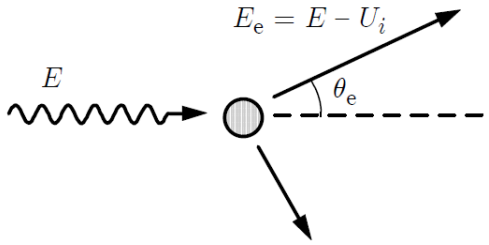

Figure 2-9: Illustration of the photoelectric effect [41].

The probability of photoelectric effect per unit mass is approximately proportional to Z^3/E^3, where Z is the atomic number of the material and E is the energy of the incident photon. When the incident photon energy is approximately equals to the binding energy of the election, the probability will increase and give rise to the so-called K-edge and L-edge in the absorption coefficient.

Pair production is a form of interaction of x-ray with matter characterized by photon-nucleus interaction. When the incident x-ray photon has sufficiently large amount of energy ($> 2m_e c^2 = 1.02$ MeV), it may penetrate the electron cloud and get close to the nucleus. The strong electrostatic field of the nucleus interacts with the high-energy photon and generates a pair of charged particles: a position and an electron. This mechanism is illustrated in Figure

2-10. As this effect may occur when the photon energies greatly exceed the 1.02 MeV energy threshold, it is not applicable to the diagnostic x-ray imaging.

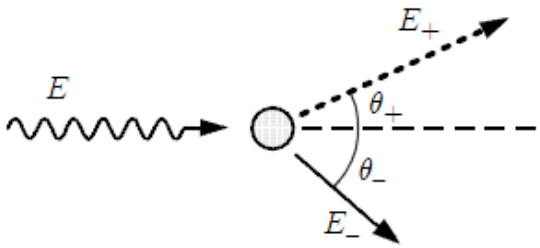

Figure 2-10: Illustration of the pair production [41].

Due to the above interactions, photons are attenuated (i.e., absorbed or scattered) when they pass through materials. The change of the photon number follows Beer-Lambert law [1], which can be expressed by an exponential relationship for an incident x-ray beam with energy ε as

$$N(\varepsilon) = N_0(\varepsilon)e^{-\int \mu(\vec{x},\varepsilon)dl}, \quad 2\text{-}4$$

where $N_0(\varepsilon)$ and $N(\varepsilon)$ are the incident and transmitted x-ray photon numbers, $\mu(\vec{x},\varepsilon)$ is the attenuation coefficient of the material at location $\vec{x}$ and energy ε. The parameter $\mu(\vec{x},\varepsilon)$ can be further expressed as

$$\mu(\vec{x},\varepsilon) = \tau(\vec{x},\varepsilon) + \sigma_{Co}(\vec{x},\varepsilon) + \sigma_{Ra}(\vec{x},\varepsilon), \quad 2\text{-}5$$

where $\tau(\vec{x},\varepsilon)$, $\sigma_{Co}(\vec{x},\varepsilon)$, and $\sigma_{Ra}(\vec{x},\varepsilon)$ are the attenuation coefficients due to photoelectric effect, Compton scattering, and coherent scattering, respectively.

One adverse factor that can degrade the image quality is the scatter radiation due to the coherent scattering and Compton scattering. Both of these two scattering processes generate secondary photons that have different transportation angles with the primary beam. These secondary photons can contaminate the primary transmission data that are used in the reconstruction and affect the image quality [1]. The SDF scanner employs several strategies [43] to minimize the scatter radiation. For example, anti-scatter collimators (Figure 2-11) are used to absorb the photons coming from the other directions. Scatter sensors on either side in the z direction of the detector array (Figure 2-11) are placed outside the penumbra of the primary x-ray beam to obtain a profile of the magnitude of the scattered radiation, with which the scatter radiation can be subtracted from the raw data to correct the measurements.

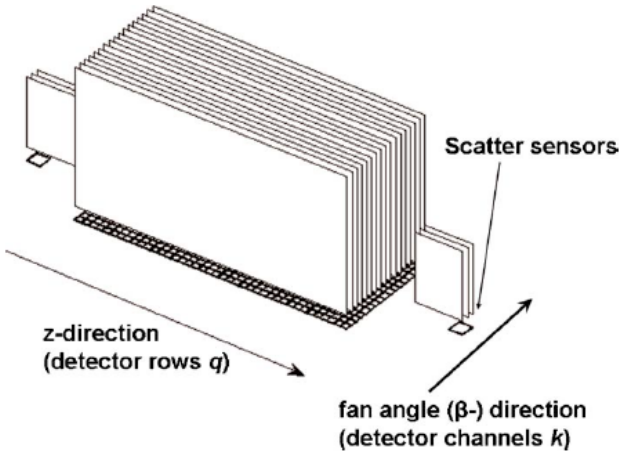

Figure 2-11: Schematic diagram of the geometry of one detector module used in the SDF scanner [43]. The center region consists of the primary detector pixels, positioned below the collimator blades of the anti-scatter collimator. The scattered radiation sensors, placed on both sides of the primary detector module, are equipped with collimator blades as well. The arrows indicate the z direction (row direction) and the fan angle direction (channel direction).

2.2.3 X-ray Detectors

An x-ray photon, after going through and interacting with matter, is detected by an x-ray detector. X-ray detectors are very important part of an imaging system as they determine the quality of an x-ray image. X-ray detectors in CT scanners have experienced two generations, i.e., xenon detectors and solid-state detectors [2].

The first-generation detectors use nonradioactive xenon gas under high pressure (about 25 atm) in long thin cells between two metal plates. Because of the relative low density of the xenon gas, a gaseous detector has to be made very thick (e.g., 6 cm) to improve detection efficiency. Due to the long and thin ionization plates, the xenon detectors are highly directional. Therefore, xenon detectors must be positioned in a fixed orientation with respect to the x-ray source.

When x-rays interact with the xenon gas, induced ions (positive atoms and negative electrons) move to the electrodes along the electric field and the electronic charge is collected. After being amplified, the electronic signal is digitized with its numerical value directly proportional to the intensity of the incident x-ray photons.

The quantum efficiency of gas detectors is inferior to that of solid-state systems, but xenon detectors possess relatively fast decay times, high uniformity of detection sensitivity, and long-term stability against radiation damage [44]. They are still being used in some CT scanners [2].

The second-generation detectors use solid-state scintillators coupled tightly to a photodiode. When struck by x-rays, the scintillator emits visible light, which then reaches photodiode and is converted into an electrical signal proportional to the light intensity via the analog-to-digital converter (ADC). The CT scanner uses energy integrating detector, with a behavior that can be expressed via,

$$p = -\ln\left[\int N_0(\varepsilon)\eta(\varepsilon)\varepsilon e^{-\int \mu(\bar{x},\varepsilon)dl} d\varepsilon\right], \quad 2\text{-}6$$

where p is the logarithmic transmission measurement, $\eta(\varepsilon)$ is the absorption ratio of the detector. The attenuation coefficient of water at 70 keV is about 0.019208/mm, so the integral $\int \mu dl$ or transmission measurement p in clinical applications ranges from 0 to 10.

One potential adverse factor of the solid state detector is the electronic noise, which is due to the fluctuations within the electronic components of the detector, generally following a Gaussian distribution [1]. In order to reduce the influence of the electronic noise, the SDF scanner uses a new detector, called Stellar detector (Figure 2-12). This new detector directly couples photodiode with ADC instead of connecting the photodiode and analog-to-digital convertor (ADC) with an analog connection on an external board [45]. Doing so, the amount of electronic noise added to the signal via the analog connection can be reduced.

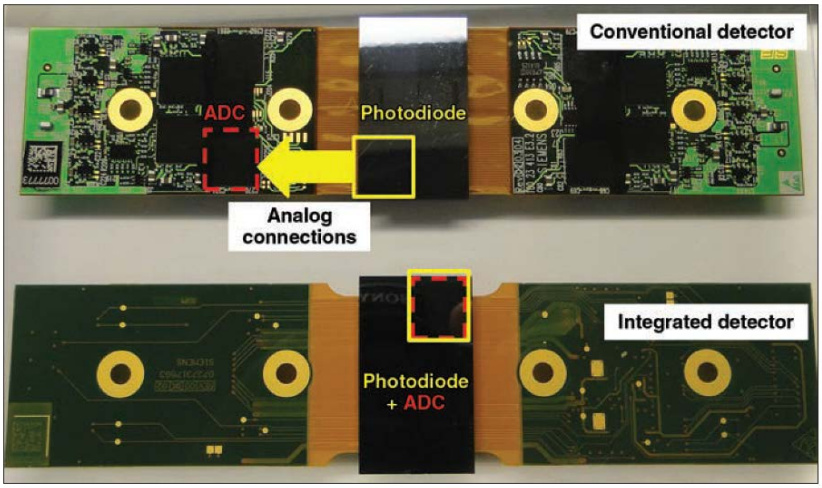

Figure 2-12: Photograph shows conventional CT detector module (top) (Somatom Definition AS+, Siemens Healthcare) and integrated CT detector module (bottom) (Stellar detector, Somatom Definition Flash, Siemens Healthcare) [45].

Solid state detectors typically have better x-ray absorption efficiency since the density and effective atomic number of scintillators are substantially higher than those of xenon detectors. However, in order to reduce crosstalk between adjacent detector elements, it is necessary to maintain a small gap between detector elements, which slightly reduces the geometric efficiency. Unlike xenon detectors, because of the flat top surface of solid state detectors, they are capable of x-ray detection over a wide range of angles.

2.3 Filtered Backprojection Algorithm (FBP)

The x-rays emitted by the x-ray tube spread within a large range (Figure 2-5) and have great influence on both x-ray matter interaction (Eq. 2-4) and x-ray detection (Eq. 2-6). However, most of the reconstruction algorithms including the widely used Filtered Backprojection algorithm (FBP) assume mono-energetic x-ray tube. As such, the poly-

energetic transmission measurements (Eq. 2-6) can be simplified to a simple linear relationship between the measurement and the material attenuation coefficient, i.e.,

$$p(\varepsilon_0) = \int \mu(\vec{x}, \varepsilon_0) dl \,. \qquad 2\text{-}7$$

As FBP is an important component in our work, we quickly review its basic principles in this section.

Here we assume simple parallel beam geometry (Figure 2-13). The parameter $p(t, \theta)$ is the projection along the parallel lines at angle θ, i.e.,

$$p(t, \theta) = \int \int \mu(x, y) \delta(x \cos\theta + y \sin\theta - s) dx dy \,. \qquad 2\text{-}8$$

Based on the Fourier slice theorem [1], the Fourier transform of the projection $p(t, \theta)$ at angle θ equals a line in a two-dimensional Fourier transform of $\mu(x, y)$ taken at the same angle. Therefore, with a series of projections from different angles, we can obtain the complete image information in its frequency domain. If polar coordinate system is adopted, the inverse two-dimensional Fourier transformation can be expressed in this form,

$$\mu(x, y) = \int_0^{\pi} d\theta \int_{-\infty}^{+\infty} P(\omega, \theta) |\omega| e^{i 2\pi \omega (x \cos\theta + y \sin\theta)} d\omega \,, \qquad 2\text{-}9$$

where $P(\omega, \theta)$ is the Fourier transform of the projection $p(t, \theta)$ at angle θ. In the above equation, $P(\omega, \theta)$ is first filtered by a ramp-like filter $|\omega|$, and then the result is inversely Fourier transformed to backwardly update each voxel. Therefore, this algorithm is called the "Filtered Backprojection" algorithm.

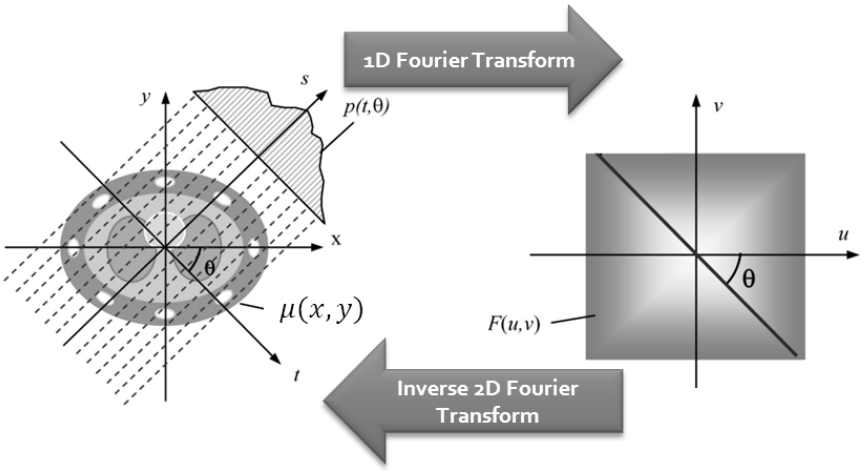

Figure 2-13: Illustration of the Fourier slice theorem [1].

To enhance small differences between different body tissues, the voxel values generally are converted to the intensity scale (called the CT number), i.e.,

$$CT\ number = \frac{\mu - \mu_{water}}{\mu_{water}} \times 1000, \qquad 2\text{-}10$$

where μ_{water} is the linear attenuation coefficient of water. This unit is generally called the Hounsfield Unit (HU).

Because FBP takes the advantage of the fast Fourier transform algorithm and only has a backward projection procedure, it has a fast computation speed and is widely used in the current clinical CT scanners.

2.4 Beam Hardening Effect

The inconsistency between the poly-energetic nature of the physical CT system and the mono-energetic assumption of the reconstruction algorithms leads to a well-known phenomenon called beam hardening (BH) effect. Due to the larger attenuation coefficients of

the materials in the lower energy region (Figure 2-14), x-ray photons with lower energy are preferentially absorbed (Figure 2-15). Such that, as the beam propagates through materials, the average energy of the x-ray beam increases but the transmission measurement recorded by the detector (Eq. 2-6) decreases (Figure 2-16).

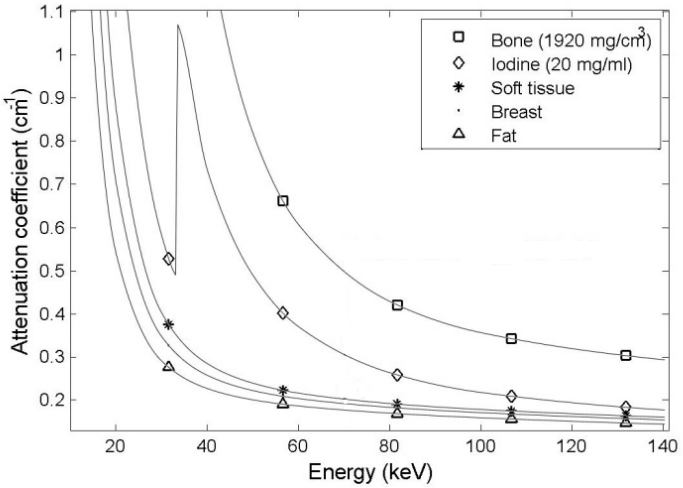

Figure 2-14: Attenuation coefficient for different materials as a function of x-ray energy [46] .

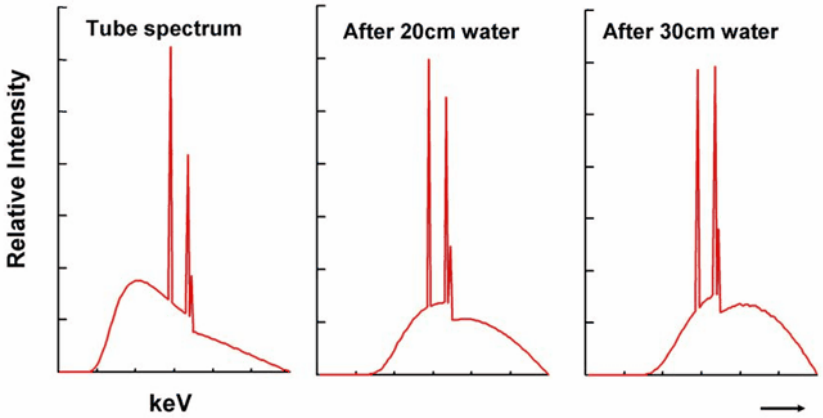

Figure 2-15: Effect of beam hardening as the x-ray beam pass through a water phantom. (a) Original spectrum, (b) after passing through 20 cm of water, and (c) after passing through 30 cm of water [1].

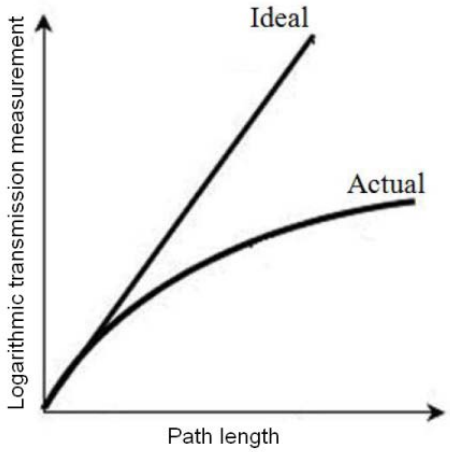

Figure 2-16: Logarithmic transmission measurement as a function of path length.

This nonlinear effect (Figure 2-16) can influence medical interpretations in two notable ways. First, visible influence such as cupping artifacts (Figure 2-17a) and streaking artifacts (Figure 2-18) can seriously deteriorate image quality. Sometimes, they can mimic certain pathologies and lead to misdiagnosis. As water correction [23-26] is usually used to linearize the projection measurements before FBP reconstruction, the cupping artifacts can be largely suppressed (Figure 2-17b). However, water correction cannot suppress the streaking artifacts induced by dense bones, high concentration iodinated contrast agent, and metal implants, as their attenuation properties are different from that of water.

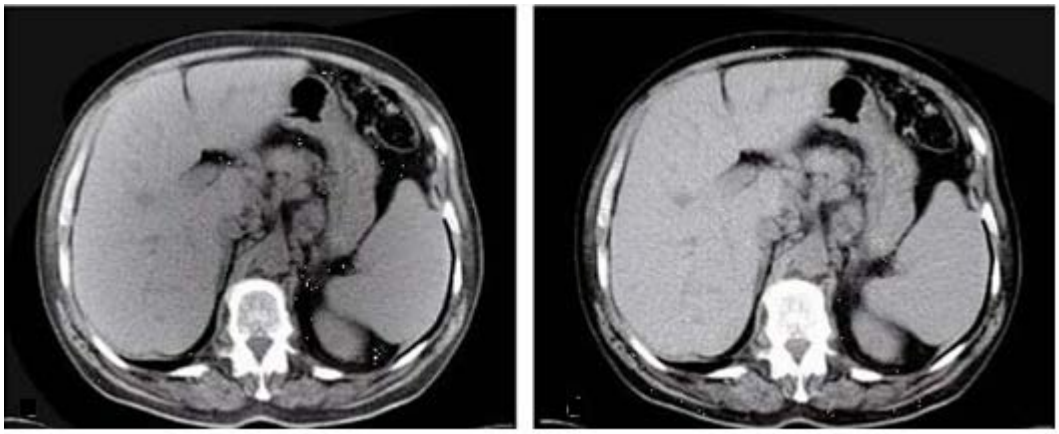

(a) (b)

Figure 2-17: (a) Cupping artifacts due to beam hardening (increased intensities for voxels at the periphery of the object) and (b) the result of water correction [47].

(a) (b) (c)

Figure 2-18: Streaking artifacts due to (a) dense bones [1], (b) high concentration iodinated contrast agent [48], and (c) metal implants [1].

The beam hardening effect also makes the quantitative imaging a challenge, as the CT numbers will become dependent on many influential factors [49], such as body size, anatomic region, nodule size, and x-ray spectrum, etc. The beam hardening effect can be eliminated by dual energy or dual spectrum CT scanner [34-36], but at a high cost due to the sophisticated hardware. Therefore, in this work, we limited our study to the single spectrum CT scanners.

2.5 CT Applications

In this section, we quickly review two important clinical applications of the CT technique that are related with our work, i.e., quantitative CT and CT perfusion. As both of these applications use water-corrected FBP as the image reconstruction method, beam hardening effect can potentially influence the image quality and the subsequent medical interpretations.

2.5.1 Quantitative CT

Quantitative CT (QCT) is a medical imaging technique that has been used to quantitatively (as opposed to qualitatively) measure the density of bone mineral [50], nodules [49] (e.g., lung nodule and liver lesion), and kidney stones [51] and to quantitatively determine the volume of nodules [52] using a standard x-ray CT scanner.

Bone mineral density can be used in the diagnosis and monitoring of osteoporosis, which is characterized by low bone mass and micro-architectural deterioration of bone tissue with a consequent increase in bone fragility and susceptibility to facture [53]. The density of nodules may be a useful feature for distinguishing benign from malignant nodules in computer-aided diagnosis (CAD) [49].

In order to convert the Hounsfield Units of the CT image to density values, a calibration phantom (Figure 2-19) is generally required to be scanned with the patient. These calibration phantoms contain various concentrations of material with similar x-ray attenuation properties to bone. Originally, fluid solutions [53], i.e., di-potassium phosphate

(K_2HPO_4), were used, but because of leakage and transpiration of fluid, air bubbles can develop in the solutions resulting in inaccurate quantification. Therefore, solid materials [53], e.g., hydroxyapatite, were developed and are now widely used.

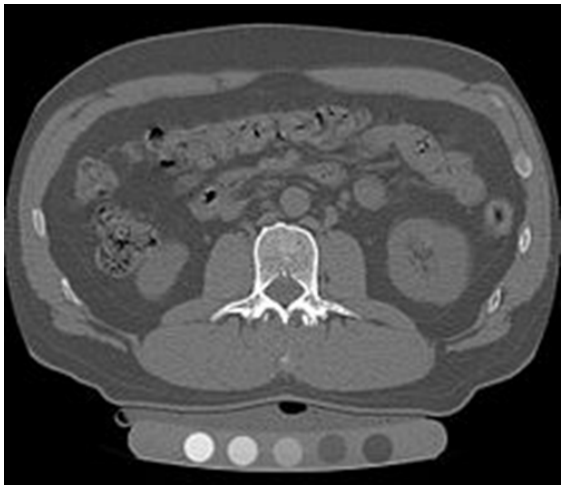

Figure 2-19: A solid phantom placed in a pad under the patient during CT image acquisition is used for calibration. Source: http://en.wikipedia.org/wiki/Quantitative_computed_tomography.

Besides density measurement, QCT is also used to estimate the volume of the nodule [52], which is used as a biomarker for diagnosis, staging or therapy evaluation. For example, the likelihood of malignancy increases if the nodules have an increasing nodule size (>5 mm) [54].

Because of the beam hardening effect, the quantification ability of QCT depends on many influential factors [49], such as patient body size, anatomic region, and spectrum, etc. In Chapter 4, we introduce a new algorithm to address this problem.

2.5.2 CT Perfusion

In CT perfusion imaging, a bolus of iodinated contrast agent is administered to the patient through intravenous injection, and a sequential scanning of a pre-selected region is performed to ascertain quantitative information such as the time-attenuation curve to determine ischemic regions.

For example, Figure 2-20 shows how CT perfusion can be used to differentiate the healthy myocardium and the infarcted myocardium. During the first-pass of the iodine through heart, the ventricle was greatly enhanced due to the high concentration of the iodine contrast agent. The healthy myocardium (the ROI circled in black in Figure 2-20a) is slightly enhanced due to the normal cardiovascular system. In contrast, the myocardium with infarcted cardiovascular system (the ROI circled in white in Figure 2-20b) is not enhanced as the time-attenuation curve is flat.

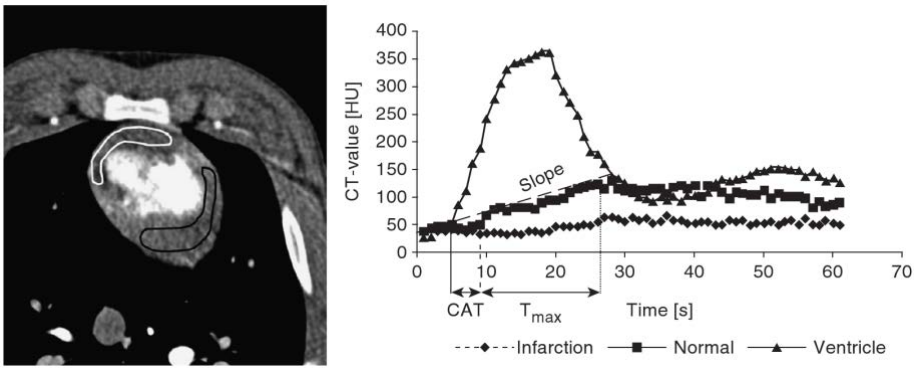

(a) (b)

Figure 2-20: Time-attenuation curves (B) measured from regions of interest that are placed in the area of infarcted myocardium (A: white) and healthy myocardium (A: black). Results are normalized to the enhancement in the left ventricular cavity [55].

However, the beam hardening artifacts induced by the high concentration iodine can result in falsely decreased attenuation of healthy tissue that may be misinterpreted as infarcted myocardium (Figure 2-18b). In Chapter 4, a novel myocardial CT perfusion algorithm will be proposed to account for the attenuation properties of blood-iodine mixtures, such that we can eliminate beam hardening artifacts and provide improved iodine quantification ability for the myocardial perfusion exam.

In addition to the myocardial CT perfusion exams, there are many other important CT perfusion exams, such as breast perfusion [56], lung perfusion [57], and brain perfusion [58], etc. To accurately account for the diverse attenuation properties of tissue-iodine mixtures, we propose another perfusion algorithm in Chapter 6.

2.6 Summary

This chapter provided an introduction to the fundamental x-ray computed tomography. These fundamental concepts form the bases of the work pursued in this thesis. As no two x-ray tubes generate the same spectra due to self-absorption of the bremsstrahlung radiation, this necessitates experimental measurements of the spectra for specific CT scanners. The generation and transmission of the x-rays form the basis of the x-ray spectra modeled and estimated in Chapter 3. Furthermore, the poly-energetic nature of the x-ray spectra leads to material dependent beam hardening effects in CT images. The fundamental physics of interaction of x-rays and matter form the core, based upon which

three poly-energetic reconstruction algorithms are developed for different clinical applications in Chapter 4-6.

Chapter 3

An Angle-dependent Estimation of CT X-ray Spectrum from Rotational Transmission Measurements

The X-ray spectrum provides important information for the CT reconstruction, dose estimation, and quality assurance. However, the current assessment approaches of the CT x-ray spectrum require costly measurement equipment and complicated operational procedures, and are often limited only to the spectrum corresponding to the center of rotation. In order to address these limitations, we propose an angle-dependent estimation technique of the CT x-ray spectrum from rotational transmission measurements, with which incident spectra across a wide range of angular trajectories of the imaging field of view can be accurately estimated with a single phantom and a single axial scan. The proposed technique was experimentally validated using a clinical scanner (Somatom Definition Flash, Siemens Healthcare, Germany) with spectra provided by the manufacturer serving as the gold standard.

The work described in this chapter has been submitted to the journal of Medical Physics for publication [59].

3.1 Introduction

With the improvements of the diagnostic imaging technologies, there are increasing demands for the accurate knowledge of the x-ray spectrum produced by a particular x-ray source. For example, in dose and risk estimations for computed tomography (CT) [60, 61], the x-ray spectrum is used in Monte Carlo simulations to determine the energy deposition in a patient body. In poly-energetic reconstruction [19, 29] or dual energy reconstruction [36], the x-ray spectrum can be used as *a priori* information to reduce beam hardening artifacts and to implement quantitative imaging approaches. It is also desirable to measure the x-ray spectrum for quality assurance purposes, as the spectrum of an x-ray source can drift from the expected values due to repeated usage [62].

Current spectral estimation techniques can be roughly categorized into three approaches: (1) computer simulation, (2) spectroscopic measurements, and (3) transmission-based measurements.

Computer-simulation-based approaches [63-65] aim to estimate generalized spectra based on basic physical parameters, such as the kinetic energy of the incident electrons, the density and the attenuation coefficient of the target material, and the target angle. The characteristic radiation is added to the Bremsstrahlung continuum according to empirical relationships [64]. These approaches can model fundamental mechanics of the x-ray formation process, but are generally unable to fully account for the hardware nuances of

individual x-ray systems (e.g., the used condition of the x-ray tube (Figure 3-1) and the actual attenuation properties of the inherent filtrations and the bowtie filters).

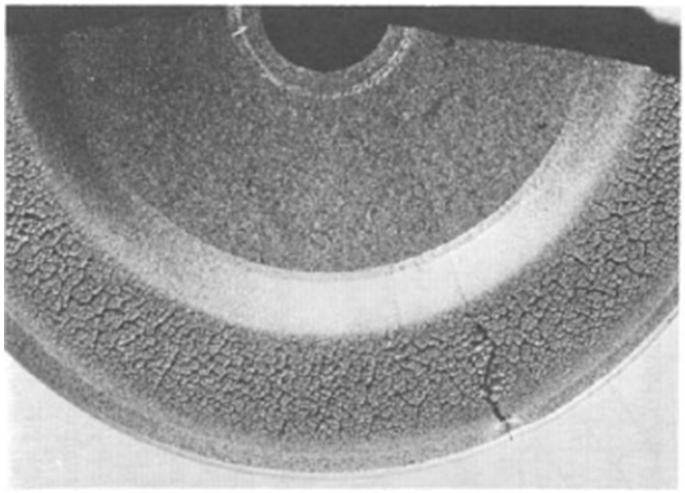

Figure 3-1: An image of the anode damaged by slow rotation and excessive loading after a long time usage [66].

Spectroscopic measurement approaches [67-72] assess the spectrum from a particular x-ray source using energy-resolved, photon-counting x-ray detectors (e.g., CdTe detectors [69-71] or CdZnTe detectors [72]. While these approaches are generally give a more representative estimation of the actual spectrum (considering the limitation implied by the experimental uncertainties), they are not suitable for routine measurements because they require expensive experimental tools (e.g., dedicated detectors) and delicate experimental settings. For example, in the preparation phase, the detector must be calibrated with radioactive elements (e.g., ^{241}Am and ^{133}Ba) and the whole experimental setup needs to be aligned precisely. In addition, the spectrum correction procedure [72] requires a detailed understanding of the detector properties, such that Monte Carlos simulation can be used to

compute the response functions for each detector channel, with which the distorted spectrum can be corrected by stripping methods [72, 73].

A more practical way to spectral estimation is called transmission-measurement-based approaches, which use transmission measurements of phantoms of known dimensions and compositions [62, 74-76]. These approaches are relatively simple and have been shown to provide satisfactory results for various energy ranges of x-ray spectra [62, 74]. However, both the phantom preparation and the measurement process of these approaches can be time consuming and potentially error prone. For instance, in the phantom preparation, two or more materials have to be used and each material has to be carefully shaped and stacked-up into different thicknesses. In the measurement process, all phantoms have to be sequentially exposed to x-rays.

One of the major drawbacks of these approaches is that, without the knowledge of the bowtie filter (i.e., shape, composition, and position), it is difficult to derive the incident spectra across the entire CT field of view (SFOV). Moreover, to obtain the transmission measurements, these approaches often have to be implemented in a special service acquisition mode, where the x-ray tube is stationary [75]. This operational mode is not always available to practicing medical physicists and requires special service personnel from the manufacturer to access the scanner.

In this work, we propose a new transmission-measurement-based approach for clinical CT scanners. Using a single cylindrical phantom and a single axial scan, incident

spectra across a wide range of angular trajectories can be estimated without the knowledge of the bowtie filter characteristics. The method still requires a certain level of access to the raw data from the manufacturer. However, the measurements can be made without having the gantry in the stationary mode. In this paper, we first review the mathematical model of the transmission-measurement-based approaches in Section 3.2.1 and then introduce the proposed off-centered scanning geometry and the data conditioning procedure in Section 3.2.2 and 3.2.3, respectively. This paper further details the experimental validation of the proposed technique in Section 3.2.3.

3.2 Methods

3.2.1 Mathematical Model

The transmission measurements can be expressed as an integral equation as

$$\begin{aligned} Y(L) &= \int_E I(E) e^{-\mu(E)\mathrm{L}} dE \\ &= \int_E N(E)\eta(E) E e^{-\mu(E)L} dE' \end{aligned} \qquad \text{3-1}$$

where $Y(L)$ is the transmission measurement, $I(E)$ is the photon intensity at energy E, $\mu(E)$ is the attenuation coefficient of the phantom, and L is the x-ray attenuation length through the phantom. As a conventional x-ray imaging CT system has energy-integrating detectors, $I(E)$ can be further broken into three components: the incident spectrum $N(E)$ (the objective of the characterization), the detector response $\eta(E)$, and the photon energy E. In this work, $\int I(E)dE$ is normalized to one, so the transmission measurement $Y(L)$ is equivalent to the transmission ratio.

Generally, the measurements expressed in Eq. 3-1 follows a compound Poisson distribution [77, 78]. Previously developed statistical image reconstruction methods have used the assumption of simple Poisson statistics [19, 32, 79] of the measurements with acceptable results. In this work, we adopted the latter assumption, i.e., each measurement $Y(L)$ is assumed to follow a simple Poisson distribution with the mean intensity of $\int_E I(E)e^{-\mu(E)L}dE$ as

$$Y(L) = Poisson\left\{\int_E I(E)e^{-\mu(E)\mathrm{L}}dE\right\}, \tag{3-2}$$

or

$$Y_m = Poisson\left\{\sum_{s=1}^{N_S} A_{m,s}I_s\right\}, m = 1,\ldots, N_M, \tag{3-3}$$

in the discretization form, where N_M is the total number of transmission measurements, N_S is the number of samplings of the spectrum, $A_{m,s}$ is the system matrix element computed from the phantom attenuation, the phantom thickness, and the size of the discretized spectral interval ΔE using the relation

$$A_{m,s} = e^{-\mu_s L_m}\Delta E\ . \tag{3-4}$$

Based on the simple Poisson assumption, the probability of obtaining Y_m with the photon intensity spectrum I_s can be computed as

$$P(\mathbf{I}\,|\,\mathbf{Y},\mathbf{A}) = \prod_m \frac{\left(\sum_s A_{m,s}I_s\right)^{Y_m}}{(Y_m)!}e^{-\sum_s A_{m,s}I_s}\ , \tag{3-5}$$

where $\boldsymbol{I} = \{I_1, \ldots, I_{N_S}\}^T$, $\boldsymbol{Y}$=$\{Y_1, \ldots, Y_{N_M}\}^T$, and $\boldsymbol{A} = \{A_{m,s}\} \in R^{N_M \times N_S}$. In order to estimate I_s, one possible approach is to maximize the log-likelihood objective function of Eq. 3-5 through,

$$\begin{aligned} \mathbf{I} &= \arg\left\{\max_{\mathbf{A},\mathbf{Y}} \ln P(\mathbf{I} \mid \mathbf{A}, \mathbf{z})\right\} \\ &= \arg\left\{\max_{\mathbf{A},\mathbf{Y}} \sum_m \left[Y_m \ln(\sum_s A_{m,s} I_s) - \sum_s A_{m,s} I_s \right] + c \right\}, \end{aligned} \tag{3-6}$$

where c is a constant. As a logarithmic function is concave, based on Jensen's inequality, Eq. 3-6 can be equivalently converted to

$$\mathbf{I} = \arg\left\{\max_{\mathbf{A},\mathbf{Y}} \sum_{m,s} \left[Y_m \ln(A_{m,s} I_s) - A_{m,s} I_s \right] + c \right\}. \tag{3-7}$$

Since this objective function is not quadratic, the Expectation-Maximization (EM) approach [80, 81] is applied to solve this maximization problem. The resulting iteratively multiplicative update form is

$$I_s^{(k)} = \frac{I_s^{(\mathrm{k}-1)}}{\sum_m A_{m,s}} \sum_m \frac{A_{m,s} Y_m}{\sum_{s'} A_{m,s'} I_{s'}^{(\mathrm{k}-1)}}, \tag{3-8}$$

where k indicates the *k-th* iteration. For the EM method, the main features of the spectrum (such as the characteristic x-rays of the x-ray tube and the K-edges of the detector) must be reflected in the initial guess ($I_s^{(0)}$) [62, 75]. After each iteration, the sum of $\sum I_s^{(k)}$ is normalized to one. The iteration can be terminated when the averaged error is smaller than a threshold T as

$$\frac{1}{N_M} \sum_{m=1}^{N_M} \left| Y_m - \sum_{s=1}^{N_S} A_{m,s} I_s^{(\mathrm{k})} \right| \le T. \tag{3-9}$$

Usually, the iterative equation (Eq. 3-8) converges within about 3.0×10^3 iterations for T=10^{-5}. The computational time is less than 2 s using Matlab running on a desktop computer (3GB RAM and 2.5 GHz CPU). With I_s, the incident spectrum N_s can be obtained by dividing the detector response η_s and the energy E_s as

$$N_s = \frac{I_s}{\eta_s E_s}. \qquad 3\text{-}10$$

3.2.2 Acquisition Geometry

Because of the bowtie filter, the incident spectrum $N(E)$ gradually changes as a function of beam angle. In order to fast and accurately sample the transmission measurements for a wide range of angular trajectories, we propose an off-centered acquisition geometry as shown in Figure 3-2.

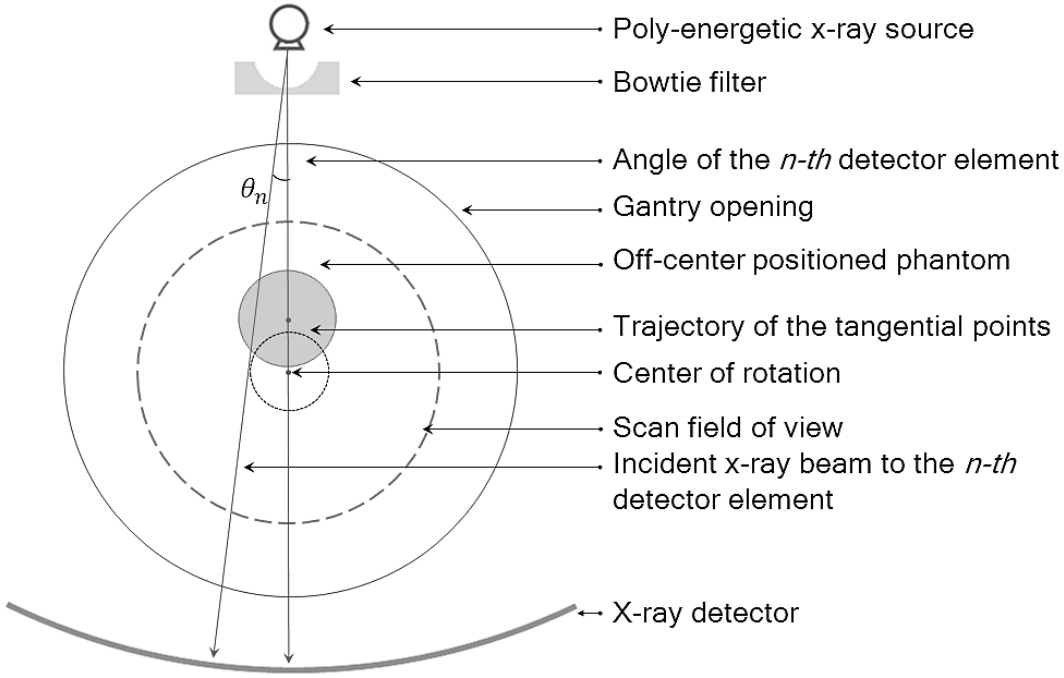

Figure 3-2: Off-centered acquisition geometry for the angle-dependent estimation technique of x-ray spectrum.

Using a cylindrical shaped phantom and targeting the transmission measurements of the *n-th* detector element, the x-ray beam from the x-ray source to the *n-th* detector element is always tangent to a circle (dotted line in Figure 3-2) with its center located at the center of the gantry rotation. Based on this circle, one can trace the position of this x-ray beam and determine the corresponding attenuation length during the rotation of the gantry (Figure 3-3). Starting from position 1 (Figure 3-3a), the attenuation length gradually increases to the maximum (i.e., the diameter of the phantom) at position 2 (Figure 3-3b), decreases to zero at position 3 (Figure 3-3c), and then starts to increase again from zero value at position 4 (Figure 3-3d). Based on this off-centered geometry, the detectors from different angles can

quasi-continuously record a series of transmission measurements with a large range of attenuation lengths.

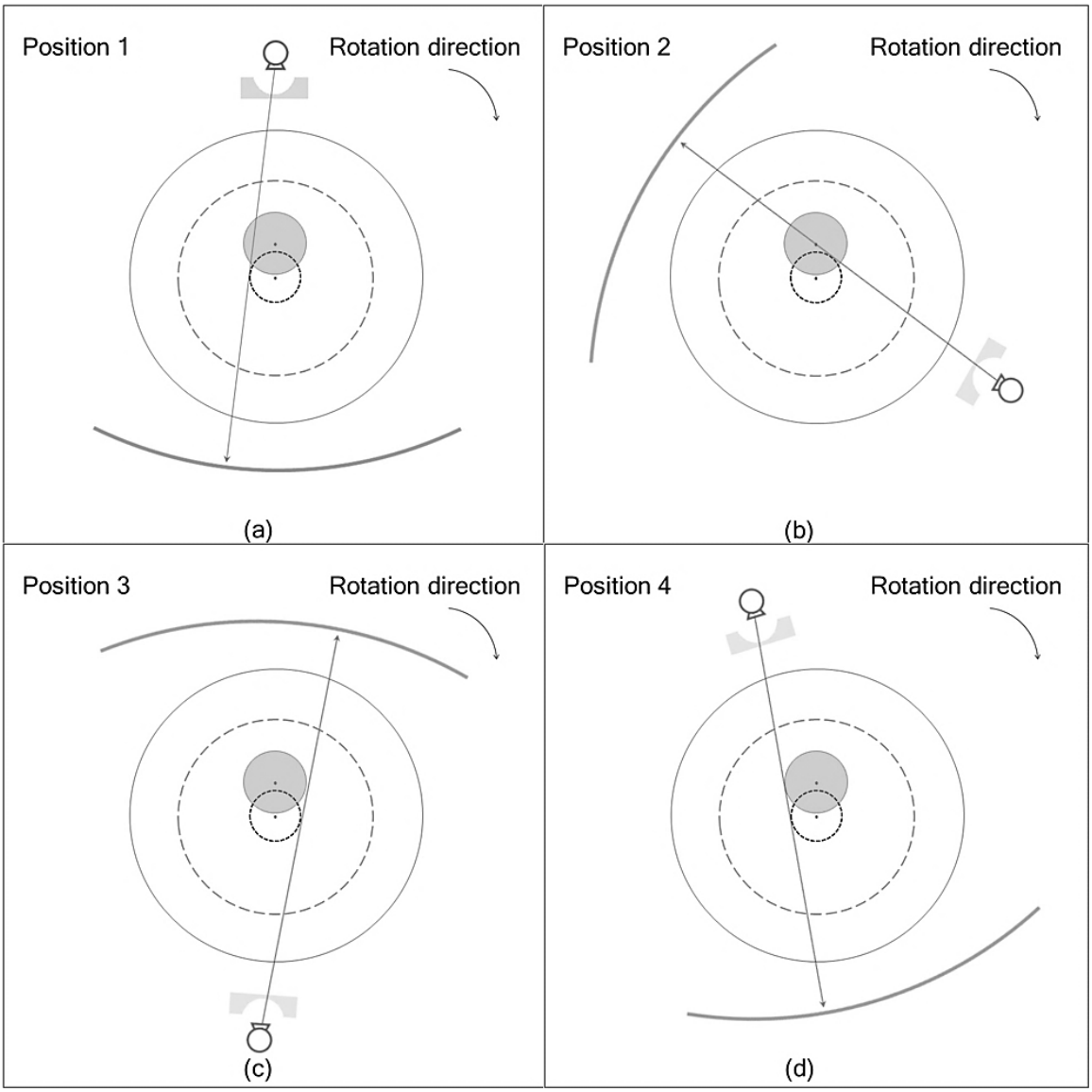

Figure 3-3: Schematic diagram of the change of the attenuation path of the x-ray beam from the x-ray source to the *n-th* detector element during the CT scan in axial mode.

In order to make sure the ranges of the intersection lengths of the central detector elements can always start from zero, the phantom should be kept completely off from the center of rotation (e.g., position 1 in Figure 3-4). With the increase of the distance between the phantom and the rotation center, the phantom can cover a larger range of angular trajectories. The furthest location to position the phantom is position 2 in Figure 3-4, where phantom is tangent to the SFOV. When the detector is rotated to the closest location to the phantom during the CT scan, scatter radiation can increase proportionally (see our Monte Carlos simulation results in Section 3.2.4). As a scanned object is usually positioned in the center, the built-in model-based correction techniques [43, 82] can effectively reduce the scatter radiation via tabulated tables. Therefore, it would be advantageous for the phantom to be positioned only slightly off-centered as in position 1 (Figure 3-4) , so that the scatter radiation pattern is more similar to that of the centered phantom and the scatter radiation across all projections can be readily corrected by the scanner's built-in scatter correction techniques. Positioning the phantom in position 2 provides a wider sampling of the angular trajectories but a larger impact of scatter radiation on the measurements. Note that phantom located beyond position 2 (e.g., position 3 in Figure 3-4) will further result in truncated projections and the cross sectional image cannot be accurately reconstructed for the derivation of the intersection lengths using conventional FBP method. Dedicated reconstruction algorithms for truncated projections have to be employed to extend the CT SFOV [83, 84] for this case.

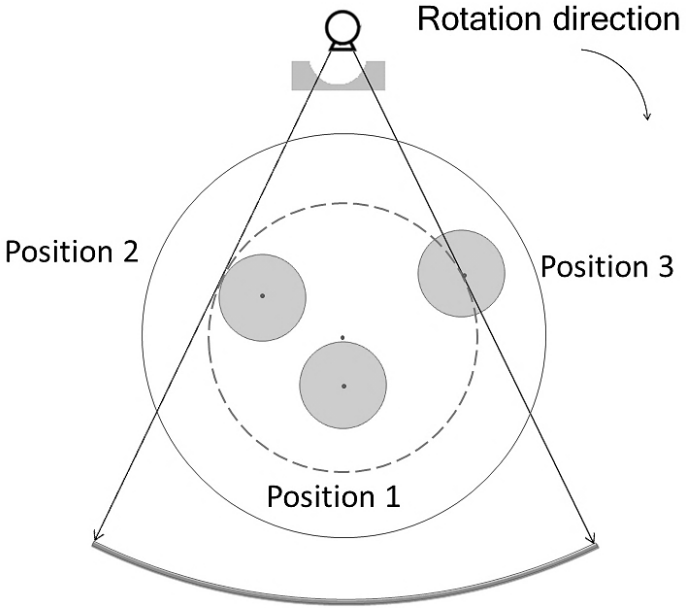

Figure 3-4: Possible off-centered positions. At position 1, the distance between the center of the phantom and the rotation center is slightly larger than the radius of the phantom. At position 2, the phantom is tangent to the SFOV. At position 3, a part of the phantom is positioned outside of the SFOV.

As the phantom is positioned within the SFOV and the CT scanner is operated in axial mode with the x-rays continuously on for a full rotation, the transmission data can be used to reconstruct the cross-sectional image of the scanned phantom. The voxel values that are larger than half of the attenuation of the scanned material can be set to unit one to facilitate deriving the intersection lengths via the forward ray tracing procedure. If the shape of the phantom is convex, a conventional backward ray tracing technique can be used to delineate the border of the phantom instead of using image reconstruction.

The phantom should be made of a material with moderate attenuation properties. Materials with large attenuations (such as metals) could be small in size, but the accuracy of

the intersection lengths derived from the reconstructed image will suffer large errors due to the limited resolution of the CT detectors (0.6 x 0.6 mm^2 at iso-center). Materials with small attenuations provide for a larger phantom enabling smaller relative errors in intersection length measurement, but can lead to increased scatter radiation to the detectors. Plastic materials, such as ultra-high-molecular-weight polyethylene (UHMWPE; chemical formula: $(C_2H_4)_nH_2$, density: 0.937 g/cm^3), have moderate attenuations. In this work, a 160 mm diameter cylindrical phantom made of polyethylene was used to reduce transmission to 0.1 for the maximum path length through the phantom for a typical 140 kVp beam.

3.2.3 Data Conditioning Procedure

The off-centered acquisition geometry can collect hundreds of transmission measurements across a wide range of angular trajectories, which provides abundant experimental data. However, the large amount of data can make the estimation process time consuming, while the data are further contaminated by various sources of noise (such as quantum noise, instrumentation noise, or stochastic variations due to the phantom and the experimental condition). In order to accelerate spectral estimation speed, to reduce noise, and to improve estimation stability, the data is preprocessed before spectral estimation.

Generally, the transmission measurements can be fitted with polynomial functions. Eq. 3-1 can be expanded in a Taylor series as

$$\begin{aligned} Y(L) &= \int_E I(E) e^{-\mu(E)\mathrm{L}} dE \\ &= \sum_k c_k L^k \end{aligned} \quad , \qquad \text{3-11}$$

where

$$c_k = \int_E \frac{I(E)\left[-\mu(E)\right]^k}{k!} dE \,. \qquad 3\text{-}12$$

Because the attenuation length L can be very large (e.g., 160 mm), it is necessary to ensure that the Taylor series converges with a suitable truncation degree. In order to make this determination, the absolute value of the *n-th* term ($|c_k L^k|$, where L=160 mm) of Eq. 3-11 is plotted in Figure 3-5 as a function of polynomial degree (k) for different spectra. In this work, we used a polynomial function with a truncation degree of 11 to maintain errors to be less than 10^{-2}.

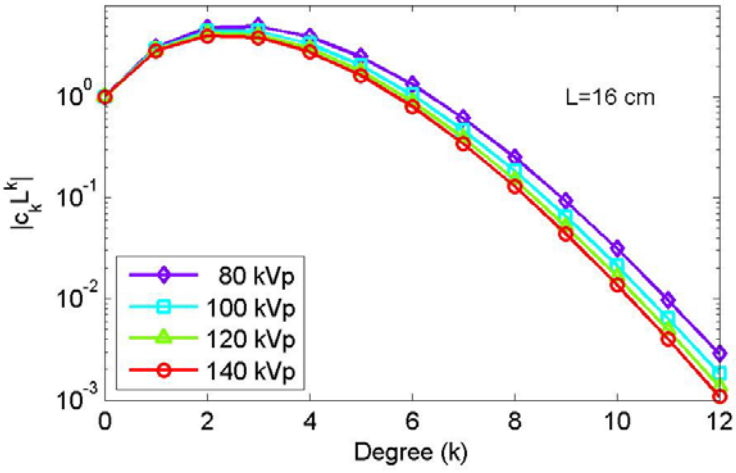

Figure 3-5: The absolute value of the *k-th* term ($|c_k L^k|$, where L =160 mm) of the Taylor series in Eq. 3-11 as a function of polynomial degree (k) for different spectra.

One boundary condition that should be imposed to the polynomial function is that the transmission measurements Y_m should be 1 when x-ray beam is not attenuated ($L = 0$). Because of the limited resolution of the detector and various sources of noise, when an x-ray

path approaches the edge of the phantom, the derived intersection length might change dramatically and the fitted function may not necessarily satisfy this boundary condition. In order to force the polynomial functions through this fixed point, c_0 in Eq. 3-11 is set to unity. In matrix notation, the equation for a polynomial fit is given by

$$\mathbf{Y} - \mathbf{1} = \mathbf{L}\mathbf{c}\,, \tag{3-13}$$

where $\mathbf{1} = [1, \ldots, 1]^T \in R^{N_M \times 1}$, $\boldsymbol{L}$ is the Vandermonde matrix generated by the L_m, i.e.,

$$\mathbf{L} = \begin{bmatrix} L_1^1 & \cdots & L_1^{N_K} \\ \vdots & \ddots & \vdots \\ L_{N_M}^1 & \cdots & L_{N_M}^{N_K} \end{bmatrix}, \tag{3-14}$$

and $\boldsymbol{c} = \left[c_1, \ldots, c_{N_K}\right]^T \in R^{N_K \times 1}$ is the vector of unknown polynomial coefficients. In this work, the linear equation system of Eq. 3-13 is solved by using a fixed point least square method as

$$\mathbf{c} = \left(\mathbf{L}^{\mathrm{T}}\mathbf{L}\right)^{-1}\mathbf{L}^{\mathrm{T}}\left(\mathbf{Y} - \mathbf{1}\right). \tag{3-15}$$

With the fitted polynomial function for each angular trajectory, we resampled 30 measurements equally distributed between L=0 and the measured maximum intersection length for the spectral estimation.

3.2.4 Experimental Validation

The proposed spectral estimation technique was validated on a CT scanner (Somatom Definition Flash, Siemens Healthcare, Germany). Details of the pre-bowtie spectra (140, 120, 100, and 80 kVp), the bowtie filter, and the detector absorption ratios were provided from the manufacturer. These spectra were measured with a spectroscopic x-ray

detector using a Compton scattering method [67, 68, 70]. The bowtie filter was used to derive the incident spectra along different angular trajectories from manufacturer-provided pre-bowtie spectra. The detector absorption ratios were used to convert the estimated photon intensities to incident spectra (Eq. 3-10). The CT geometric information and the scan parameters used are specified in Table 3-1.

Table 3-1: The CT geometric information and the scan parameters used in this work.

Parameter name	Value
Source-to-detector distance	1085.6 mm
Source-to-object distance	595.0 mm
Number of detector bins	736
Fan angle	49.95°
Detector size at iso-center	0.60 x 0.60 mm^2
Bowtie filter	w3
Tube current	500 mAs
Exposure time	0.5 s
Number of projections	1152

In order to reduce the potential influence of the quantum noise, a high mAs setting (i.e., 500 mAs) was used. The obtained two-row data were then averaged with respect to each column to further suppress the quantum noise.

A comparative experiment was conducted between the conventional technique and the proposed technique. For the conventional technique [75], two materials (i.e., Al and Cu) were selected. For each material, nine metal filters of different thicknesses were used. The thicknesses of the metal filters were selected to ensure uniformly-distributed transmission measurements within the [0.0, 1.0] range (Table 3-2). Actual thicknesses of the metal filters

were measured with a caliper. For this technique, the scanner was operated in the service mode [75], i.e., both the x-ray tube and the detector remained stationary. The metal filters were positioned in a proximate location to the x-ray tube to minimize the scatter radiation and the transmission measurements through the metal filters were acquired sequentially along the central axis of the beam.

Table 3-2: Technical description of the Al and Cu filters at 140 kVp.

Material	Density (g/cm^3)		1	2	3	4	5	6	7	8	9
Al	2.700	*L* (mm)	1.000	3.000	5.000	7.500	10.50	14.50	20.50	25.50	40.50
		Y(L)	0.936	0.819	0.721	0.616	0.514	0.401	0.286	0.206	0.098
Cu	8.960	*L* (mm)	0.127	0.254	0.655	1.062	1.562	2.090	3.124	3.658	4.686
		Y(L)	0.864	0.761	0.546	0.415	0.303	0.229	0.140	0.112	0.074

For the new technique, a cylindrical phantom [85] with a 160 mm diameter was used, which was made of uniform ultra-high-molecular-weight polyethylene. The experimental setup is shown in Figure 3-6. First, the scanning section of this phantom was extended beyond the patient table to avoid the influence of the patient bed (Figure 3-6a). Second, this phantom was positioned off center in the SFOV by adjusting vertically the patient bed (Figure 3-6b). With the proposed technique, the scanner was able to be operated in the axial mode. After measurement, raw data were exported from the scanner to an external computer, from which the transmission data were extracted for spectral estimation via a manufacturer-provided program. The beam-hardening corrections were excluded from the transmission data.

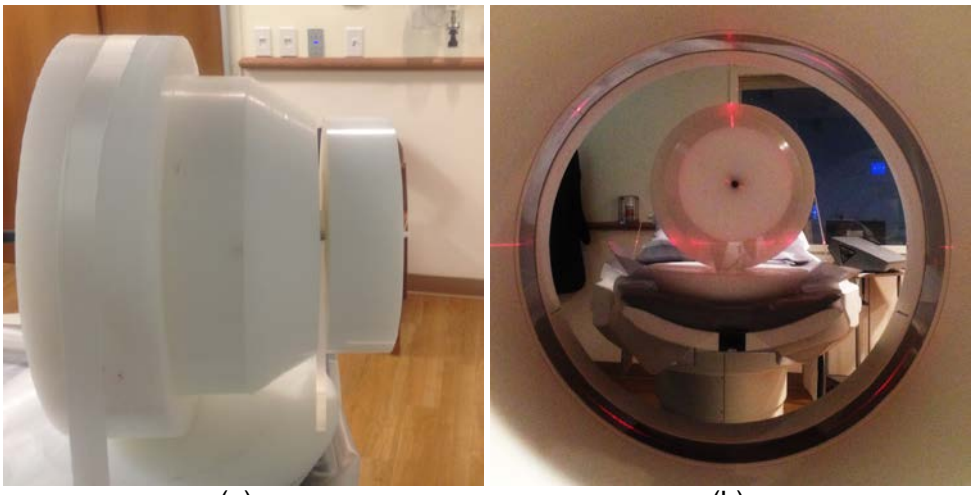

(a) (b)

Figure 3-6: Pictures of the experimental setup of the proposed technique. (a) In the first step, the scanning section of the phantom was extended beyond the patient table to avoid the influence of the patient bed in the followed CT scan. (b) In the second step, the phantom was positioned off-center in the scan field of view by vertically adjusting the patient bed.

To reduce the influence of the scatter radiation, a 2 x 1 mm collimation was used. A Monte Carlos simulation with MC-GPU [86] indicates that the scatter-primary ratios (SPRs) of position 1 in Figure 3-4. As the SPRs of the transmission data were further reduced by the built-in scatter correction strategies of Somatom Flash Definition scanner [43] (e.g., an anti-scatter grid), we postulated that the actual SPRs of the transmission data in our study should be less than that value estimated by the Monte Carlo simulation, and then inconsequential to the measurements. We further demonstrated in a secondary analysis that the distance between the phantom and the detector had negligible influence on the transmission measurements (see Figure 3-10).

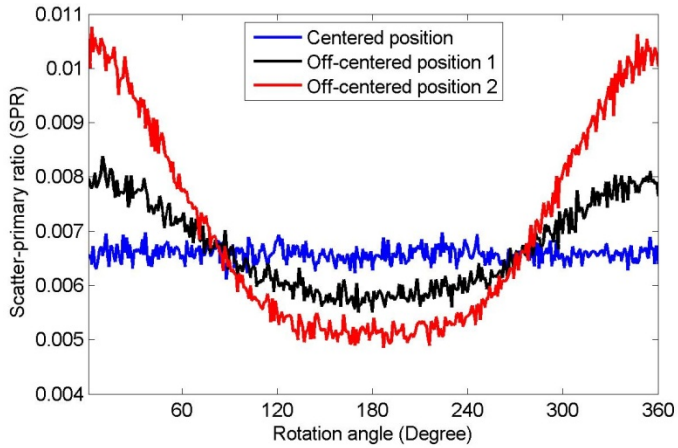

Figure 3-7: Monte Carlo simulation results of the maximum scatter primary ratio as a function of rotation degree for three different phantom positions, i.e., the centered position, the off-centered position 1 in Fig. 3, and the off-centered position 2 in Fig. 3. The geometry of the Somatom Definition Flash scanner was simulated with a perfect detector (2 x 1 mm collimation) and without an anti-scatter grid using Monte Carlos simulation code MC-GPU [86]. A cylindrical phantom made of polyethylene (160 mm in diameter and 250 mm in height) was imaged at 140 kVp.

The maximum fan angle of the estimated spectra depends on the phantom radius r and the distance d between the phantom center and the rotation center. If the x-ray path is required to pass through the phantom center to achieve the maximum intersection length of $2r$ (Figure 3-8), the maximum fan angle would be

$$\varphi = \pm\frac{180^\circ}{\pi}\arcsin\left(\frac{d}{SOD}\right) \qquad 3\text{-}16$$

where SOD is the source-to-object distance (i.e., 595 mm). In that condition, based on our experimental setup (d = 80 mm, i.e., position 1 in Figure 3-8), the angular trajectories would be within $[\theta_{114,}\theta_{622}]$ = [-8°, 8°], where the subscript in θ_n indicates the detector index. However, our results (in Table 3-4) indicate that it is possible to obtain spectra with good

accuracy even if the maximum intersection length is reduced to r (Figure 3-8). In that condition, the transmission measurements are reduced to about 0.2 and the maximum fan angle is extended to

$$\varphi' = \pm\frac{180°}{\pi}\arcsin\left(\frac{d+\sqrt{3}r/2}{SOD}\right) \qquad 3\text{-}17$$

According to the above equation, the range of the angular trajectories was extended to $[\theta_{147},\theta_{589}]$ = [-15°, 15°] for the geometry used in this experiment. The quarter detector offset was considered negligible assuming the angle of the central detector element to be zero, i.e., $\theta_{368} = 0°$.

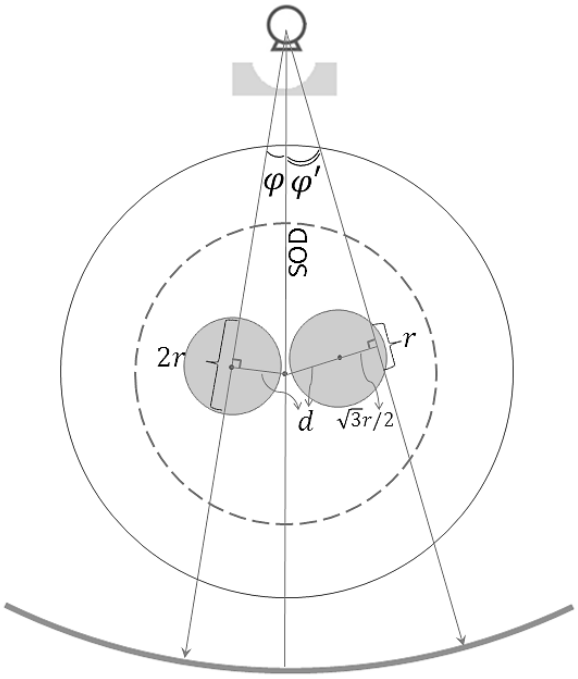

Figure 3-8: Schematic diagram to illustrate the maximum fan angles ϕ and ϕ' determined by the maximum intersection lengths of 2r and r, respectively.

The incident spectrum of the central detector element at 140 kVp was estimated by the conventional and the proposed techniques. The results were compared in terms of the mean energy difference (MED) and the normalized root mean square deviation (NRMSD). The MED was defined as the mean energy of the estimated spectrum minus the mean energy of the manufacturer-provided spectrum. The NRMSD was defined as

$$NRMSD = \frac{\sqrt{\sum_s (N_s - N_s^*)^2 / N_E}}{\max(N_s^*) - \min(N_s^*)}, \quad 3\text{-}18$$

where N_s^* is the expected spectrum, N_s is the estimated spectrum, and N_E is the total number of the energy bins. In addition, the incident spectra of the detector elements between -15° and 15° were estimated and were quantitatively compared with the incident spectra derived from the manufacturer-provided spectra. Note that as the manufacturer-provided spectra cannot be assumed to be the actual gold standard, the MED and NRMSD may not be interpreted as metrics of absolute accuracy.

3.3 Results

3.3.1 The Conventional Technique vs. the Proposed Technique

The transmission measurement results for the central detector element ($\theta_{368} = 0°$) at 140 kVp are plotted in Figure 3-9. Figure 3-9a shows the results of the metal filters (i.e., Al and Cu) using the conventional technique and Figure 3-9b shows the results of the polyethylene phantom using the proposed technique. Both of the experimental results in Figure 3-9a and Figure 3-9b yielded a good agreement with the simulation results. However,

due to the limited number of metal filters, Figure 3-9a included fewer measurements. In contrast, the latter figure included more than 900 measurements, to which a high-degree polynomial function could be fit to reduce the influence of noise and to more accurately represent the transmission measurements.

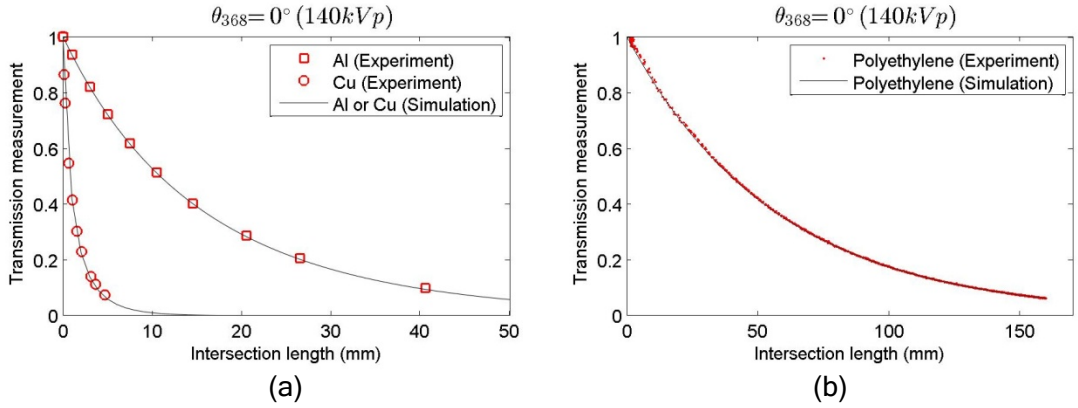

Figure 3-9: Comparison of the experimental results and the simulated results in terms of the transmission measurement as a function of the intersection length for the central detector element ($\theta_{368} = 0°$) at 140 kVp. (a) Experimental measurement results of Al and Cu using the conventional technique. (b) Experimental measurement results of polyethylene using the proposed technique. The estimated error for polyethylene (too small to be visualized) was 0.002, determined by computing the standard deviation of the transmission measurements within the 1 mm interval centered at the intersection length of 137 mm.

Figure 3-10 shows the transmission measurements acquired by the central detector at different locations. The circles and dots indicate the data acquired when the phantom was near to the x-ray tube and the detector, respectively. Both datasets were close to the simulated data (solid line) with no notable difference demonstrating a negligible influence of the scatter radiation on the measurements. The fluctuation of the measured transmission measurements was due to the finite size of the detector (0.6 x 0.6 mm2) and the quantum

noise, which impact the derived intersection lengths. With our data conditioning procedure, the resampled measurements (solid squares) had a good agreement with the simulated measurements and the fluctuation was significantly suppressed.

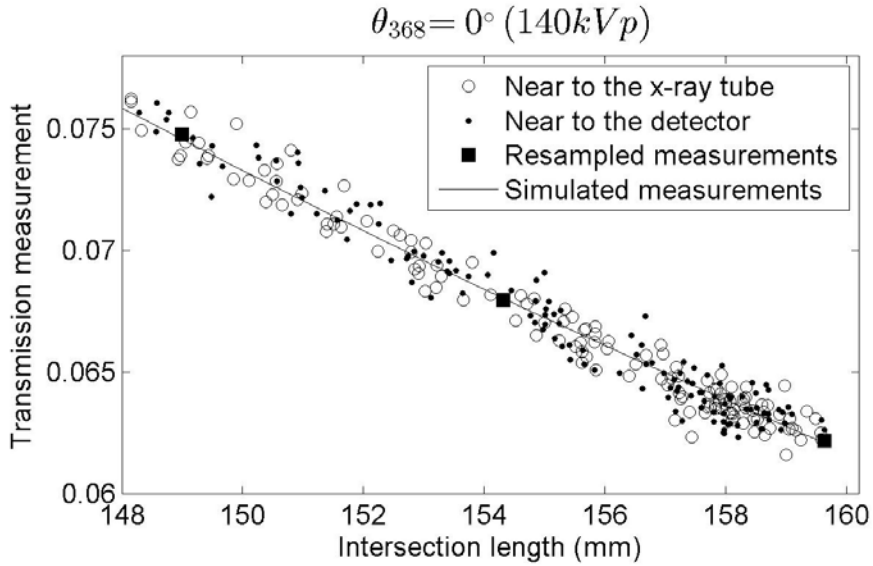

Figure 3-10: Comparison of the transmission measurements acquired by the central detector when the phantom was near to the x-ray tube (circles) and near to the detector (dots). The resampled measurements after data conditioning procedure were plotted as solid squares. The simulated measurements were plotted as a solid curve.

Using the corresponding transmission measurement (Figure 3-9), the incident spectrum of the central detector element was estimated and compared with the initial spectrum and the manufacturer-provided spectrum. The results show that the proposed technique (Figure 3-11b) yielded spectral estimation comparable to those of the conventional technique (Figure 3-11a), as the estimated spectrum was closer to the manufacture spectrum. Detailed quantitative comparison in terms of MED and NRMSD (Table 3-3) shows a slightly closer correlation for our results with the manufacturer-provided spectrum.

It is notable that the NRMSD of the conventional technique here was 1.56%, which was much smaller than that in Duan's work [75] (i.e., [4.7%, 8.6%]). This improvement might be due to the use of more reliable reference spectra in this work, which were provided by the manufacturer instead of being simulated with software. The MED value (0.64 keV) was slightly larger than those reported in Duan's work (i.e., [-0.23, 0.55]), but still within the statistical uncertainty.

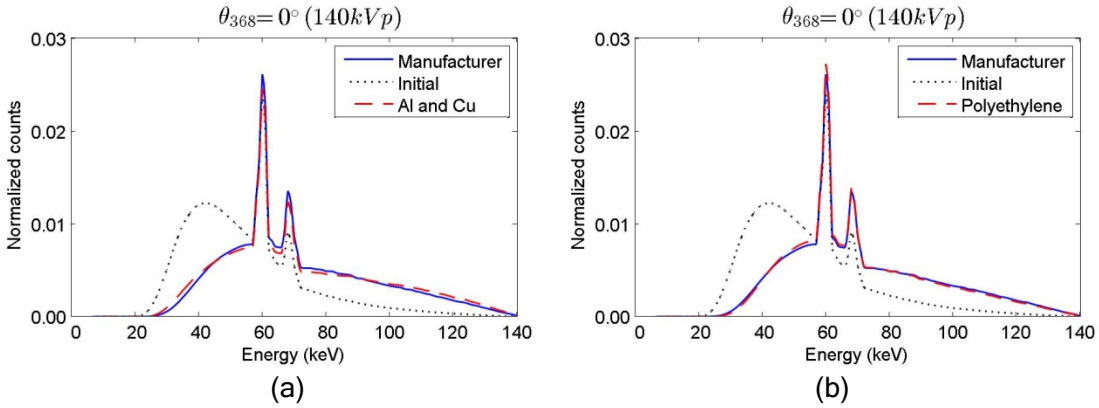

Figure 3-11: Comparison of the central spectrum derived from manufacturer-provided spectrum (solid line), the central spectrum estimated with Al and Cu using the conventional technique (dashed line in (a)), and the central spectrum estimated with polyethylene using the proposed technique (dashed line in (b)). The same initial spectrum (dotted line) was used by the two techniques.

Table 3-3: Comparison of the two techniques in terms of MED and NRMSD for the incident spectrum of 140 kVp.

Beam angle	Method	MED (keV)	NRMSD (%)
$\theta_{368} = 0°$	Conventional technique	0.64	1.56
	Proposed technique	-0.28	0.84

3.3.2 Incident Spectra of Different Angular Trajectories

With the proposed technique, the incident spectra for four non-central x-ray trajectories (i.e., θ_{324} =-3°, θ_{265} =-7°, θ_{206} =-11°, θ_{147} =15°) were estimated and are plotted in Figure 3-12. The reference spectra were derived from the manufacturer-provided spectrum and the bowtie filter. The comparative results show that the estimated spectra accorded well with the reference spectra across different trajectories. The quantitative results in terms of MED and NRMSD are shown in Table 3-4. The results of the extended angular trajectories (i.e., θ_{206} and θ_{147}) were within the statistical uncertainty of the results of the non-extended angular trajectories (i.e., θ_{324} and θ_{265}).

In addition, the beam hardening effect could be observed in these figures, as the photon distribution gradually shifted from low energy to high energy with the increase of the absolute value of the beam angle. This phenomenon can be better appreciated in Figure 3-13, where the incident spectra across a wide range of angular trajectories ($\theta_n \in [\theta_{147}, \theta_{368}]$ = [-15°, 0°]) were estimated by the proposed technique. From Figure 3-13a to Figure 3-13d, different kVp settings (i.e, 140, 120, 100, and 80 kVp) were used.

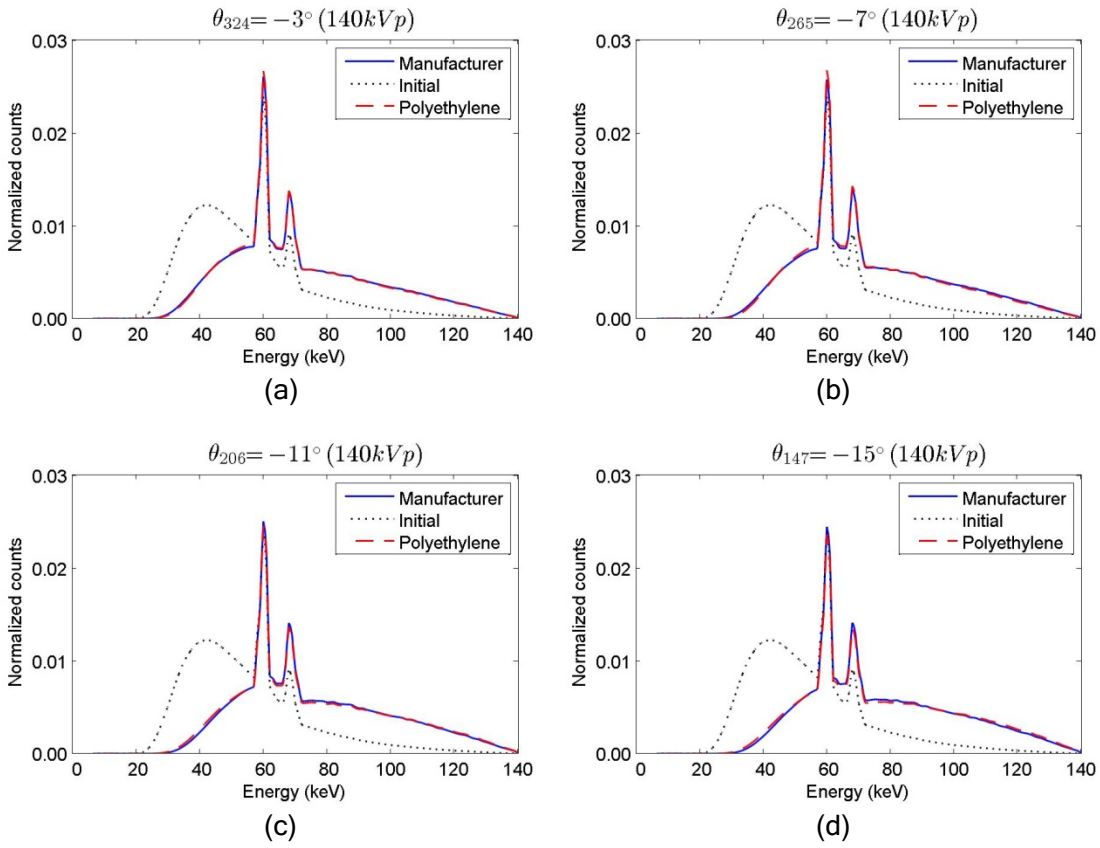

Figure 3-12: Comparison of the manufacturer-provided pre-bowtie spectra (solid line) and the spectra estimated with polyethylene (dashed line) from different beam angles ((a) θ_{324} =-3°, (b) θ_{265} =-7°, (c) θ_{206} =-11°, and (d) θ_{147} =-15°). The same initial spectrum (dotted line) was used.

Table 3-4 Comparison of the estimated spectra from different beam angles in terms of MED and NRMSD for the incident spectrum of 140 kVp.

Beam angle	Maximum intersection length (mm)	MED (keV)	NRMSD (%)
θ_{324} = - 3°	160	-0.20	1.56
θ_{265} = - 7°	160	-0.49	0.76
θ_{206} = -11°	148	-0.11	0.68
θ_{147} = -15°	72	-0.27	0.93

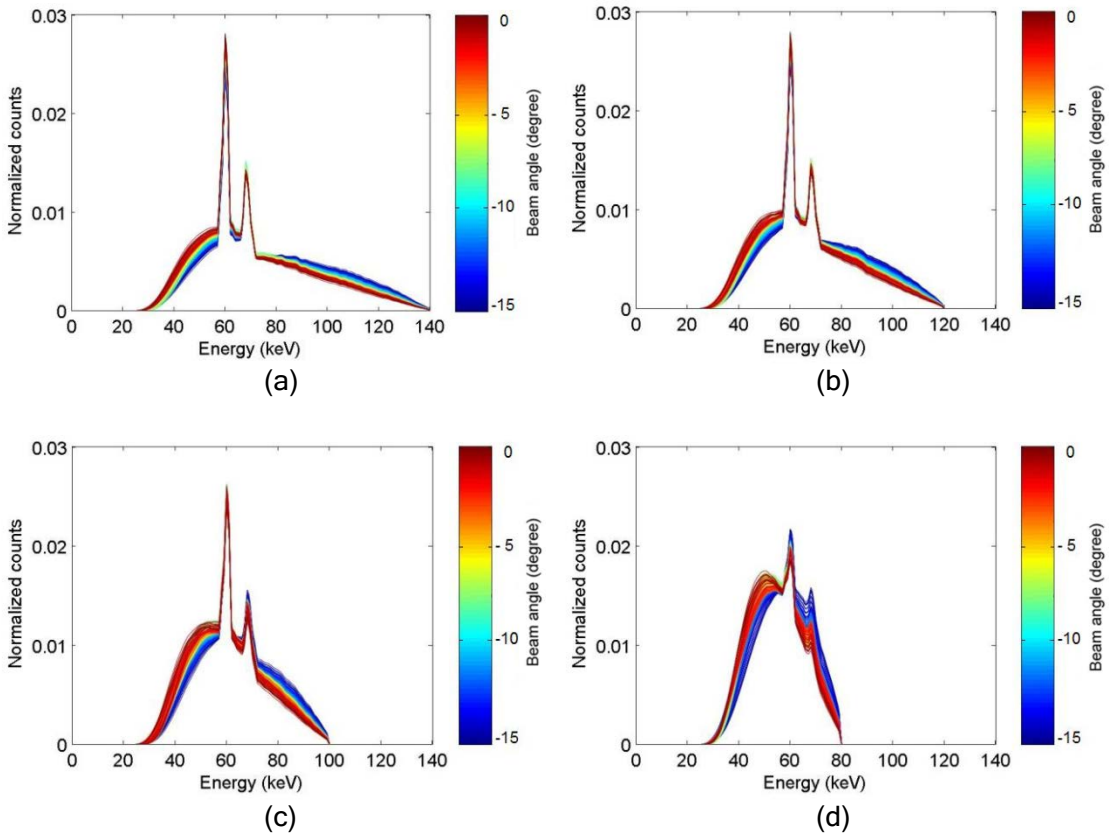

Figure 3-13: Plot of the estimated incident spectra from different beam angles ($\boldsymbol{\theta_n} \in [\boldsymbol{\theta_{147}}, \boldsymbol{\theta_{368}}]$ = [-15°, 0°]) with different kVp settings, i.e., (a) 140 kVp, (b), 120 kVp, (c) 100 kVp, and (d) 80 kVp. The jet color map was used to differentiate spectra along different angular trajectories.

With the estimated spectra, their corresponding mean energies were evaluated as a function of beam angle (Figure 3-14). The mean energies derived from the proposed technique (dots) had an excellent agreement with the mean energies derived from the manufacturer-provided pre-bowtie spectra (solid lines).

The estimation performance for different kVp settings was also assessed (Table 3-5). The averaged absolute MEDs across the beam angles between [-15°, 15°] of all x-ray tube

spectra were less than 0.61 keV with standard deviation less than 0.74 keV. The averaged NRMSDs were less than 3.41% with standard deviation less than 2.02%. These quantities indicate the high estimation accuracy and stability of the proposed technique across different angular trajectories and kVp settings.

With the decrease of the kVp, the averaged NRMSD increased. This is likely due to the decrease in the maximum number of photons in the spectrum, (i.e., $\max(N_s^*)$ = 0.026, 0.025, 0.022, 0.016 for 140, 120, 100, 80 kVp, respectively), which magnified the NRMSD values via the normalization process in Eq. 18. In addition, with decreased kVp, more photons were attenuated leading to increased contribution of the quantum noise and scatter radiation [32, 33].

It was observed that the shapes of the curves (Figure 3-14) had an angle-dependent pattern at higher kVp settings (i.e., 140, 120, and 100 kVp). The mean energies along certain angular trajectories were systematically smaller (e.g., -8° and 8°) or larger (e.g., -6° and -1°) than the simulated mean energies. These patterns were probably caused by systematic errors.

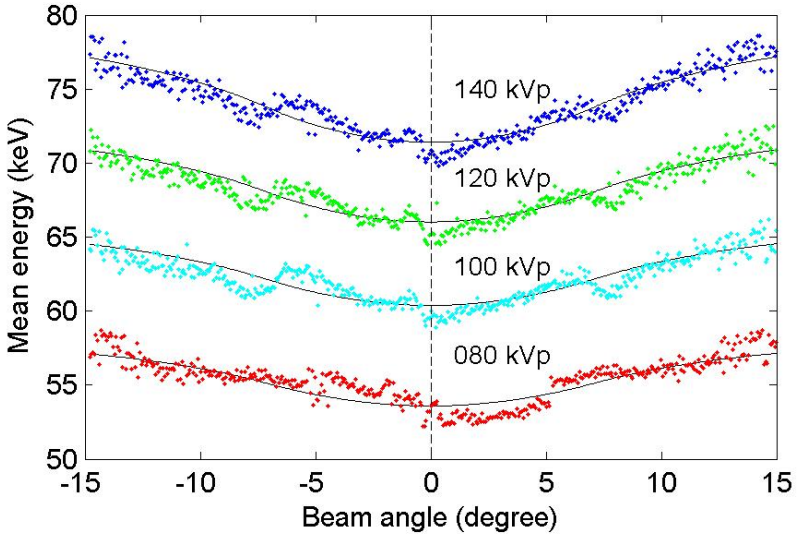

Figure 3-14: Plots of the mean energy of the incident spectrum as a function of the beam angle ($\boldsymbol{\theta_n} \in [\boldsymbol{\theta_{147}}, \boldsymbol{\theta_{589}}] = [\boldsymbol{-15^\circ, 15^\circ}]$). The solid lines were derived from the manufacturer-provided spectra; the dots were derived from the proposed technique. From top to bottom, the results were derived from different kVp settings, i.e., 140, 120, 100, and 80 kVp.

Table 3-5: Quantitative analysis in terms of the averaged absolute MED, the standard deviation of the MEDs, the averaged NRMSD, and standard deviation of the NRMSDs across the beam angles between [-15°, 15°] for different kVp settings.

Beam angle	Spectrum (kVp)	Averaged absolute MED (keV)	Standard deviation of the MEDs (keV)	Averaged NRMSD (%)	Standard deviation of the NRMSDs (%)
$[\theta_{147}, \theta_{589}]$ = [-15°, 15°]	140	0.53	0.66	0.89	0.64
	120	0.57	0.69	1.08	0.75
	100	0.59	0.71	1.60	1.04
	80	0.61	0.74	3.41	2.02

3.4 Discussion

In this work, an angle-dependent estimation technique of CT x-ray spectrum from rotational transmission measurements was presented. This method enables the estimation of

the incident spectra across a wide range of angular trajectories with a single phantom and a single axial CT scan in the absence of the knowledge of the bowtie filter. Compared with the previous techniques, the proposed technique has the following two important features: 1) estimation of the spectra with an off-centered geometry; and 2) an effective data conditioning procedure. With an off-centered geometry, transmission measurements along different angular trajectories can be collected with one rotation using the CT detector elements. This acquisition geometry has three merits. First, the CT scanner can be operated in axial mode instead of in service mode, which is not always accessible in all CT scanners. Second, the axial mode scan greatly increases the data collection efficiency, as transmission measurements across a wide range of angular trajectories can be quasi-continuously collected within a short time. Finally, the collected measurements can be used to reconstruct the cross sectional image of the phantom to facilitate deriving the intersection lengths.

Because of the limited number of the measurements, the previous techniques do not have the data conditioning procedure. Therefore, diverse attenuation materials have to be adopted to reduce noise and to improve estimation stability. In comparison, the proposed technique can collect hundreds of transmission measurements for each angular trajectory. With the abundant transmission measurements, polynomial functions with the correct boundary condition can be used to fit the data, which helps reduce the influence of the dramatic change of the intersection lengths derived from the x-ray paths near the edge of the

phantom. Therefore, this data conditioning procedure reduces noise and improves both the estimation accuracy and the estimation stability.

An experiment was conducted by comparing the conventional technique and the proposed technique. The results show that, for the incident spectrum of the central beam, the MED and the NRMSD of the proposed technique were both largely comparable to those of the conventional technique. The incident spectra across a wide range of angular trajectories were also estimated. The quantitative results show that the average absolute MED and averaged NRMSD of all kVp settings were smaller than 0.61 keV and 3.41%, respectively, which indicates the high accuracy and stability of the proposed technique across different angular trajectories and kVp settings.

Two types of systematic errors might contribute to the angle-dependent pattern in Figure 3-14. The first one is the inherent systematic errors of the detector modules [1, 87] (e.g., gain error, nonlinearity error, and energy sensitivity difference, etc.), as it is impossible to produce identical detector modules in the manufacturing process. An additional possible cause might be due to the unexpected deviation of the bowtie filters. Other possible sources of error remain topics for future research.

There are several ways by which the method developed in this study can be improved. First, one of the major sources of error in our method is the limited resolution of the detector. This error can be reduced using the flying focal spot technique (FFS) [38], which can improve the resolution from 0.6 x 0.6 mm^2 to 0.3 x 0.3 mm^2. Second, while we use a high

mAs setting and a data conditioning procedure to reduce the quantum noise, it is possible to further reduce the quantum noise by averaging multiple axial scans. Third, if we use position 2 in Figure 3-4 , the range of the angular trajectories can be extended to $\theta_n \in [\theta_{17}, \theta_{719}]$ = [-24°, 24°], which almost covers the whole detector range, i.e., [-25°, 25°]. This extension however requires certain accommodations. In order to avoid the influence of the scatter radiation for this position, we can only utilize the transmission measurements acquired near to the x-ray tube for spectral estimation. It is straightforward to extend the proposed method to estimate the spectra along the cone-angle (i.e., z direction). However, with the increase of the cone angle, the scatter radiation will also increase and can potentially contaminate the transmission measurements and result in unreliable estimated spectra. If the knowledge of the bowtie filter is available, spectra can be estimated with a narrow detector collimation and then used to derive the spectra along the cone-angle. Finally, the attenuation properties and the geometry information of the bowtie filter can also be incorporated into the system matrix (Eq. 3-3) and all measurements can be used to reconstruct one pre-bowtie spectrum. These possible extensions of the work will remain topics for future investigation.

3.5 Conclusions

In this work, we proposed a novel angle-dependent estimation technique of CT x-ray spectrum from rotational transmission measurements. In comparison with the conventional techniques, the proposed technique simplifies the measurement procedures, enables the incident spectral estimation ability for a wide range of angular trajectories, and improves the

estimation accuracy and stability. This technique can be applied to both rigorous research objectives (e.g., dose estimation and image reconstruction) and routine clinical quality control procedures.

Chapter 4

A Fast Poly-energetic Iterative FBP (piFBP) Algorithm

Beam hardening (BH) effect can influence medical interpretations in two notable ways. First, high attenuation materials such as bones can induce strong artifacts, which severely deteriorate the image quality. Second, image values can significantly deviate from the expected values based on material attenuation properties, which can lead to unreliable quantification. Some iterative methods have been proposed to eliminate BH effect, but they cannot be widely applied to clinical practice because of the slow computational speed. The purpose of this chapter was to develop a new fast and practical poly-energetic iterative Filtered Backprojection algorithm (piFBP), composed of a novel poly-energetic forward projection process and a robust FBP-type backward updating process. Two phantoms (an oval phantom and an anthropomorphic phantom) were used to quantitatively validate the proposed method.

The work described in this chapter has been published on the journal of Physics in Medicine and Biology [88].

4.1 Introduction

Many different solutions have been proposed in the literature to eliminate the BH effect, and they can be broadly divided into three categories:

The first category is FBP-based linearization approaches [1, 23-28], which aim to correct the raw measurements according to the water's or bone's x-ray attenuation characteristics prior to the FBP reconstruction. For example, McCullough et al [23-26] described a reconstruction method (i.e., water correction) to compensate for the water-related cupping artifacts. However, this method is limited to soft tissue, and for inhomogeneous objects (especially in the presence of bone), BH artifacts are still significant. Later, Joseph and Spital [1, 27, 28] developed a bone correction method for CT images. However, this method requires a threshold-based segmentation process for the initial reconstructed images, which restricts its quantitative reconstruction performance.

The second category is iterative-based base material approaches [19, 29-32], which assume that the target volume consists of N known base materials, and use a linear combination of the known energy dependences to approximate the energy dependence of the attenuation coefficient in each voxel. Base material approaches are a more accurate alternative to the linearization approaches, but limited base materials have been incorporated due to expensive computation. For example, Elbakri and Fessler [19] proposed a segmentation-free displacement model that accounts for soft tissue, bone, and their mixture by their density difference. This method performs well for these base materials, but

is less accurate for fat and breast tissue since their spectral properties deviate from those of the base materials. Chung et al [79] proposed a glandular fraction based tomosynthesis reconstruction algorithm, which can account for adipose tissue, breast tissue, or a combination of both. But this model is restricted to glandular-like materials. The work of Yan et al [31] was similarly limited to the two known materials problem with base materials decomposed into volume fraction. Kyriakou et al [89] proposed a beam hardening correction technique to correct a mixture of materials such as water and bone, which only requires simple segmentation technique without the need of *a priori* information of tube spectra, bowtie filter, detector efficiency, or even attenuation coefficients.

In the third category, as an acquisition alternative, the dual energy approaches [34-36] decompose the attenuation coefficients into components related to photoelectric absorption and Compton scattering. With the dual energy projection datasets, the nonlinear intensity measurements can be transformed to two simple linear integrals of the component coefficients, and then FBP can be used to reconstruct the unknown object. However, this method requires two scans at different kVp settings and a sophisticated hardware setup, such as dual-energy x-ray tubes, rapid kVp switching, or energy discriminating detectors (either layered detectors or photon counting detectors). In addition, if K-edge contrast material is involved, a third material decomposition may need to be added with a third scan [90, 91].

Each approach has advantages and disadvantages. Linearization approaches are fast and widely used in the current clinical practice, but can only reduce visible artifacts and have limited quantitative reconstruction abilities. Iterative base material approaches are accurate for base materials, but cannot be widely used for diagnosis due to slow computational speed. The dual energy approaches are fast and accurate, but the sophisticated hardware and cost limit their applications.

In view of these limitations, this chapter proposes a fast poly-energetic iterative FBP algorithm (piFBP) for single spectrum CT scanners, which combines the poly-energetic forward projection process of the iterative approaches with FBP type backward updating process. For the poly-energetic forward projection process (Section 4.2.1), an adaptive attenuation coefficient decomposition method is proposed, which can help incorporate diverse base materials including diverse body tissues (e.g., lung, fat, breast, soft tissue, and bone) and metal implants. For the backward updating process (Section 4.2.2), a new iterative FBP algorithm with smoothing kernel is proposed to improve the convergence properties. A series of simulations are performed to validate our algorithm.

4.2 Methods

4.2.1 Algorithm

Iterative algorithms can be viewed as feedback loops in which projections are simulated based on the current estimates (forward projection process) and are compared to the measured projections for the backward error updating (backprojection process).

Therefore, faithfully simulating the transmission process of the x-ray beam in the forward projection process and efficiently updating the errors in the backprojection process quickly are two crucial requirements of a poly-energetic reconstruction algorithm. To meet these requirements, a new poly-energetic forward projection method and a new iterative FBP backprojection method were developed as outlined in the following two sections.

4.2.1.1 Poly-energetic Forward Projection Process

The forward projection model for the poly-energetic x-ray beam is given by

$$\overline{p}_r = -\ln\left(\int I(\varepsilon)\exp[-\int_{L_r}\mu(\vec{x},\varepsilon)dl]d\varepsilon\right)\ (r=1,\ldots,N_R), \qquad 4\text{-}1$$

where $\overline{p}_r$ is the estimated logarithmic measurement along the *r-th* ray line L_r, N_R is the total number of the ray paths from the x-ray source to the detector elements, $I(\varepsilon)$ is the spectrum (normalized to unit area), and $\mu(\vec{x},\varepsilon)$ is the unknown spatial- and energetic-related attenuation map of the object. In order to reduce the free degrees of the attenuation map $\mu(r,\varepsilon)$ and to facilitate the evaluation of this nonlinear double integral, we developed the following adaptive base material decomposition method.

Let us assume that the object is composed of N_M known base materials, and each voxel is a mixture of two base materials. The base material set can be selected according to the CT exams. For example, the base material set for a chest CT exam usually comprises air (m=0), lung (m=1), fat (m=2), breast (m=3), soft tissue (m=4), bone (m=5), and metal implants (m=6), where m is the material index. The attenuation coefficient curves [46] of these base materials are plotted in Figure 4-1. Since previous poly-energetic algorithms [19, 23, 28] can

only incorporate one (soft tissue) or two (soft tissue and bone) base materials, errors arise for other materials, such as lung, fat, and breast. Our base material set contains a wide range of materials, so that gradation of attenuation coefficients for various tissue types can be broadly and accurately sampled.

In order to facilitate incorporating the base material set into the forward projection process, the value of the *v-th* voxel (i.e., t_v, $v = 1, \ldots, N_V$) is defined as the attenuation coefficient at a reference mono-energetic energy of ε_0 (e.g. $\varepsilon_0 = 70$ keV), where N_V is the total number of the unknown voxels. Based on t_v, each voxel of mixture can be adaptively decomposed to two adjacent base materials. For instance, if t_v (the circle in Figure 4-1) is within the bone interval, i.e., $[\mu_4(\varepsilon_0), \mu_5(\varepsilon_0))$, where $\mu_m(\varepsilon_0)$ is the attenuation coefficient of the *m-th* base material at the reference energy ε_0, then the attenuation coefficient curve for the *v-th* voxel can be estimated as

$$\mu(t_v, \varepsilon) = \frac{\mu_5(\varepsilon_0) - t_v}{\mu_5(\varepsilon_0) - \mu_4(\varepsilon_0)} \mu_4(\varepsilon) + \frac{t_v - \mu_4(\varepsilon_0)}{\mu_5(\varepsilon_0) - \mu_4(\varepsilon_0)} \mu_5(\varepsilon). \quad 4\text{-}2$$

This expression is defined as a ***separation model***, and the coefficients stand for the base material volume fractions or effective lengths, i.e., for x-ray, the path through the mixture with attenuation coefficient t_v is equivalent to sequential paths through $\frac{\mu_5(\varepsilon_0) - t_v}{\mu_5(\varepsilon_0) - \mu_4(\varepsilon_0)}$ soft tissue and $\frac{t_v - \mu_4(\varepsilon_0)}{\mu_5(\varepsilon_0) - \mu_4(\varepsilon_0)}$ bone. This decomposition approach transfers the energy dependence to countable base materials and the dependence degrees are reflected by base material effective lengths with attenuation coefficients at preselected reference energy ε_0.

This suggests that we can use one forward ray tracing to calculate the energy independent accumulated effective lengths of all base materials, which can then be used repeatedly to estimate the poly-energetic forward projection (Eq. 4-1).

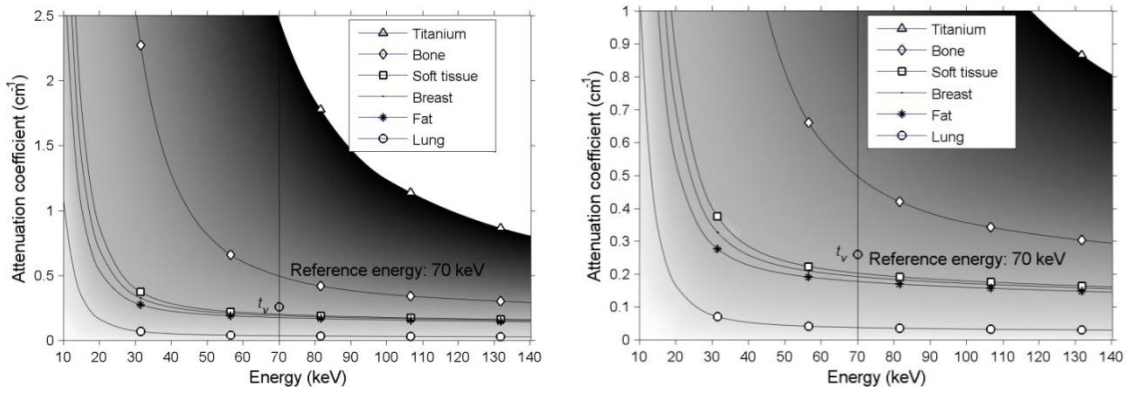

Figure 4-1: The attenuation coefficient curves [46] of the base materials for chest CT exam. (a) A plot with large attenuation coefficient range [0.0, 2.5] to facilitate the appreciation of the relative relationship between the high attenuation curves and the low attenuation curves. (b) A plot with small attenuation coefficient range [0.0, 1.0] to facilitate the appreciation of the relative relationship of the low attenuation curves. The gray gradient indicates the interpolated attenuation curves along the 70 keV reference energy line.

Eq. 4-2 can also be rewritten into an equivalent mass attenuation coefficient form as

$$\mu(t_v,\varepsilon)=\left(\frac{\mu_5(\varepsilon_0)-t_v}{\mu_5(\varepsilon_0)-\mu_4(\varepsilon_0)}\rho_4\right)\left[\frac{\mu(\varepsilon)}{\rho}\right]_4+\left(\frac{t_v-\mu_4(\varepsilon_0)}{\mu_5(\varepsilon_0)-\mu_4(\varepsilon_0)}\rho_5\right)\left[\frac{\mu(\varepsilon)}{\rho}\right]_5, \qquad 4\text{-}3$$

where ρ_m (m=1,…, N_M) is the density of the base materials. The above expression stands for a ***mixture model***, and the coefficients in the round brackets are the base material densities after being mixed. This model is convenient for computing the bone density,

$$\rho_v = \frac{t_v - \mu_4(\varepsilon_0)}{\mu_5(\varepsilon_0) - \mu_4(\varepsilon_0)} \times 1920\ mg/cc\ . \quad 4\text{-}4$$

where 1920 mg/cc is the density of the bone base material [46]. Note that in previous literature [19, 28], bone is generally considered as a water–calcium solution. For cancellous bone, this solution model is reasonably accurate and can be applied to quantitative CT for bone mineral measurement [50, 92, 93]. For cortical bone, this solution model can lead to significant displacement effect [94, 95], which can be accounted by tabulating the decomposition coefficients in Eq. 4-3 for different density bones. As the aim of this work was to validate a new poly-energetic reconstruction algorithm, we assumed the displacement effect would be inconsequential and thus the solution model was sufficient accurate.

A general decomposition equation for the *v-th* voxel can be expressed as

$$\mu(t_v, \varepsilon) = \sum_{m=0,\ldots,N_M-1} \chi_{[\mu_m, \mu_{m+1})}(t_v)\left[\frac{\mu_{m+1}(\varepsilon_0) - t_v}{\mu_{m+1}(\varepsilon_0) - \mu_m(\varepsilon_0)}\mu_m(\varepsilon) + \frac{t_v - \mu_m(\varepsilon_0)}{\mu_{m+1}(\varepsilon_0) - \mu_m(\varepsilon_0)}\mu_{m+1}(\varepsilon)\right], \quad 4\text{-}5$$

where the step function $\chi_{[a,b)}$ is defined as

$$\chi_{[a,b)}(t) = \begin{cases} 1 & t \in [a,b) \\ 0 & t \notin [a,b) \end{cases}. \quad 4\text{-}6$$

For easy observation, the interpolated attenuation curves along the 70 keV reference energy line with Eq. 4-5 is plotted in Figure 4-1 with a gray gradient. To reduce the computational time, the base material interval indices and the corresponding effective lengths for every voxel can be calculated and stored in matrices before each iteration, with

which the accumulated effective lengths of all base materials can be computed through one forward ray tracing as

$$\int_{L_r} \mu(t(\vec{x}),\varepsilon)dl \approx \sum_{v=1,\ldots,N_V} a_{rv}\mu(t_v,\varepsilon) = \sum_{m=0,\ldots,N_M} l_{rm}\mu_m(\varepsilon), \quad \text{4-7}$$

where a_{rv} denotes the elements of the system matrix, and l_{rm} denotes the accumulated effective length of the *m-th* material for the *r-th* ray,

$$l_{rm} = \sum_{v=1,\ldots,N_V} a_{rv}\chi_{[\mu_m,\mu_{m+1})}(t_v) \times \begin{cases} \dfrac{\mu_{m+1}(\varepsilon_0)-t_v}{\mu_{m+1}(\varepsilon_0)-\mu_m(\varepsilon_0)} & m=0 \\ \dfrac{\mu_{m+1}(\varepsilon_0)-t_v}{\mu_{m+1}(\varepsilon_0)-\mu_m(\varepsilon_0)} + \dfrac{t_v-\mu_{m-1}(\varepsilon_0)}{\mu_m(\varepsilon_0)-\mu_{m-1}(\varepsilon_0)} & m=1,\ldots,N_M-1 \\ \dfrac{t_v-\mu_{m-1}(\varepsilon_0)}{\mu_m(\varepsilon_0)-\mu_{m-1}(\varepsilon_0)} & m=N_M \end{cases}$$

. 4-8

With the accumulated effective length l_{rm}, the poly-energetic forward projection equation (Eq. 4-1) can be easily calculated as

$$\begin{aligned} \bar{p}_r &= -\ln\left(\int I(\varepsilon)\exp[-\int_{L_r}\mu(t(\vec{x}),\varepsilon)dl]d\varepsilon\right) \\ &\approx -\ln\left(\sum_{e=1,\ldots,N_E} I_e \exp[-\sum_{m=0,\ldots,N_M} l_{rm}\mu_{me}]\Delta e\right), \end{aligned} \quad \text{4-9}$$

where I_e denotes the *e-th* energy bin (e=1,…, N_E) of the x-ray spectrum and N_E is the total number of the discrete energy bins. For simplicity, Eq. 4-9 can be expressed in a vector notation as

$$\bar{\mathbf{p}} = \mathcal{F}\mathbf{t}, \quad \text{4-10}$$

where $\bar{\mathbf{p}}$ is the column vector containing estimated logarithmic poly-energetic detector values, $\mathbf{t}$ is the column vector containing voxels of the target volume in terms of the attenuation coefficient at reference energy ε_0, and $\mathcal{F}$ is the logarithmic poly-energetic forward projection operator.

The backward projection method of piFBP (detailed in the next section) uses the conventional water correction technique [1, 27]. The water correction technique assumes that the scanned object is mainly made of water equivalent materials in x-ray attenuation characteristics. Such that, each logarithmic poly-energetic measurement (p_r) or estimation ($\bar{p}_r$) corresponds to a water-equivalent length (l_r), which can be determined based on an experiment-based lookup table or the following equation

$$p_r = -\ln\left(\int I(\varepsilon)\exp[-\mu_{\mathrm{w}}(\varepsilon)l_r]d\varepsilon\right), \tag{4-11}$$

where $\mu_w(\varepsilon)$ is the attenuation of water. Multiplying l_r with water's attenuation coefficient at preselected reference energy (ε_0) then yields the water corrected measurements as

$$p_{\mathrm{w},r} = \mu_{\mathrm{w}}(\varepsilon_0)l_r. \tag{4-12}$$

If the scanned object is made of water equivalent materials, water correction can completely eliminate the beam hardening artifacts. In the next section, we will use $\mathbf{p}_w$ to indicate the column vector containing water-corrected logarithmic measurements. The column vector containing water corrected logarithmic poly-energetic forward estimations is correspondingly expressed as

$$\bar{\mathbf{p}}_{\mathrm{w}} = \mathcal{F}_{\mathrm{w}}\mathbf{t}, \tag{4-13}$$

where $\mathcal{F}_w$ is a compound operator consisting of a water correction operation after a logarithmic poly-energetic forward projection operation.

Currently, all clinical CT scanners [89] use this water correction technique to pre-correct the projection measurements, which are then reconstructed by conventional FBP algorithm. As such, this water-corrected FBP method was used as a major comparison method in our validation chapter.

4.2.1.2 Backprojection Method

Iterative FBP (iFBP) has been mainly investigated for the non-uniform attenuation compensation problem in single-photon emission computed tomography (SPECT) [96-99]. With the poly-energetic forward projection operation introduced in the last chapter, the conventional iterative FBP algorithm can be written as

$$\text{piFBP-W: } \begin{cases} \mathbf{t}^{(0)} = \mathcal{B}\mathbf{p}_w \\ \mathbf{t}^{(k+1)} = \mathbf{t}^{(k)} + c\mathcal{B}(\mathbf{p}_w - \mathcal{F}_w\mathbf{t}^{(k)})' \end{cases} \quad 4\text{-}14$$

where $\mathcal{B}$ is the Filtered Backprojection (FBP) operator, $\mathbf{p}_w$ is the column vector containing water-corrected logarithmic poly-energetic measurements, k is the iteration index ($k \geq 0$), and c is the relaxation parameter. In this study, the relaxation parameter c is always equal to one. For convenience, we name the poly-energetic iterative algorithm Eq. 4-14 as piFBP-W, where W stands for the water correction in the iterative updating equation.

In essence, piFBP-W uses the water-corrected measured projections $\mathbf{p}_w$ as reference. If one voxel is underestimated (or overestimated) due to BH effect, the simulated forward

projections $\mathcal{F}_w \mathbf{t}^{(k)}$ through that voxel are likely to be underestimated (or overestimated) with respect to $\mathbf{p}_w$. The differences reflected by the estimated and measured projections are then backward updated to correct the target volume. Ideally, the image estimates will stop changing, i.e., converge to the correct solution, when

$$\mathbf{p}_w - \mathcal{F}_w \mathbf{t}^{(k)} = 0. \qquad 4\text{-}15$$

However, the noise in the CT system, such as quantum noise and electronic noise, can be gradually built up in the target volume in each iteration, and finally result in divergent results. So the conventional form Eq. 4-14 cannot be used for reconstruction directly.

As BH artifacts are mainly low frequency signals, we propose to use a smoothing operator $\mathcal{S}$ to suppress the noise in the correction volume, and improve the convergence stability:

$$\text{piFBP-WS: } \begin{cases} \mathbf{t}^{(0)} = \mathcal{B}\mathbf{p}_w \\ \mathbf{t}^{(k+1)} = \mathbf{t}^{(k)} + c\mathcal{S}\mathcal{B}(\mathbf{p}_w - \mathcal{F}_w \mathbf{t}^{(k)}) \end{cases}. \qquad 4\text{-}16$$

For the smoothing kernel, this study employed a zero-mean 5 x 5 pixels Gaussian low pass filter with a standard deviation (sigma) of 1.05. As the iterative updating equation in Eq. 4-16 contains both a water correction process and a smoothing kernel, we designate this algorithm as piFBP-WS.

For piFBP-WS, water correction needs to be applied to the simulated poly-energetic projections. The water correction can reduce the nonlinearity of the projections, and benefit

the convergence, but it is a time consuming process. Because of monotonicity of the water correction, $\mathbf{p} - \mathcal{F}\mathbf{t}^{(k)}$ and $\mathbf{p}_w - \mathcal{F}_w\mathbf{t}^{(k)}$ have the same updating direction and slightly different updating step sizes, we can omit the water correction process in the backward updating equation to reduce computational time. The new poly-energetic reconstruction algorithm designated as piFBP, can then be expressed as

$$\text{piFBP: } \begin{cases} \mathbf{t}^{(0)} = \mathcal{B}\mathbf{p}_w \\ \mathbf{t}^{(k+1)} = \mathbf{t}^{(k)} + c\mathcal{S}\mathcal{B}(\mathbf{p} - \mathcal{F}\mathbf{t}^{(k)}) \end{cases}. \qquad 4\text{-}17$$

Later we will show that piFBP-WS has better convergence property than piFBP, but piFBP has a faster reconstruction speed and yields similar images.

Two things are worth noting in this Section. First, $\mathcal{F}_w$ and $\mathcal{B}$ are inverse operators of each other when the spectrum is mono-energetic or when the materials in the scanned object are all water equivalent. However, $\mathcal{F}$ and $\mathcal{B}$ are only inverse operators of each other in the former case. Second, Fourier cut-off frequency and the filter type can lead to a so-called inherent error in the reconstruction process [100, 101]. Using a ramp-like filter during the iterative processes can reduce the inherent error by preserving the high frequency edge information. Otherwise, sharp edges will be blurred by the soft filters, which create inconsistency between estimated and measured projections in the subsequent iterations as edge artifacts.

4.2.2 Validations

We simulated a fan beam with an equiangular arc detector row CT geometry. Two phantoms (a simple oval phantom and an anthropomorphic thorax phantom) were used to generate poly-energetic projection data. The simulation parameters are listed in Table C-1 (Appendix C). Quantum noise corresponding to 4.0 x 10^5 photons per detector pixel was added to the projection data. In this work, no inhomogeneous bow-tie filtering and scatter were taken into consideration. All simulations were conducted on Duke Blue Devil GPU Cluster with NVIDIA Tesla C1060 CPUs, which consists of 30 multiprocessors (each with eight SIMD processing cores) and 4 GB of memory.

4.2.2.1 Beam Hardening Index and Noise Index

In our simulations, there are two major errors that cause the computed voxel value t_v to deviate from the expected value t_v^0, i.e., the error due to BH effect (η_v^b) and the error due to noise (η_v^n).

$$t_v = t_v^0 + \eta_v^b + \eta_v^n . \qquad 4\text{-}18$$

The BH effect results in visible artifacts (e.g., cupping and streaking) and invisible voxel accuracy issue. In this work, we only quantified the invisible voxel accuracy issue by measuring the mean errors on uniform regions of a material. The noise term η_v^n in the above equation can originate from different sources, such as quantum noise, electronic noise, under sampling, and discretization model (e.g., target volume voxelization or x-ray line integral,

etc.). Here we assumed that η_v^n was the compound result of these noise sources, followed a zero-mean Gaussian distribution.

In a uniform region of a single material, the standard deviation of η_v^b and the mean value of η_v^n should be both approximately zero values. Thus, we used normalized mean error (NME) and normalized standard deviation (NStd) to quantify the BH effect and noise level, respectively. The mathematical forms for NME and NStd were

$$NME = \frac{1}{N}\sum_{v=1}^{N}\left(\frac{t_v - t_v^0}{t_v^0}\right) \approx \frac{1}{N}\sum_{v=1}^{N}\frac{\eta_v^b}{t_v^0}, \tag{4-19}$$

and

$$NStd = \sqrt{\frac{1}{N}\sum_{v=1}^{N}\left(\frac{t_v - \bar{t}}{t_v^0}\right)^2} \approx \sqrt{\frac{1}{N}\sum_{v=1}^{N}\left(\frac{\eta_v^n}{t_v^0}\right)^2}, \tag{4-20}$$

where N is the total number of the voxels in the measured ROI, and $\bar{t}$ is the ROI mean value. Previous researchers [19, 102] utilized normalized root mean square error (NRMSE) to quantify the differences between the reconstructed image and phantom image. However, it is not difficult to derive that

$$NRMSE = \sqrt{\frac{1}{N}\sum_{v=1}^{N}\left(\frac{t_v - t_v^0}{t_v^0}\right)^2} \approx \sqrt{NME^2 + NStd^2}. \tag{4-21}$$

If BH effect is eliminated after several iterations, NME will approach zero, and then NStd can be used to approximate NRMSE. For simplicity, we used BH index (BIdx) and noise index (NIdx) to denote as percentage of NME and percentage of NStd, respectively:

$$BIdx = NME \times 100, \text{ and} \quad 4\text{-}22$$

$$NIdx = NStd \times 100. \quad 4\text{-}23$$

4.2.2.2 Oval Phantom Simulations

An oval phantom (Figure 4-2) consisting of lung, fat, breast, soft tissue, and bone (1200 mg/cc) was used for our validation. This phantom is a simplified and idealized model to visually and quantitatively assess the performance of the reconstruction algorithms.

Six simulation tests were conducted on this phantom, i.e., an algorithm test, a convergence test, a phantom size test, a spectrum type test, and a spectrum mismatch test. In the first simulation test, reconstruction results of the 32 cm oval phantom were compared between different algorithms, including FBP with a mono-energetic spectrum projection dataset (70 keV), and water-corrected FBP and piFBP-type methods (piFBP-W, piFBP-WS, and piFBP) with a poly-energetic spectrum projection dataset (80 kVp). In the second simulation test, the convergence properties of the piFBP-type methods (piFBP-W, piFBP-WS, and piFBP) were investigated on the same 32 cm oval phantom. In the third simulation test, the oval phantom was scaled to four sizes, i.e., 16, 24, 32, and 40 cm diameter, to examine the reconstruction stability associated with the phantom size. In the fourth simulation, we varied the spectrum (80, 100, 120, and 140 kVp) to test the reconstruction stability associated with the x-ray spectrum. A spectrum mismatch test was conducted to investigate the influence of a possible difference between the actual and the assumed spectra. By adjusting the inherent aluminum filtration of the x-ray tube, the correct spectrum of 80 kVp could be softened or

hardened to yield nineteen mismatch spectra with the normalized root mean square differences (NRMSDs) ranging from -9% to 9% [75], where negative NRMSDs indicate softened spectra and positive NRMSDs indicate hardened spectra. Finally, a base material transition test was conducted to investigate the benefit of more base materials. The projection dataset acquired with a 32 cm oval phantom and a spectrum of 80 kVp was reconstructed by increasing the number of the base materials. The base material groups used in this test are listed in Table 4-2. The parameters used in the six simulation tests are summarized in detail in Table 4-1.

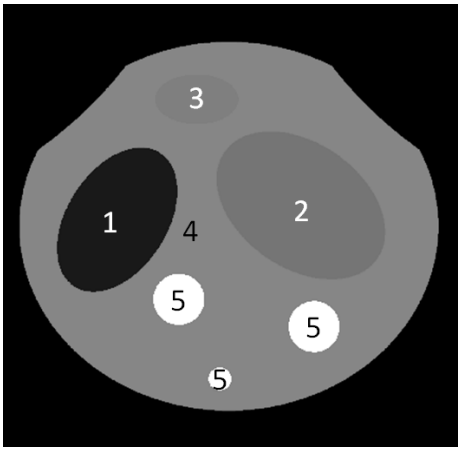

Figure 4-2: Definition of the oval phantom with (1) lung, (2) fat, (3) breast, (4) soft tissue, and (5) bone (1200 mg/cc). This phantom was scaled to four different sizes, i.e., 16, 24, 32, and 40 cm in diameter.

Table 4-1: Parameter summary of simulation tests for the cylindrical phantom.

Simulation tests	Varying parameters	Fixed parameters
Algorithm test	Algorithm: FBP (70 keV) FBP (80 kVp) piFBP-W (80 kVp) piFBP-WS (80 kVp) piFBP (80 kVp)	Phantom size: 32 cm Iteration: 4
Convergence test	Algorithm: piFBP-W piFBP-WS piFBP Iteration number: 0, 1, 2, 3, 4, 10	Phantom size: 32 cm Spectrum: 80 kVp
Phantom size test	Algorithm: FBP, piFBP Phantom size: 16, 24, 32, and 40 cm	Spectrum:80 kVp Iteration: 4
Spectral type test	Algorithm: FBP, piFBP Spectrum: 80, 100, 120, 140 kVp	Phantom size: 32 cm Iteration: 4
Spectral mismatch test	Mismatch spectrum: NRMSD = -9%,…, 9%	Algorithm: piFBP Phantom size: 32 cm Spectrum:80 kVp Iteration: 4

Table 4-2: Base material groups used in the base material transition test.

	Group 1	Group 2	Group 3	Group 4	Group 5
Base material	Water	Soft tissue Bone	Breast Soft tissue Bone	Fat Breast Soft tissue Bone	Lung Fat Breast Soft tissue Bone

4.2.2.3 Anthropomorphic Thorax Phantom Simulations

In contrast to the previous phantom, real CT data from the database of The Cancer Imaging Archive (TCIA, http://www.cancerimagingarchive.net/) was used to create a more complex and realistic anthropomorphic thorax phantom (Figure 4-3). This phantom was composed of various materials, including five main body tissues (i.e., lung, fat, breast, soft tissue, and bone) and one metal implant (i.e., Titanium). With this phantom, the reconstruction performance under an extreme condition, i.e., when a metal implant exists in the patient body, were investigated by comparing piFBP (80 kVp) with FBP (70 keV) and FBP (80 kVp).

Figure 4-3: Definition of the anthropomorphic thorax phantom with (1) lung, (2) fat, (3) breast, (4) soft tissue, (5) bone (1600 mg/cc), and (6) metal implant (Titanium).

4.3 Results

4.3.1 Oval Phantom

4.3.1.1 Algorithm Test

Figure 4-4 shows the reconstructed images of the oval phantom by different algorithms with the corresponding quantitative results listed in Table 4-3.

For reference purposes, the oval phantom with real attenuation coefficients (70 keV) of body tissues is shown in Figure 4-4a, and the images reconstructed by FBP (70 keV) is shown in Figure 4-4b. Because of the use of a mono-energetic spectrum, there were no visible BH artifacts in the reconstructed image, and the BIdx values of all materials were zeros. The NIdx values reflected the normalized noise levels, which were the lower limits that can be achieved by the poly-energetic reconstruction algorithms. Please note that the NIdx of the lung was larger than those of the other body tissues. That is because lung has smaller attenuation coefficient, which magnified its NIdx value through the normalization process in Eq. 4-20. The BIdx and NIdx of Figure 4-4b were provided as benchmark values.

Figure 4-4c shows the image reconstructed by water-corrected FBP with 80 kVp poly-energetic spectrum. Because of the BH effect, the dark streak artifacts between the bones severely degraded the image quality and the BIdx values of all materials spread within a large range of [-1.8, 10.4], which undermined quantitative evaluation. Based on the attenuation coefficient, the estimated bone density was 1464 mg/cc, which significantly deviated from the expected value of 1200 mg/cc. The NIdx values of FBP (80 kVp) were

slightly larger than the NIdx benchmark values. This was due to the fact that the 80 kVp spectrum had more low energy photons than the 70 keV spectrum, so more photons were attenuated and less photons could reach the detector, which raised the quantum noise in the measurements, and finally raised the noise level in the reconstructed images.

The image reconstructed by the piFBP-W algorithm after four iterations is shown in Figure 4-4d. The strong noise severely deteriorated the image quality, and the NIdx values in Table 4-3 increased multiple times for all materials. However, the iterations did help reduce the streak artifacts, making the streak artifacts almost invisible. This improvement was also reflected by the reduced spread range of BIdx, i.e., [-0.9, 0.7].

With the smoothing filter, the images reconstructed by piFBP-WS and piFBP with four iterations are shown in Figure 4-4e and f. Neither of these had visible beam-artifacts or severe noise. In addition, the two images were almost visually identical to Figure 4-4b. The quantitative results showed that both BIdx and NIdx were close to their corresponding benchmark values. With Eq. 4-4, the bone density was estimated to be 1201 mg/cc, which was very close to the expected value of 1200 mg/cc.

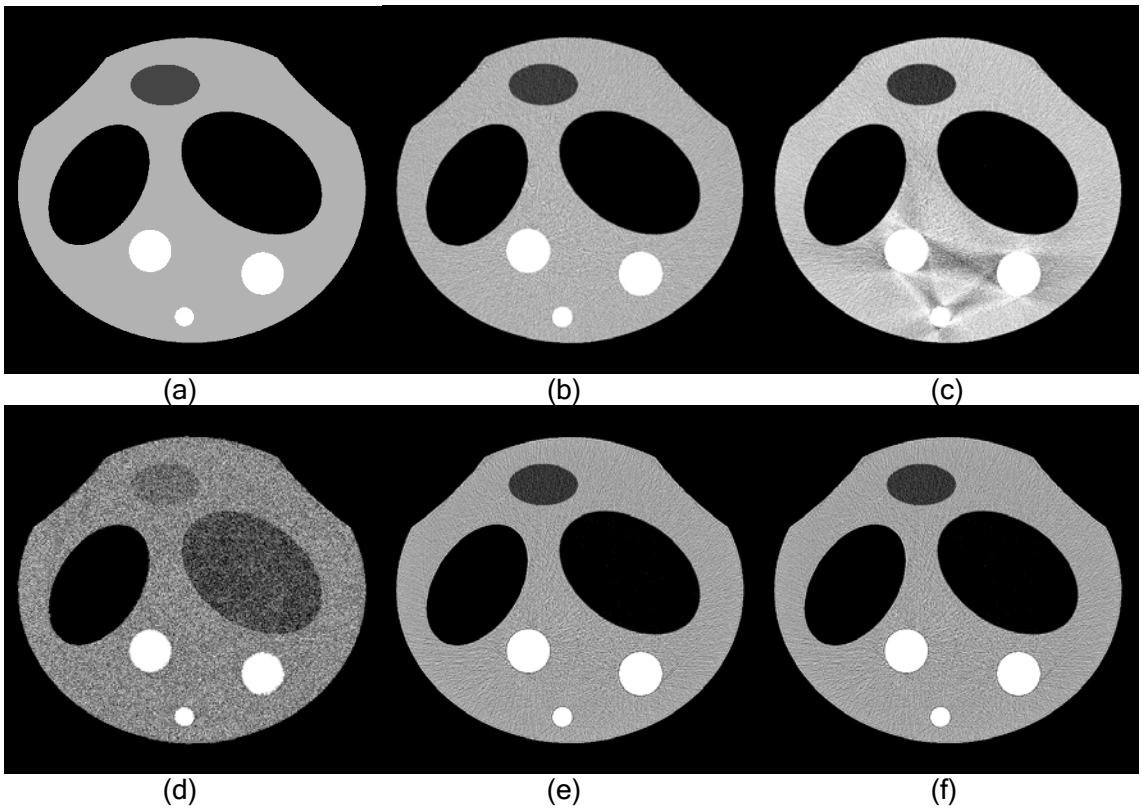

Figure 4-4: Reconstruction results of the oval phantom. Image (a) shows the oval phantom with real attenuation coefficients (70 keV) of various body tissues; Image (b) was reconstructed by FBP with mono-energetic 70 keV spectrum projection dataset. The rest images were reconstructed from the same poly-energetic 80 kVp spectrum projection dataset but different algorithms, i.e., (c) water-corrected FBP (d) piFBP-W, (e) piFBP-WS, and (f) piFBP. Window level = 40 HU and window width = 100 HU.

Table 4-3: Quantitative results of the oval phantom in terms of the beam hardening index (BIdx) and noise index (NIdx) for different materials and reconstruction algorithms.

BIdx / NIdx	Lung	Fat	Breast tissue	Soft tissue	Bone
FBP (70 keV)	0.0 / 1.1	0.0 / 0.3	0.0 / 0.3	0.0 / 0.4	0.0 / 0.2
FBP (80 kVp)	1.5 / 1.4	-1.8 / 0.4	-1.0 / 0.3	0.1 / 0.6	10.4 / 0.4
piFBP-W	-0.8 / 5.5	-0.8 / 1.4	-0.9 / 1.1	-0.4 / 1.4	0.7 / 0.8
piFBP-WS	0.0 / 1.7	-0.1 / 0.5	-0.1 / 0.4	0.0 / 0.5	0.1 / 0.3
piFBP	0.0 / 1.7	-0.1 / 0.5	-0.1 / 0.4	0.0 / 0.5	0.1 / 0.3

4.3.1.2 Convergence Test

To further explore the convergence properties of the algorithms piFBP-W, piFBP-WS, and piFBP, the iteration trends of the BIdx and NIdx of various materials are plotted in Figure 4-5.

For algorithm piFBP-W, BIdx curves in Figure 4-5a are significantly reduced in the first several iterations. However, due to the increasing noise, both BIdx and NIdx diverge after four iterations.

The BIdx curves of algorithms piFBP-WS and piFBP both converged to zero after three iterations. As water correction could reduce the nonlinearity of the projection data, so piFBP-WS converged slightly faster than piFBP. This improvement was reflected by the fact that the BIdx curve of bone in Figure 4-5b had smaller oscillation magnitudes than that in Figure 4-5c. As for the NIdx, there were no obvious differences between the curves of piFBP-WS and piFBP, and all the NIdx curves approximately maintained their original noise levels. The NIdx curves of lung of the two algorithms increased slightly, which was because the small attenuation coefficient of lung made its normalized NIdx sensitive to the noise. To help readers better appreciate the BH correction process, the images reconstructed by piFBP at the 0th, 1st, 2nd, 3rd, 4th, and 10th iterations are presented in Figure 4-6

Compared with piFBP, piFBP-WS had smaller oscillation magnitudes of BIdx curves but longer computational time (Table 4-4), which was caused by the time consuming water

correction process in each iteration. Given the similar reconstruction results, piFBP is certainly a better choice.

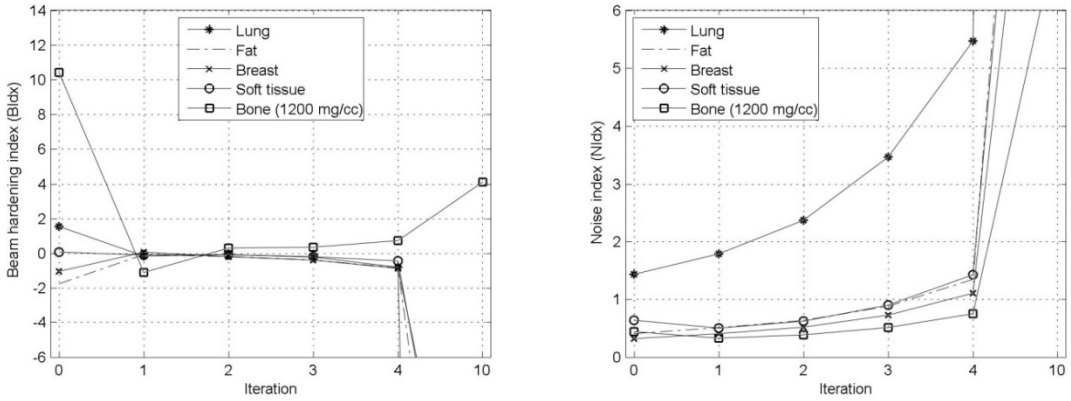

(a) BIdx and NIdx of algorithm piFBP-W

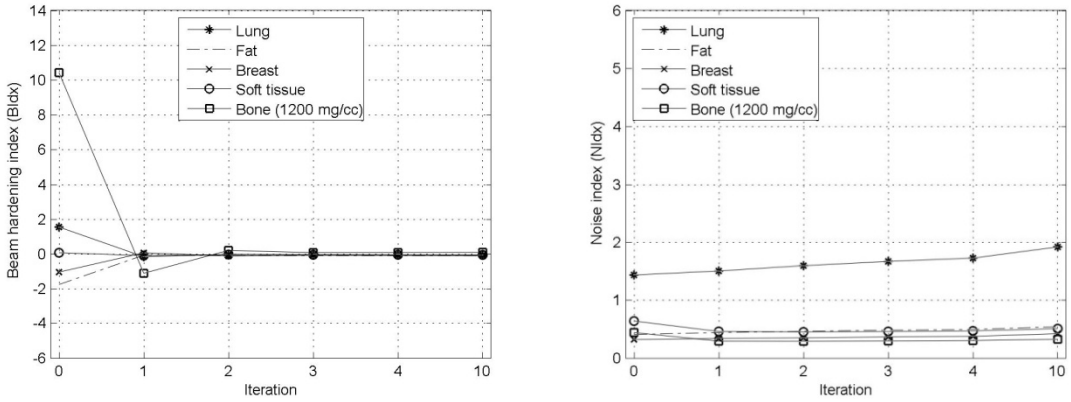

(b) BIdx and NIdx of algorithm piFBP-WS

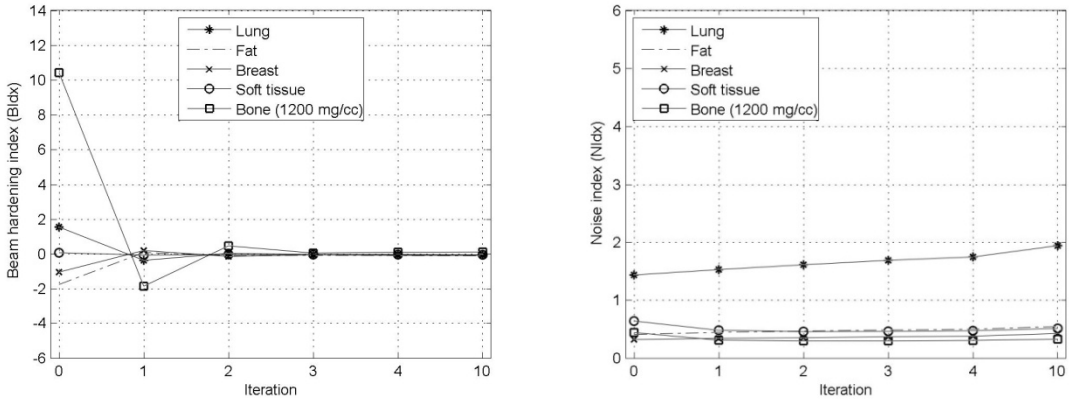

(c) BIdx and NIdx of algorithm piFBP

Figure 4-5: Iteration trends of BIdx and NIdx of various materials in the oval phantom for algorithms (a) piFBP-W, (b) piFBP-WS, (c) piFBP.

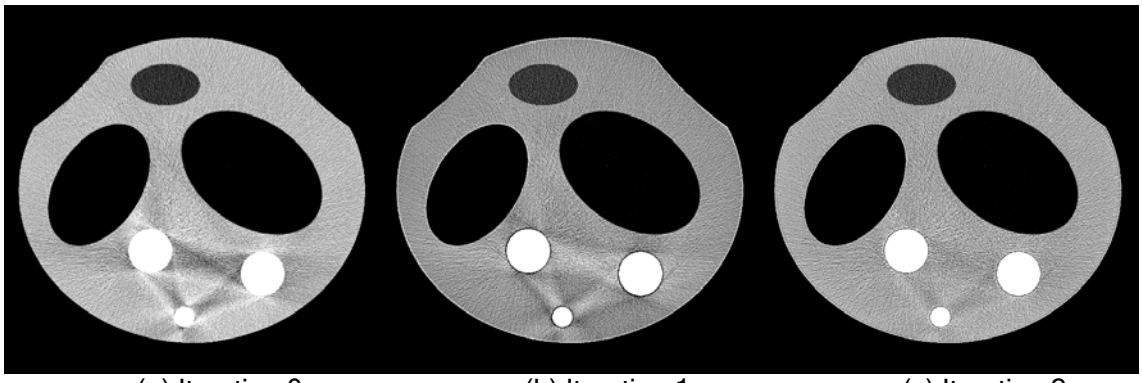

(a) Iteration 0. (b) Iteration 1. (c) Iteration 2.

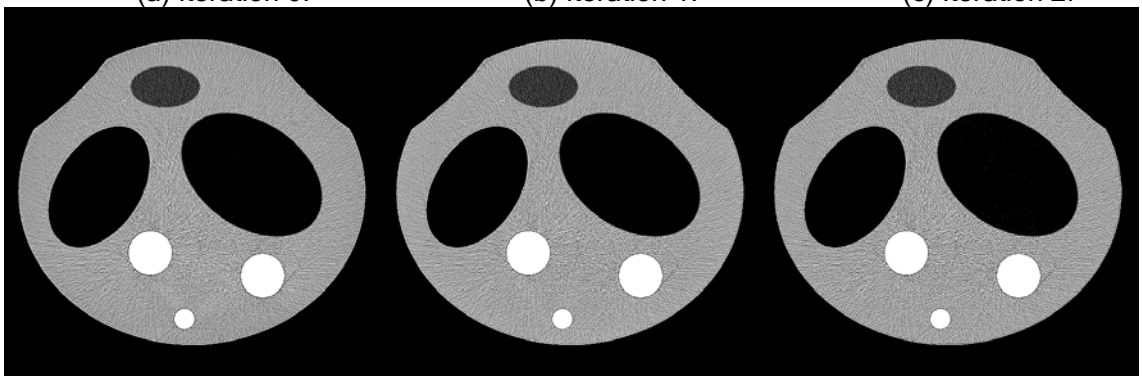

(d) Iteration 3. (e) Iteration 4. (f) Iteration 10.

Figure 4-6: Images reconstructed by piFBP at the (a) 0th, (b) 1st, (c) 2nd, (d) 3rd, (e) 4th, and (f) 10th iterations. Window level = 40 HU and window width = 100 HU.

Table 4-4: The comparison of computational speeds between piFBP-WS and piFBP.

	Iterations	Time/Iteration	Total Time
piFBP-WS	4	21 sec	84 sec
piFBP	4	7 sec	28 sec

4.3.1.3 Phantom Size Test

The effect of phantom size to different body tissues is illustrated in Figure 4-7. For FBP (dashed lines, 80 kVp), soft tissue maintained low BIdx values because its attenuation property was similar to that of water. Other materials were either underestimated or overestimated due to the BH effect. Among those materials, bone values not only

significantly deviated from the expected values, but showed a large variation across different phantom sizes. For piFBP (dotted lines, 80 kVp), negligible BIdx values for any body tissue and phantom size showed that piFBP possesses stable reconstruction ability across phantom size.

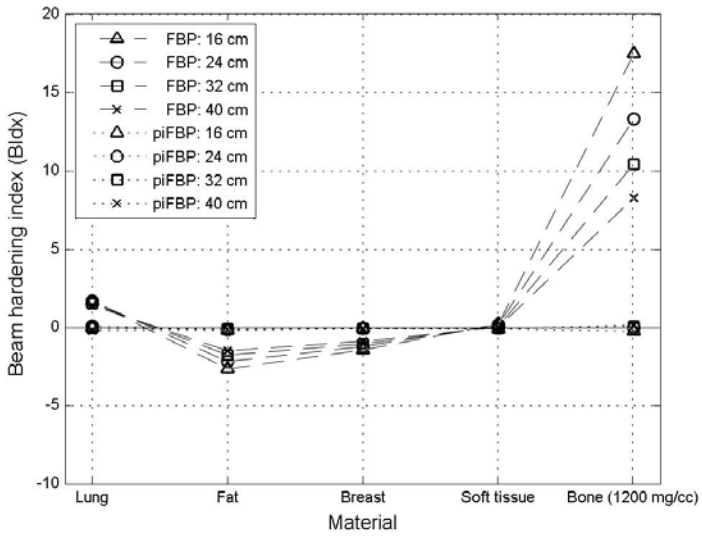

Figure 4-7: Phantom size test results. By varying phantom size (triangle: 16 cm; circle: 23 cm; square: 30 cm; cross: 37 cm), BIdx's are plotted for different materials and algorithms (dashed line: FBP; dotted line: piFBP). All simulations in this test used the 80 kVp spectrum.

4.3.1.4 Spectral Type Test

The effect of the spectrum choice to different body tissues was reflected in figure 8. All simulations in this test used the same 32 cm oval phantom. For FBP (dashed lines), soft tissue still maintained low BIdx values like the results in Figure 4-8, but the other body tissues had relatively larger magnitudes of variation. In contrast, PE-IFPB (dotted lines)

showed negligible BIdx values for different materials and spectra, which proved its stable reconstruction ability associated with the spectrum.

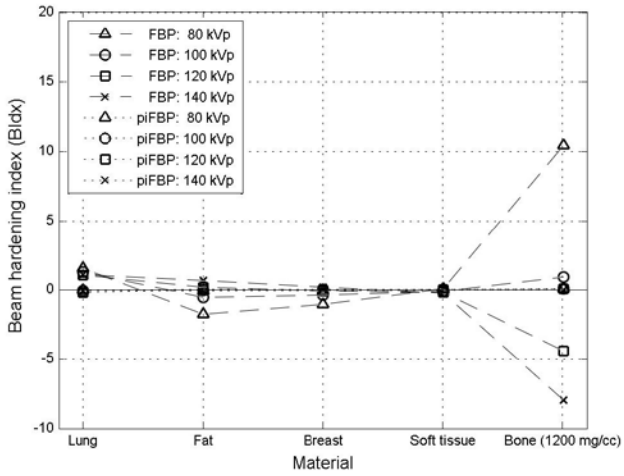

Figure 4-8: Spectral test results. By varying x-ray spectrum (triangle: 80 kVp; circle: 100 kVp; square: 120 kVp; cross: 140 kVp), BIdx's are plotted for different materials and algorithms (dashed line: FBP; dotted line: piFBP). All simulations in this test used the 32 cm diameter phantom.

4.3.1.5 Spectral Mismatch Test

The results of the spectrum mismatch test are shown in Figure 4-9. When the mismatch spectra were harder than the correct spectrum (80 kVp), the BIdx's of all tissues increased to compensate the decreased photon numbers in the low energy range. The reverse was the case for softer spectra. For the spectra with largest NRMSDs of -9% and 9%, the BIdx range increased from [-0.1, 0.1] to [-5.1, 4.5]. Based on our recent spectrum measurement technique [103], an experimental accuracy of $\pm$3.4% is readily achievable for the 80 kVp spectrum. Therefore, the BIdx range could be reduced down to [-1.8, 1.6], which was smaller than that of FBP with the correct spectrum (i.e., [-1.8, 10.4]). If water calibration is available,

the BIdx range could be further reduced by subtracting the offset value of water. This test suggested that piFBP could moderately tolerate the mismatch spectra.

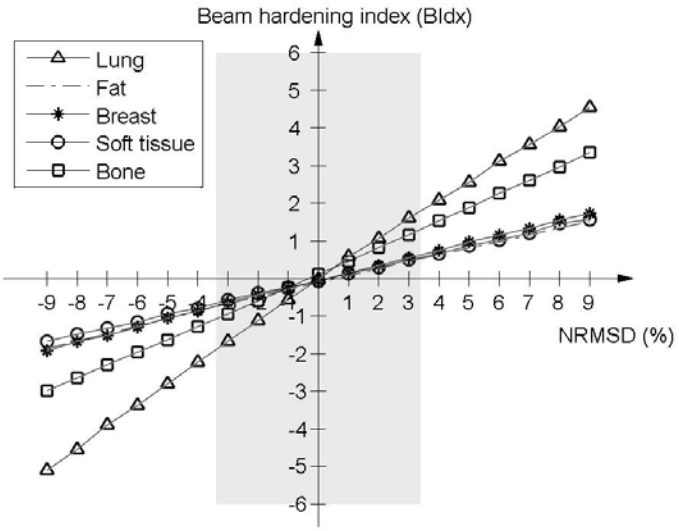

Figure 4-9: Spectrum mismatch results. BIdx's of different body tissues were derived based on different mismatch spectra (80 kVp), the NRMSDs of which ranged from -9% to 9%. The projection data were simulated by using the 32 cm diameter phantom.

4.3.1.6 Base material transition test

The results of the base material transition test are plotted in Figure 4-10. Referring to the indices of Table 4-2, when water was used as the base material (group 1), only soft tissue had negligible BIdx. Adding bone as a base material (group 2) greatly reduced the bone's BIdx. Adding breast as a base material (group 3) further reduced the BIdx of breast to a negligible level. Note that fat also showed a small improvement as in this case fat was interpreted as low density breast tissue instead of low density soft tissue as the attenuation property of fat is closer to that of the breast. With the addition of fat (group 4), the BIdx

associated with fat was further reduced. Finally, adding lung as a base material (group 5) reduced lung's BIdx to a negligible level as well.

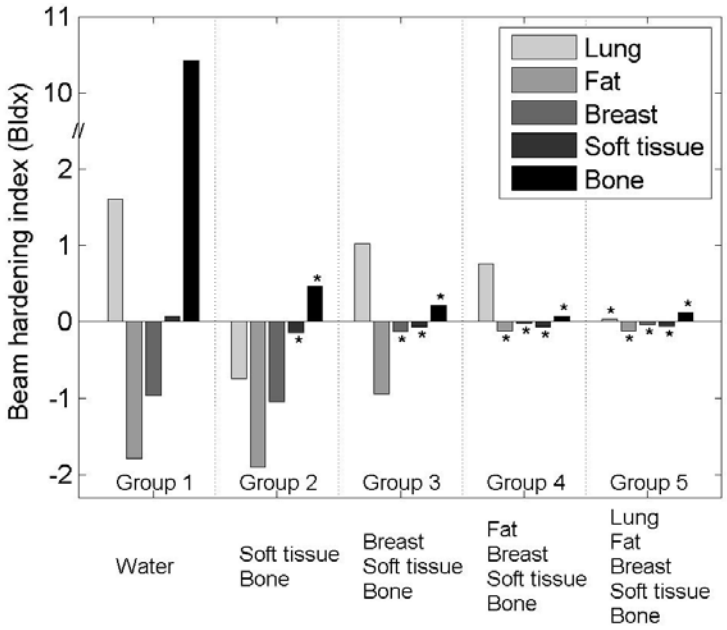

Figure 4-10: The simulation results of the base material transition test. The columns without stars indicate that the corresponding materials are not base materials. The columns with stars indicate that the corresponding materials are base materials.

4.3.2 Anthropomorphic Thorax Phantom

The reconstruction results of the anthropomorphic thorax phantom are presented in Figure 4-11. The three columns from left to right are the images reconstructed by algorithms FBP (70 keV), FBP (80 kVp), and piFBP (80 kVp), respectively. To facilitate visually comparison, from the first row to the third row, the images were adjusted to different windows, i.e., standard window (-20/300), soft tissue window (60/240), and lung window (-

800/200). The percent relative error images with window level 0%/20% are shown in the last row for the attenuation value accuracy comparison.

The images in the first column (Figure 4-11) were reconstructed by FBP (70 keV). Because of using a mono-energetic spectrum, no BH artifacts or metal artifacts were noticeable. We used the actual phantom data as benchmark images for the test comparisons.

The images reconstructed by FBP (80 kVp) are shown in the second column (Figure 4-11). As compared with the images reconstructed by FBP (70 keV) in the first column, the BH artifacts due to the metal implant and the bones severely deteriorated the image quality. For example, the metal implant on the right clavicle resulted in strong dark streaks on various body tissues, such as fat (standard window), soft tissue (soft tissue window), and lung (lung window). In addition, the bones also created strong artifacts. For example, in the soft tissue window, the streaks between sternum and vertebral column created false appearance on the heart, which obscured the real anatomical structures, and complicated the interpretation process. In addition to the visible artifacts, the invisible BH effect, i.e., voxel accuracy, could be visually assessed by the relative error image. Similar with the results revealed in the last section, fat and breast tended to be underestimated, but lung and bones tended to be overestimated.

The images in the last column were reconstructed by piFBP (80 kVp). In comparison with FBP (80 kVp), the streaks caused by the bones and the metal implant disappeared, and the image appearance was almost the same with the images reconstructed by FBP (70 keV).

The relative error image in the last row was almost uniformly zero values, which indicated high reconstruction accuracy of the piFBP algorithm.

The quantitative results of the three reconstruction algorithms are listed in Table 4-5. Strong streak artifacts were avoided during the measurements. The first row is the results of FBP (70 keV). All the BIdx values were zeros due to mono-energetic spectrum, except the BIdx value of the metal implant, which was caused by photon starvation phenomenon [104]. For the FBP (80 kVp), strong BH effect could be observed from the significantly deviated BIdx values. As the 80 kVp spectrum had more low energy photons, the photon starvation phenomenon was aggravated. The NIdx values slightly increased because of the spectral difference. For piFBP, the BIdx values of all materials were significantly reduced and close to these of FBP (70 keV). Though some of the NIdx values of piFBP increase slightly, all the NIdx values were approximately maintained at the same level with those of FBP (70 keV) and FBP (80 kVp).

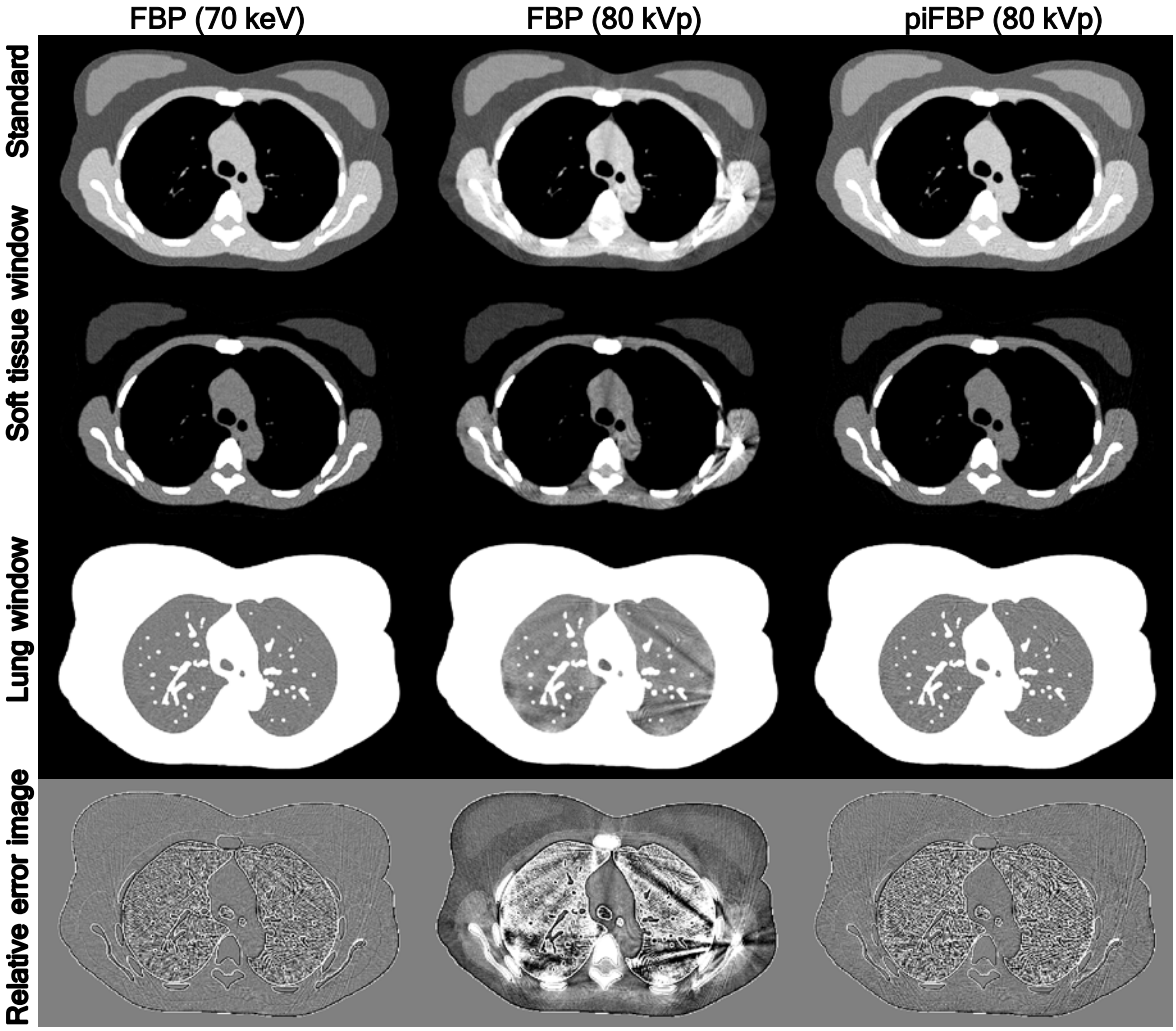

Figure 4-11: Reconstruction results of the anthropomorphic thorax phantom. The images from the first column to the third column were reconstructed by the FBP with mono-energetic spectrum (70 keV), FBP with poly-energetic spectrum (80 kVp), and piFBP with poly-energetic spectrum (80 kVp), respectively. The images from the first row to the third row are shown in different windows, i.e., fat window (-20/300), soft tissue window (60/240), and lung window (-800/200). The last row shows the percent relative error images with window level 0/20.

Table 4-5: Quantitative results of the anthropomorphic thorax phantom in terms of the beam hardening index (BIdx) and the noise index (NIdx) for different materials and reconstruction algorithms.

BIdx / NIdx	Lung	Fat	Breast Tissue	Soft Tissue	Bone (1600 mg/cc)	Metal (Ti)
FBP (70 keV)	0.0 / 4.4	0.0 / 0.9	0.0 / 0.7	0.0 / 0.8	0.0 / 0.4	-0.4 / 0.4
FBP (80 kVp)	1.8 / 5.7	-2.9 / 1.1	-1.1 / 0.9	-1.4 / 1.2	15.9 / 0.6	23.3 / 0.6
piFBP	0.3 / 6.9	-0.3 / 1.6	-0.1 / 1.1	-0.3 / 1.1	-0.3 / 0.5	1.3 / 0.9

4.4 Discussion

We proposed a fast poly-energetic iterative FBP reconstruction algorithm (piFBP) to eliminate BH artifacts and endow single spectrum CT scanners with stable quantitative reconstruction ability. The performance of the algorithm was systematically explored by an oval phantom and an anthropomorphic thorax phantom.

Five simulation tests were conducted on the oval phantom, including an algorithm test, a convergence test, a phantom size test, a spectrum type test, and a spectrum mismatch test. The algorithm test showed that both piFBP-WS and piFBP reduced the BIdx's of various tissues from [-1.8, 10.4] for FBP to [-0.1, 0.1] and maintained the NIdx's almost unchanged, which indicates the proposed algorithms could effectively eliminate the BH effect and suppress the increasing noise. The convergence test showed that piFBP converged slightly slower than piFBP-WS, but required less computational time, so only piFBP algorithm was used for the following simulation tests and recommended for clinical practice. In the phantom size and spectrum tests, the variation range of the BIdx's was reduced from [-7.5, 17.5] for FBP to [-0.1, 0.1], which indicates that piFBP possessed stable reconstruction ability across all phantom sizes (16, 24, 32, 40 cm) and spectra (80, 100, 120, and 140 kVp). The

spectrum mismatch test showed that piFBP could moderately tolerate the mismatch spectra, as the range of BIdx's of all materials only increased from [-0.1, 0.1] (derived with the correct spectrum) to [-1.8, 1.6] for the spectrum with the NRMSDs of $\pm 3.4\%$ expected from experimental measurements [103]. If water calibration information is available, the errors could be further reduced. Finally, the base material transition test indicated the importance of incorporating the correct attenuation information of the base materials in the scanned objects.

We also tested the reconstruction performance of piFBP on a realistic anthropomorphic thorax phantom in the presence of a metal implant. The simulation results showed that the BH artifacts of the body tissues could be effectively eliminated and the metal artifacts significantly reduced with four iterations, as the variation range of the BIdx's was reduced from [-2.9, 15.9] for FBP to [-0.3, 0.3] for piFBP and the BIdx of the metal implant from 23.3 to 1.3. The BIdx residue of the metal implant was due to the photon starvation.

There are three important features that distinguish our poly-energetic reconstruction algorithms from the previous ones.

First, most of the BH correction algorithms [19, 23, 28] can only incorporate one or two materials into the reconstruction process. In contrast, the adaptive base material decomposition method introduced in this work can help incorporate diverse body tissues (such as lung, fat, breast, soft tissue, and bone) and also implant metals into the

reconstruction process. The wide range of the base materials enables our algorithm to significantly reduce the BH artifacts and to quantitatively reconstruct the images.

Second, IFBP was mainly used to solve the non-uniform attenuation compensation problem in SPECT [96-99]. Our simulations showed that the conventional IFBP diverge due to the influence of noise. To improve the convergence property, we reformed IFBP by adding a smoothing kernel (piFBP) to reduce noise but maintain BH correction signals. This proposed algorithm piFBP significantly improves the convergence stability and makes it possible for BH correction.

The third important feature is the fast reconstruction speed. Different from other poly-energetic iterative algorithms [19, 79], which requires dozens or hundreds of iterations and long reconstruction time, our method can finish reconstruction with at most four iterations. If using high kVp spectra or bow-tie filters to reduce the amount of low energy photons, the iteration number can be further reduced. The fast speed suggests that the current single spectrum CT scanners can be enhanced with quantitative reconstruction ability by only updating the reconstruction algorithm. With quantitative CT, misdiagnoses can be reduced with artifact-free images, and the quantitative assessment can be improved.

If an unknown material (e.g., iron) does not possess prominent K-edges in the x-ray spectrum range, its attenuation coefficient then can be decomposed into two bases (i.e., photoelectric component and Compton component) or two distinct materials (e.g., water and bone). As there is one unknown decomposition coefficient for each base, the solution space is

doubled with respect to that of the conventional FBP algorithm. For the dual energy approaches, a patient is scanned by a dual energy scanner to obtain more information. Such that the decomposition coefficients can be computed to enable quantitative reconstruction of this unknown material, but the dual energy scanner increases the cost and the complexity of the acquisition.

In comparison, the iterative-based base material approaches assume that the scanned object is composed of known base materials (e.g., water and bone) and their mixtures (i.e., water-bone mixtures). The attenuations of the base materials can only be used to accurately compute the attenuation properties of the base materials and their mixtures, but not to accurately predict the attenuation properties of the other materials (e.g. iron). For the previous algorithms [19, 23, 28], limited base materials are incorporated, so errors arise for the other materials. In this work, a wide range of base materials were incorporated to greatly reduce this limitation, so that gradation of attenuation coefficients for various tissue types can be broadly and accurately sampled. As the attenuation at reference energy $\mu(\varepsilon_0)$ is used to compute the decomposition coefficients based on a predefined decomposition equation (Eq. 4-5) via interpolation, the size of the solution space is the same as that of the conventional FBP algorithm. Therefore, the proposed method can be applied on a single spectrum CT to reconstruct artifact-free images.

For the purpose of reconstruction stability, the two bases selected in the dual energy approaches should not be too close to each other. In contrast, close base materials will not

induce reconstruction stability problem in the iterative-based base material approaches, as base materials are mainly used to estimate the attenuation properties of their mixtures via interpolation. In fact, close base materials can provide more accurate information to reduce approximation errors, as observed through the base material transition test.

In order to improve the convergence stability, the proposed piFBP algorithm reduced two adverse factors, i.e., the noise in the correction volume due to quantum noise and electronic noise, and the inherent error due to the Fourier cut-off frequency and the filter type [100, 101]. The noise was suppressed using a smoothing kernel and the inherent error was reduced using a ramp-like filter. In comparison, Vedula and Munshi [105, 106] proposed a different strategy to improve the convergence stability. They used softer filters (e.g., Hamming filter) to reduce the influence of the noise. The inherent error induced by the softer filters was then corrected by an inherent error correction procedure. As such, they could use a piFBP-W-type (Eq. 4-14) backward updating formula to remove the beam hardening artifacts. However, as their algorithm was mainly designed for the non-destructive test (NDT), the scanned objects could only consist of distinct base materials. The adaptive base material decomposition method proposed in this work can be employed as an extension of that work, so that that algorithm can be applied in diagnostic radiology to account for the mixtures of the base materials (e.g., water-bone mixtures). Quantitative comparison of the reconstruction performance of the two different strategies remains topics for future investigation.

The smoothing kernel in Eq. 4-17 was not optimized in this work, as this study primarily aimed to improve the material quantification performance. In the future, an adaptive smoothing kernel can be used to reduce image noise and maintain anatomical details. We also plan to extend our method to CT angiography and CT perfusion, so that BH artifacts due to contrast agent materials (e.g., Iodine) can be eliminated, and quantitative concentrations of contrast agent can be retrieved for diagnostic analyses [48, 107, 108].

4.5 Conclusions

We have presented a fast poly-energetic iterative FBP algorithm (piFBP) for computed tomography. Excellent results were obtained from a series of simulations. The proposed algorithm can effectively eliminate beam hardening artifacts and accurately reconstruct the attenuation coefficients for precise quantitative imaging. The reconstruction speed is also faster than the other poly-energetic algorithms, and is promising for clinical applications. In the future research, we will try to further optimize the algorithm and to extend the algorithm to CT angiography and CT perfusion.

Chapter 5

An Efficient Poly-energetic SART (pSART) Reconstruction Algorithm for Quantitative Myocardial CT Perfusion

In quantitative myocardial CT perfusion imaging [109, 110], iodine as contrast agent is administered to the patient through intravenous injection, which can increase the absorption of x-rays and enhance the visibility of vascular structures and organs [1]. By recording the transit of the iodine through the vasculature and myocardium, time–attenuation curves (TACs) [111, 112] in the aorta (or left ventricle blood pool) and myocardium can be obtained, from which myocardial blood flow (MBF) and myocardial blood volume (MBV) [113] can be further derived to quantitatively estimate ischemic regions [109, 114]. Therefore, accurately reconstructing the iodine concentration is of great importance to the quantitative assessment of the myocardial CT perfusion imaging.

In perfusion CT examinations, high concentration iodinated contrast agent can induce strong beam hardening artifacts as dense bone. As iodine has a prominent K-edge within the x-ray energy spectrum and possesses different attenuation properties from body tissues, the poly-energetic reconstruction method introduced in the last chapter cannot be applied to offer a viable approach for reconstruction of CT perfusion studies. In this chapter,

we propose a poly-energetic SART (pSART) algorithm to offer a viable approach for reconstruction of CT perfusion studies. A series of simulations and a phantom experiment were performed to quantitatively validate the proposed method.

The work described in this chapter has been published on the journal of Medical Physics [115].

5.1 Introduction

Some efforts have been made to account for iodinated contrast agent [29, 33], but prior efforts require either accurate segmentation techniques or precise registration techniques. Further, they cannot quantitatively model the attenuation properties of water-bone mixtures and water-iodine mixtures. For example, Joseph and Ruth [29] proposed an image-based BH correction algorithm for images containing both bone and iodine with a pre-requisite to accurately segment the images into regions of soft tissue, bone, and iodine. Stenner et al [33] developed a method to distinguish these three regions by measuring the voxel dynamics, which requires a registration of the images within a time series in reference to one image set. However, patient motions, such as these from breathing or heart beating, pose a challenge to the accuracy of the registration process. Both of the aforementioned methods use the same mass attenuation coefficient curves of bone and iodine for their corresponding regions and do not model the transitional effects of water-bone and water-iodine mixtures. As a result, while they can reduce visible BH artifacts, they cannot accurately reconstruct the CT numbers of those mixtures.

In this chapter, we propose a new poly-energetic Simultaneous Algebraic Reconstruction Technique (pSART) algorithm. In contrast to the previous methods, our algorithm can incorporate the knowledge of various base materials (e.g., fat, breast, soft tissue, bone, and iodine) and the spectrum information into the reconstruction process. As each voxel is allowed to be a mixture of two most suitable base materials, the subtle attenuation differences of bones of different densities and of iodinated voxels of different concentrations can be accurately modeled in the reconstruction process to enable precise quantification. Instead of segmenting the images into three distinct regions, i.e., soft tissue, bone, and iodine, our method only needs to coarsely segment the images into two types of regions, i.e., non-bone regions and non-iodine regions, which can be easily achieved by the current segmentation techniques [116]. As no registration is involved, our method is not influenced by patient motion artifacts. This chapter further includes a series of simulations and a phantom experiment to explore the accuracy and convergence properties of the proposed algorithm.

5.2 Methods

5.2.1 Algorithm

Let us assume that Y_{rs} are the poly-energetic measurements for the *r-th* ray (r=1,…, N_R) with the *s-th* (s=1,…, N_S) incident spectrum, where N_R and N_S are the total number of the x-ray paths and spectra, respectively. The goal is to reconstruct a target volume, as individual indexed voxel of t_v (v=1,…, N_V) in terms of the attenuation coefficient at a

reference mono-energetic energy of E_0, where N_V is the total numbers of the unknown voxels. The materials in the object are assumed to meet three requirements:

1) the object consists of N_M indexed base materials with known attenuation coefficients $\mu_m(\varepsilon)$ (m=1,…, N_M), where m=1 corresponds to air;

2) each voxel can only be a mixture of two base materials; and

3) a region type mask T_v (v=1,…, N_V) is available, defined as

$$T_v = \begin{cases} 0, & Non-bone\ voxel, \\ 1, & Non-iodine\ voxel. \end{cases} \quad 5\text{-}1$$

In the context of quantitative myocardial CT perfusion imaging, the materials normally utilized to fulfill the first requirement include air (m=1), fat (m=2), breast (m=3), soft tissue (which has similar attenuation properties with blood, m=4), iodine solution (20 mg/ml blood-iodine solution, m=5), and bone (1920 mg/cm^3 soft tissue-calcium solution, m=6). Figure 5-1 shows the attenuation coefficients [46] of those base materials. Most of the poly-energetic reconstruction algorithms use water to approximate body tissues. However, due to the difference of the attenuation properties, the CT numbers of fat and breast in the reconstructed images can deviate from the expected values [19], which can affect not only the accuracy of those voxels, but also in turn the accuracy of the other voxels within the iterative reconstruction process. By incorporating fat and breast into the reconstruction algorithm, the gradation of attenuation coefficients for various tissue types can be more accurately sampled. For convenience, we use the 20 mg/ml iodine as a base material, since the maximum iodine concentration in the vascular space is usually below 20 mg/ml [117].

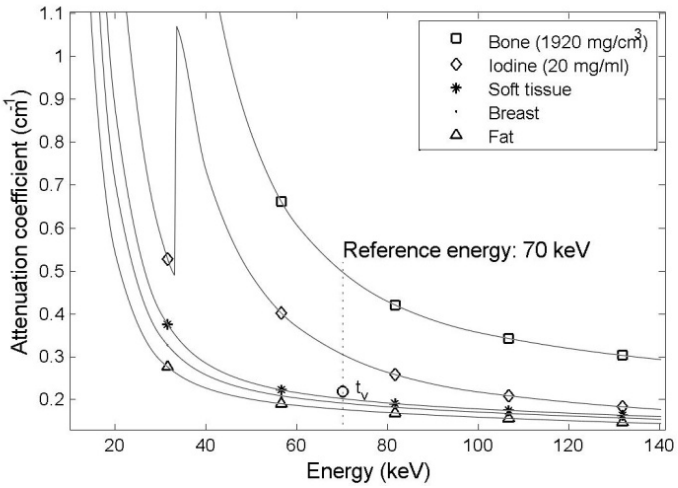

Figure 5-1: The attenuation coefficients [46] of base materials in the diagnostic x-ray energy range.

The second requirement allows us to accurately account for the subtle attenuation differences of bones and iodine concentrations. This requirement also helps reduce the complexity of the reconstruction model by ruling out mixtures formed with more than two materials. Piece-wise linear interpolation is able to be employed to estimate the attenuation properties of any given voxel.

As the attenuation curves of bone and iodine have overlap regions above the attenuation curve of soft tissue (Figure 5-1), the third requirement helps the algorithm differentiate bone and iodine and ensures that the correct attenuation curves are utilized for these two distinct materials. Instead of requiring to accurately segment the images into three types of regions [29, 33], i.e., soft tissue regions, bone regions, and iodine regions, we only require to coarsely segment the images into non-bone regions and non-iodine regions. In the non-iodine regions, materials can include any body tissues except iodine. Thereby voxel

values larger than the attenuation coefficient value of soft tissue are automatically interpreted as mixtures of bone and soft tissue. Similarly, in the non-bone regions, voxels larger than the attenuation coefficient value of soft tissue are automatically interpreted as mixtures of iodine and soft tissue. In the myocardial perfusion images, the bones are limited to sternum, ribs, and thoracic vertebrae, and those bone structure can be readily segmented based on anatomical knowledge [116, 118]. With the segmented bone structure, the region type T_v of the *v-th* voxel is set to one to bone structures, or zero otherwise.

To explain the poly-energetic forward ray-tracing strategies, we divide the discussion into three sections: iodine range $[\mu_4, \mu_5)$, bone range $[\mu_5, \mu_6)$, and body tissue range $[\mu_1, \mu_4)$, where μ_m is the *m-th* material attenuation coefficient at any preselected reference energy E_0.

5.2.1.1 Iodine Range

When $t_v \in [\mu_4, \mu_5)$ and $T_v = 0$, the *v-th* voxel is regarded as the mixture of the base materials of blood and iodine solution (20mg/ml). Its attenuation coefficient is estimated as

$$\mu(t_v, \varepsilon) = \chi_{[\mu_4, \mu_5)}(t_v)[\frac{\mu_5 - t_v}{\mu_5 - \mu_4}\mu_4(\varepsilon) + \frac{t_v - \mu_4}{\mu_5 - \mu_4}\mu_5(\varepsilon)](1 - T_v), \quad 5\text{-}2$$

where step function $\chi_{[a,b)}$ is defined as

$$\chi_{[a,b)}(t) = \begin{cases} 1 & t \in [a,b) \\ 0 & t \notin [a,b) \end{cases}. \quad 5\text{-}3$$

5.2.1.2 Bone Range

When $t_v \in [\mu_4, \mu_6)$ and $T_v = 1$, the *v-th* voxel is decomposed into the base materials of soft tissue and bone and the attenuation coefficients of those voxels are estimated as

$$\mu(t_v, \varepsilon) = \chi_{[\mu_4, \mu_6)}(t_v)[\frac{\mu_6 - t_v}{\mu_6 - \mu_4}\mu_4(\varepsilon) + \frac{t_v - \mu_4}{\mu_6 - \mu_4}\mu_6(\varepsilon)]\mathrm{T}_v . \quad 5\text{-}4$$

Note that both Eq. 5-2 and Eq. 4-2 are used to approximate bones of different densities, but the difference is that the region type mask T_v is incorporated in Eq. 5-2.

5.2.1.3 Body Tissue Range

When $t_v \in [\mu_1, \mu_4)$, the attenuation coefficient is estimated as

$$\mu(t_v, \varepsilon) = \sum_{m=1,2,3} \chi_{[\mu_m, \mu_{m+1})}(t_v)[\frac{\mu_{m+1} - t_v}{\mu_{m+1} - \mu_m}\mu_m(\varepsilon) + \frac{t_v - \mu_m}{\mu_{m+1} - \mu_m}\mu_{m+1}(\varepsilon)] . \quad 5\text{-}5$$

5.2.1.4 Reconstruction Algorithm

Combining Eq. 5-2, 5-4, and 5-5, the attenuation coefficient of the *v-th* voxel is determined as

$$\begin{aligned}\mu(t_v, \varepsilon) = & \sum_{m=1,2,3} \chi_{[\mu_m, \mu_{m+1})}(t_v)[\frac{\mu_{m+1} - t_v}{\mu_{m+1} - \mu_m}\mu_m(\varepsilon) + \frac{t_v - \mu_m}{\mu_{m+1} - \mu_m}\mu_{m+1}(\varepsilon)] \\ & + \chi_{[\mu_4, \mu_5)}(t_v)[\frac{\mu_5 - t_v}{\mu_5 - \mu_4}\mu_4(\varepsilon) + \frac{t_v - \mu_4}{\mu_5 - \mu_4}\mu_5(\varepsilon)](1 - \mathrm{T}_v) \\ & + \chi_{[\mu_4, \mu_6)}(t_v)[\frac{\mu_6 - t_v}{\mu_6 - \mu_4}\mu_4(\varepsilon) + \frac{t_v - \mu_4}{\mu_6 - \mu_4}\mu_6(\varepsilon)]\mathrm{T}_v \end{aligned} . \quad 5\text{-}6$$

The accumulated effective lengths across base materials are computed through one forward ray tracing as

$$\int_{L_r} \mu(t(\vec{x}),\varepsilon)dl \approx \sum_{v=1,\ldots,N_V} a_{rv}\mu(t_v,\varepsilon) = \sum_{m=1,\ldots,N_M} l_{rm}\mu_m(\varepsilon), \quad 5\text{-}7$$

where a_{rv} denotes the elements of the system matrix, and l_{rm} denotes the accumulated effective length of the *m-th* material for the *r-th* ray (r=1,…, N_R),

$$l_{rm} = \sum_{v=1,\ldots,N_V} a_{rv}\chi_{[\mu_m,\mu_{m+1})}(t_v) \times \begin{cases} \dfrac{\mu_{m+1}-t_v}{\mu_{m+1}-\mu_m} & m=1 \\ \dfrac{\mu_{m+1}-t_v}{\mu_{m+1}-\mu_m} + \dfrac{t_v-\mu_{m-1}}{\mu_m-\mu_{m-1}} & m=2,3 \\ \dfrac{(\mu_{m+2}-t_v)T_v}{\mu_{m+2}-\mu_m} + \dfrac{(\mu_{m+1}-t_v)(1-T_v)}{\mu_{m+1}-\mu_m} + \dfrac{t_v-\mu_{m-1}}{\mu_m-\mu_{m-1}} & m=4 \\ \dfrac{(t_v-\mu_m)(1-T_v)}{\mu_m-\mu_4} & m=5 \\ \dfrac{(t_v-\mu_m)T_v}{\mu_m-\mu_4} & m=6 \end{cases}. \quad 5\text{-}8$$

The accumulated effective length l_{rm} are repeatedly used to fast and accurately compute the energy integral calculation as

$$\begin{aligned} \overline{Y}_{rs} &= \int I_s(\varepsilon)\exp[-\int_{L_r}\mu(t(\vec{x}),\varepsilon)dl]d\varepsilon \\ &\approx \sum_{e=1,\ldots,N_E} I_{se}\exp[-\sum_{m=1,\ldots,N_M} l_{rm}\mu_{me}]\Delta e' \end{aligned} \quad 5\text{-}9$$

where I_{se} denotes the *e-th* energy bin (e=1,…, N_E) of the *s-th* spectrum (s=1,…, N_S) and N_E is the total number of the discrete energy bins.

With the estimated poly-energetic projections, algebraic reconstruction algorithms [119], statistical reconstruction algorithms [120] or FBP (Eq. 4-17) can be utilized to iteratively update voxels along the x-ray paths. In this study, the Simultaneous Algebraic Reconstruction Technique (SART) [119, 121] was used as

$$t_v^{(k+1)} = t_v^{(k)} + \frac{\sum_{rs} a_{rv} \left(\frac{\ln \overline{Y_{rs}}^{(k)} - \ln Y_{rs}}{\sum_{v'} a_{rv'}} \right)}{\sum_{r} a_{rv}}. \qquad 5\text{-}10$$

SART was initially designed for mono-energetic reconstruction based on the linear relationship between measured data lnY_{rs} and linear attenuation coefficients. But when applying this algorithm to non-mono-energetic data, the inconsistency between the data and the reconstruction algorithm causes beam hardening artifacts. The proposed poly-energetic ray tracing approach efficiently solves this inconsistency problem, and helps the reconstructed volume converge to an artifact-free image. Once image t_v is reconstructed at reference energy E_0, the value of each pixel can be shifted along the interpolated attenuation coefficient curves to generate images at any other target energy. Generally, a high keV reference energy is preferred for fast convergence (Section 3.1), and a target energy of 70 keV is used in this study as in many current clinical CT applications [1].

5.2.2 Validations

We simulated a fan beam geometry with an equiangular arc detector. Two phantoms (a cylindrical phantom and a thorax phantom) were used to generate poly-energetic projection data. The simulation parameters are listed in Table C-1 (Appendix C). Quantum noise corresponding to 4.0 x 10^5 photons per detector pixel was added to the projection data. In this work, no inhomogeneous bow-tie filtering and scattered radiation were taken into consideration. All simulations were conducted on Duke Blue Devil GPU Cluster with

NVIDIA Tesla C1060 CPUs, which consists of 30 multiprocessors (each with eight SIMD processing cores) and 4 GB of memory.

5.2.2.1 Cylindrical Phantom Simulation

A cylindrical phantom (Figure 5-2) consisting of air, fat, breast tissue, soft tissue, bone (1200 mg/cm^3), and iodinated contrast medium (8 mg/ml) was used in the study. Six simulation tests were conducted on this phantom to assess the reconstruction abilities of pSART compared with SART. All the SART reconstructions in this work used water correction technique.

The first simulation test aimed to validate the reconstruction stabilities in terms of material diversity with a 23 cm cylindrical phantom and a 100 kVp spectrum. A base material transition test was conducted in the second test to investigate the benefit of more base materials. The projection dataset acquired in the first test was reconstructed by increasing the number of the base materials. The base material groups used in this test are listed in Figure 5-3. The third test focused on the reconstruction stability in terms of phantom size. The cylindrical phantom was formed into four sizes, i.e., 16, 23, 30, and 37 cm diameter, and imaging was simulated with a 100 kVp spectrum. In the fourth simulation test, we tested the reconstruction stability as a function of changes of the spectrum (80, 100, 120, and 140 kVp). In the fifth simulation test, we compared the convergence properties of the SART and pSART with three different spectra (80, 100, and 140 kVp). In addition, we also compared the convergence property of pSART at two reference energies (70 and 140 keV). In

the last simulation test, the impact of a possible difference between the actual and the assumed spectra was investigated. Nineteen mismatch spectra were obtained by softening or hardening the correct spectrum of 100 kVp through adjusting the thickness of the inherent aluminum filtration of the x-ray tube. The normalized root mean square differences (NRMSDs) [75] of these mismatch spectra ranged from -9% to 9% with an interval of 1%. Here, negative NRMSDs indicate softened spectra and positive NRMSDs indicate hardened spectra. The parameters used in the above six simulation tests are summarized in Table 5-1.

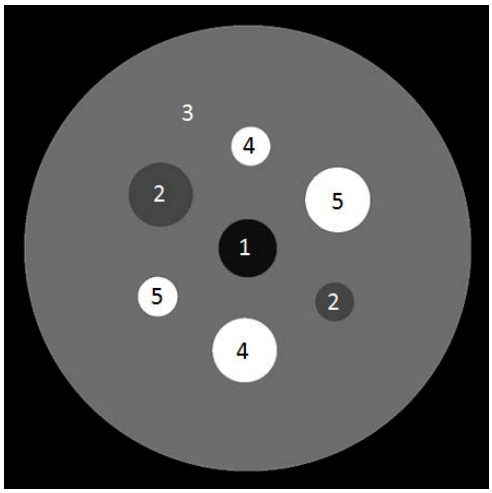

Figure 5-2: Definition of the cylindrical phantom (0.2 x 0.2 mm^2 per pixel) with (1) fat, (2) breast tissue, (3) soft tissue, (4) 8 mg/ml iodine, and (5) 1200 mg/cm^3 bone. This phantom was formed in four different cross sectional sizes, i.e., 16, 23, 30, and 37 cm in diameter.

Table 5-1: Parameter summary of simulation tests for the cylindrical phantom.

Simulation tests	Varying parameters	Fixed parameters	Individual parameters
Material test	--	Phantom size: 23 cm Spectrum: 100 kVp	SART: water correction
			pSART: E_0=70 keV
Base material transition test	Base material groups: Listed in Figure 5-3	Phantom size: 23 cm Spectrum: 100 kVp	SART: water correction
			pSART: E_0=70 keV
Phantom size test	Phantom size: 16, 23, 30, and 37 cm	Spectrum: 100 kVp	SART: water correction
			pSART: E_0=70 keV
Spectrum type test	X-ray spectrum: 80, 100, 120, 140 kVp	Phantom size: 23 cm	SART: water correction
			pSART: E_0=70 keV
Convergence test	X-ray spectrum: 80, 100, 140 kVp	Phantom size: 23 cm	SART: water correction
			pSART: E_0=70 keV, 140 keV
Spectrum mismatch test	Mismatch spectrum: NRMSD = -9%,…, 9%	Phantom size: 23 cm Spectrum: 100 kVp	pSART: E_0=70 keV

Table 5-2: Base material groups used in the base material transition test.

	Group 1	Group 2	Group 3	Group 4	Group 5
Base material	Water	Soft tissue Iodine	Soft tissue Iodine Bone	Fat Soft tissue Iodine Bone	Fat Breast Soft tissue Iodine Bone

5.2.3 Anthropomorphic Thorax Phantom Simulation

In order to further validate our reconstruction algorithm, real CT data from the database of The Cancer Imaging Archive (TCIA, http://www.cancerimagingarchive.net/) was used to create a more complex and realistic anthropomorphic thorax phantom (Figure 5-3).

Besides the body tissues such as lung, fat, breast, soft tissue, this phantom was supplemented with iodinated inserts of five different concentrations (3, 6, 9, 12, and 15 mg/ml), and bones of seven different densities (200, 400, 600, 800, 1000, 1200, and 1400 mg/cm^3). Using this phantom, the reconstruction performance of pSART was compared with that of SART.

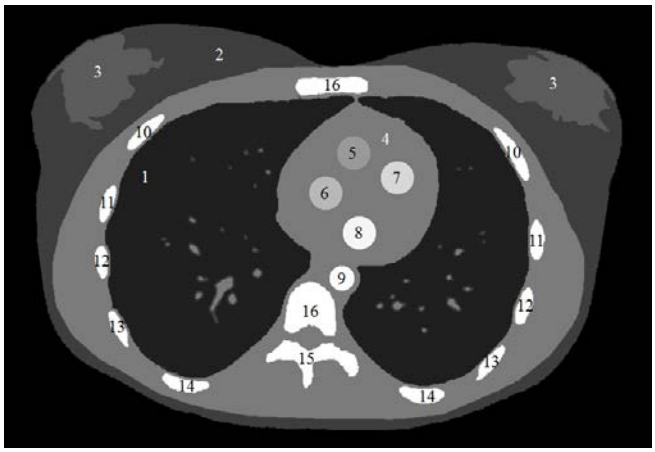

Figure 5-3: Definition of the anthropomorphic thorax phantom (0.14 x 0.14 mm^2 per pixel, 2048 x 1400 pixels) with (1) Lung, (2) fat, (3) breast tissue, (4) soft tissue, (5) 3 mg/ml iodine, (6) 6 mg/ml iodine, (7) 9 mg/ml iodine, (8) 12 mg/ml iodine, (9) 15 mg/ml, (10) 200 mg/cm^3 bone, (11) 400 mg/cm^3 bone, (12) 600 mg/cm^3 bone, (13) 800 mg/cm^3 bone, (14) 1000 mg/cm^3 bone, (15) 1200 mg/cm^3 bone, and (16) 1400 mg/cm^3 bone.

5.2.4 Phantom Measurement with Clinical CT

Phantom measurements were acquired on a clinical CT scanner (Siemens Somatom Definition Flash, Siemens Healthcare, Germany). We used axial scan mode with fixed focal spot, a 0.5s rotation time, a nominal tube voltage of 100 kVp, and a tube current of 100 mAs.

A 22 cm diameter Mercury phantom [85] was employed, which contained nine different materials as shown in Figure 5-4. The material information is listed in Table 5-3. As

the attenuation coefficient curves of polyethylene, polystyrene, acrylic, and Teflon have similar sequence order with those of fat, breast, soft tissue, and bone, these polymers were classified into non-iodine region. The iodine inserts simulated mixtures of iodine and breast tissue and were classified into non-bone region using breast tissue and 20 mg/ml breast-iodine mixture as base materials. With the composition information of this phantom already known, we were able to quantitatively validate the accuracy of pSART algorithm.

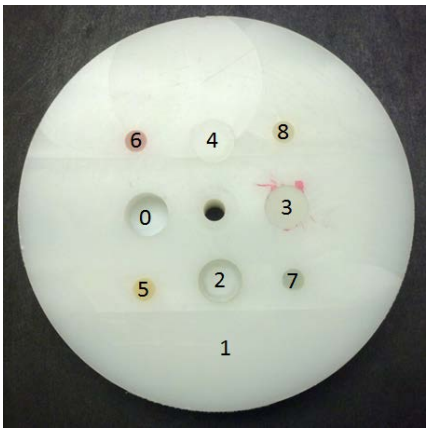

Figure 5-4: Definition of the Mercury phantom with (0) air, (1), polyethylene, (2) polystyrene, (3) acrylic, (4) Teflon, (5) 2.2 mg/ml Iodine, (6) 4.3 mg/ml Iodine, (7) 6.4 mg/ml Iodine, (8) 8.5 mg/ml Iodine.

Table 5-3: Material information of the Mercury phantom.

	Polyethylene	Polystyrene	Acrylic	Teflon	Iodine 2.2 mg/ml	Iodine 4.3 mg/ml	Iodine 6.4 mg/ml	Iodine 8.5 mg/ml
Density (mg/ml)	938	1044	1164	2163	991	993	995	998
HU	-90	-32	131	994	57	112	167	222

5.3 Results

5.3.1 Cylindrical Phantom

Figure 5-5 shows the images reconstructed by SART and pSART algorithms from the same projection dataset, which was acquired with the 23 cm cylindrical phantom and 100 kVp spectrum. Both of them were initialized with zero values and were reconstructed with 120 iterations. The images are shown with a window width of 160 HU and a window level of 70 HU. Though water correction was applied to SART (Figure 5-5a), the visible cupping artifacts (brighter pixels at the soft tissue border) were not able to be completely eliminated. Besides, the dark streak artifacts between the bones and iodinated inserts further degraded the image quality. Figure 5-5b was reconstructed by the proposed pSART algorithm at the reference energy 140 keV and target energy 70 keV. Compared with Figure 5-5a, no degradation due to beam hardening artifacts was observable, which implies that pSART was more accurate than SART.

Relative errors in terms of the attenuation coefficient (Eq. 4-19) for different materials of the cylindrical phantom are summarized in Table 5-4. For SART, because of the water correction, the soft tissue had relatively small percent error. In contrast, materials with less attenuation coefficient values than water, such as fat and breast tissue, tended to be underestimated; materials with larger attenuation coefficient values than water, such as iodine and bone, tended to be overestimated. The overall percent errors were within a 2% interval [-1.4%, 2.6%]. In comparison, the overall percent errors of pSART were within a

negligible interval [-0.1%, 0.1%]. Table 5-5 correspondingly compared the iodine concentration and bone density estimated by SART and pSART to further validate the reconstruction accuracy of the pSART algorithm.

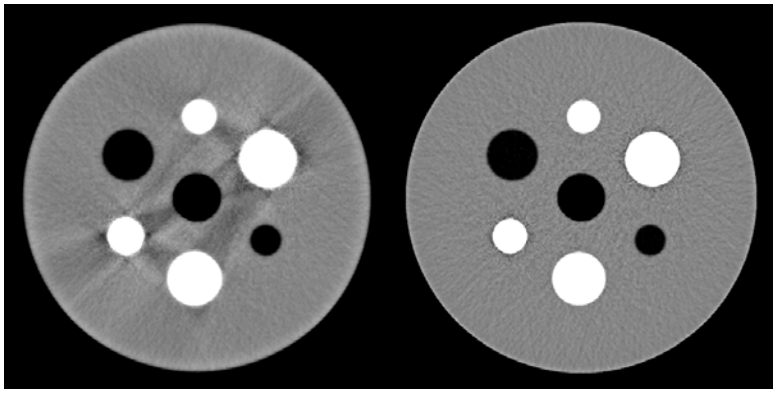

(a) SART (b) pSART

Figure 5-5: Images reconstructed by (a) water-corrected SART and (b) pSART from the same projection dataset, which was acquired with the 23 cm diameter cylindrical phantom and 100 kVp spectrum. Both of them were initialized with zero values and reconstructed with 120 iterations. The images were 512 x 512 with a voxel size of 0.5 x 0.5 mm^2.

Table 5-4: Relative errors in terms of the attenuation coefficient for different materials in the cylindrical phantom.

	Fat	Breast tissue	Soft tissue	Iodine (8 mg/ml)	Bone (1200 mg/cm^3)
SART	-1.4%	-0.2%	-0.2%	2.2%	2.6%
pSART	-0.1%	-0.1%	-0.1%	0.1%	0.1%

Table 5-5: Iodine concentration and bone density evaluated by SART and pSART.

	Iodine (8 mg/ml)	Bone (1200 mg/cm^3)
SART	8.9	1263
pSART	8.0	1201

The results of the base material transition test are plotted in Figure 5-6. Referring to the indices of Table 5-2, when only water was used as the base material (group 1), the attenuations of soft tissue and breast had small relative errors. However, other materials yielded relatively large errors due to the large difference in attenuation with water. Adding soft tissue and iodine as base materials (group 2) reduced their relative errors, especially for the iodine. With the addition of bone (group 3), the relative error associated with bone was further reduced. The relative error of fat was also reduced because the strong BH effect due to bone was suppressed. Adding breast as a base material (group 4) reduced the relative error of breast to a negligible level. Note that fat also showed a small improvement as in this case fat was interpreted as low density breast tissue instead of low density soft tissue as the attenuation property of fat is closer to that of the breast. Finally, adding fat as a base material (group 5) reduced fat's relative error to a negligible level as well.

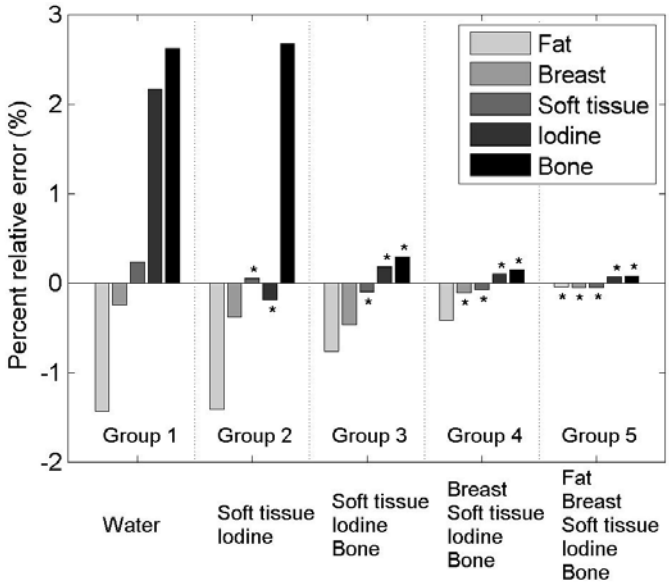

Figure 5-6: The simulation results of the base material transition test. The columns without stars indicate that the corresponding materials are not base materials. The columns with stars indicate that the corresponding materials are base materials.

The effects of the phantom size and spectrum type are presented in Figure 5-7. For SART, soft tissue maintained low relative percent errors due to water correction; fat and breast tissue were continuously underestimated for all phantom sizes and spectra; Iodine and bone showed more complicated nonlinear changes – they were overestimated for certain size phantoms or spectra, but underestimated for others. The large variation due to the spectrum (i.e., [-7.5%, 12.1%]) compared to that due to the phantom size (i.e., [-2.5%, 4.5%]) indicated that spectrum had a larger influence on the accuracy of voxel values. However, compared to SART, pSART yielded negligible relative errors (i.e., [-0.1%, 0.1%]) for all materials in the two tests and showed good reconstruction stability across phantom size and spectrum type.

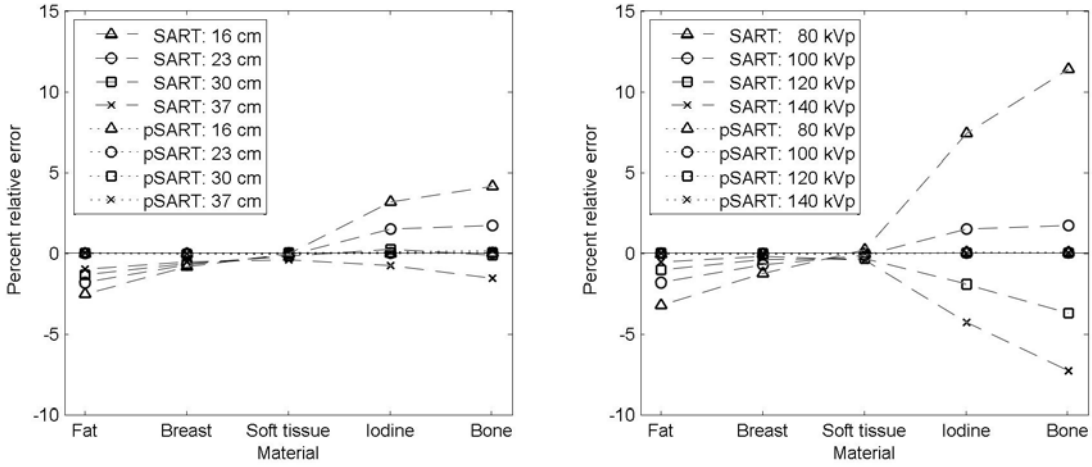

(a) Phantom size test results (b) Spectrum type test results

Figure 5-7: (a) Phantom size test results and (b) spectrum type test results. Percent relative errors are plotted for different materials (fat, breast tissue, soft tissue, 8 mg/ml iodine, and 1200 mg/cm3 bone) and reconstruction algorithms (dashed line: SART; dotted line: pSART).

The results of the convergence test for different spectra are illustrated in Figure 5-8. For SART (Figure 5-8a), the curves did not change after 100 iterations. However, because of nonlinear beam hardening effect, none of the reconstructed attenuation values of bone and iodine converged to the expected values. The reconstructed attenuation values of fat and breast tissue were close to the expected values, but their relative errors (about -1.1% to -3.2%) were still significant. Soft tissue values were relatively accurate because of similar attenuation properties with water.

In Figure 5-8b, the three kVp spectrum datasets were reconstructed by pSART. Similar with SART, the values did not change after 100 iterations. However, different from SART, the attenuation values reconstructed by pSART converged to the expected values

associated with the target energy. Besides, the dataset of the low kVp spectrum possessed fastest convergence speed among the three datasets.

Figure 5-8c depicts the attenuation convergence curves of the same spectra but at higher reference energy of 140 keV. One significant improvement was faster convergence speed for all spectrum datasets. Instead of requiring more than 100 iterations at the reference energy of 70 keV, the attenuation values reached the expected attenuation values at the *50-th* iteration.

SART generally needed approximately 100 iterations to reconstruct a dataset of 1152 projections and each iteration cost about 4s. For pSART, each iteration costs about 5s, but by selecting higher reference energy, the number of iterations could be reduced to 50 leading to a shorter computational time than that of SART (Table 5-6). This implies remarkable reconstruction efficiency of the proposed algorithm.

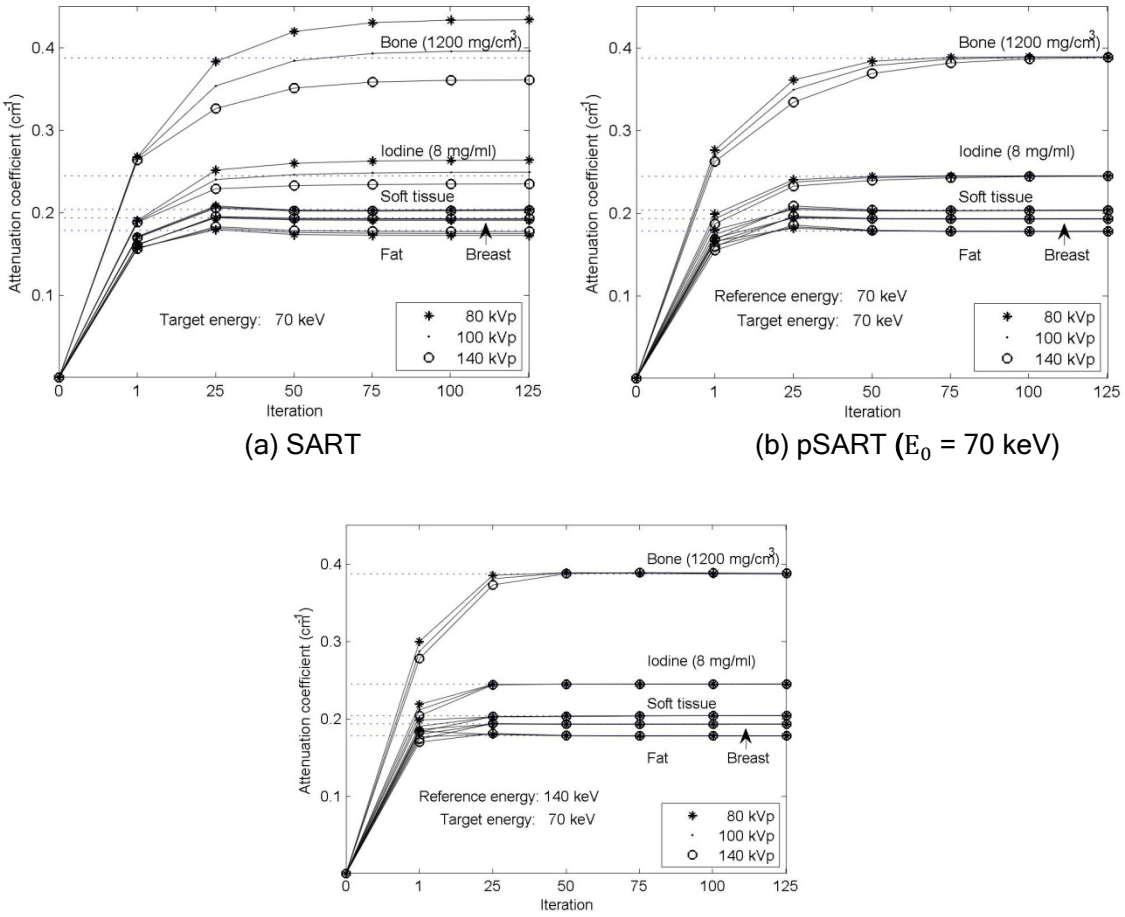

(a) SART

(b) pSART (E_0 = 70 keV)

(c) pSART (E_0 = 140 keV)

Figure 5-8: Convergence test results for different spectra (asterisk: 80 kVp; dot: 100 kVp; circle: 140 kVp) of the (a) SART algorithm, (b) pSART algorithm at reference energy E_0=70 keV, and (c) pSART algorithm at reference energy E_0=140 keV. Attenuation convergence curves are plotted for the materials in the 23 cm diameter phantom (from bottom to top: fat, breast tissue, soft tissue, 8 mg/ml iodine, and 1200 mg/ml bone) under three different x-ray spectrum (star: 80 kVp; dot: 100 kVp; circle: 140 kVp).

Table 5-6: Comparison between SART and pSART in terms of computational time.

	Iterations	Time/Iteration	Total Time
SART	100	4 sec	7 min
pSART	50	5 sec	4 min

The results of the spectrum mismatch test are shown in Figure 5-9. For the softened mismatch spectra (i.e., NRMSD < 0%), the attenuation values for all body tissues were underestimated (i.e., relative errors < 0) due to the increased photon number in the low energy range. The reverse was the case for the hardened spectra. The relative error range was increased from [-0.1%, 0.1%] to [-5.1%, 4.5%] for the spectrum with largest NRMSD of-9% and 9%. We recently proposed a robust spectrum measurement technique [103], which showed that an experimental accuracy of ±1.6% is readily achievable. Therefore, the relative error range could be reduced down to [-0.9%, 1.5%], which was smaller than that of SART with the correct spectrum (i.e., [-1.9%, 2.1%]). If water calibration is available, the relative error range could be further reduced by subtracting the offset value associated with water. This finding shows that pSART can moderately tolerate the mismatch spectra.

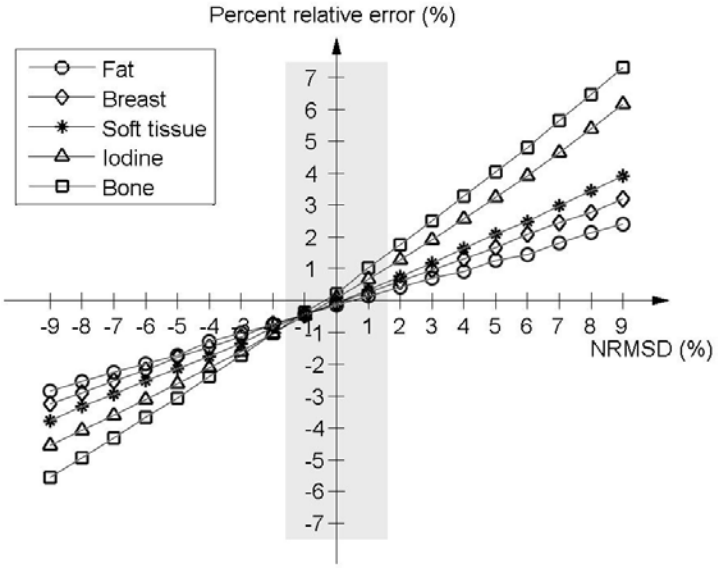

Figure 5-9: Spectrum mismatch results. Percent relative errors of different body tissues were derived based on different mismatch spectra (80 kVp), the NRMSDs of which ranged from -9% to 9%. The projection data were simulated by using the 23 cm diameter phantom.

5.3.2 Thorax Phantom

The reconstruction results of the anthropomorphic thorax phantom are shown in Figure 5-10. The images simulated at 70 keV and reconstructed by SART are presented in the first column for reference. The images reconstructed by SART and pSART simulated with the same poly-energetic projection dataset (80 kVp) are presented in the second and third columns, respectively. To further facilitate visual comparison, the images are shown with the standard window (-25/350) in the first row and with the soft tissue window (50/100) in the second row. The relative difference between the reconstructed images and the phantom (Figure 5-10) are shown in the last row with a window/level of 0%/20%. All of them were initialized with zero values and used 200 iterations to reach full convergence. The images in

the first column (Figure 5-10) were reconstructed by FBP (70 keV). Using a mono-energetic spectrum, no beam-hardening artifact was present. The difference image in the third row had approximately average zero values. The bright/dark boarders around the high frequency edges were due to the partial volume effect.

For the SART (80 kVp) algorithm, the beam-hardening effect resulted in dark streaking artifacts around the dense bones and also in the heart region. For example, in the soft tissue window, the dark streaks significantly changed the original uniform soft tissue on the two sides of the sternum. In the heart region, the streaking artifacts were induced by both the bones and the iodinated inserts. In addition to the visible artifacts, voxel value inaccuracies could be visually appreciated in its difference image. In the lung region, streaks due to the dense bones created non-uniformities that could be readily observed. Consistent with the results showed in the last section, fat and breast tended to be underestimated, and bones and iodinated inserts tended to be overestimated. The relative errors of the soft tissue were relatively small due to the water correction except for voxels between the high attenuation materials.

The images in the last column were acquired at 80 kVp and reconstructed by pSART. In comparison with SART (80 kVp), there were no apparent streak artifact, and the image appearance was almost the same with that of our reference image (SART, 70 keV). Other than the partial volume artifacts, the difference image in the last row had an average zero value, which indicates the high reconstruction accuracy of the pSART algorithm.

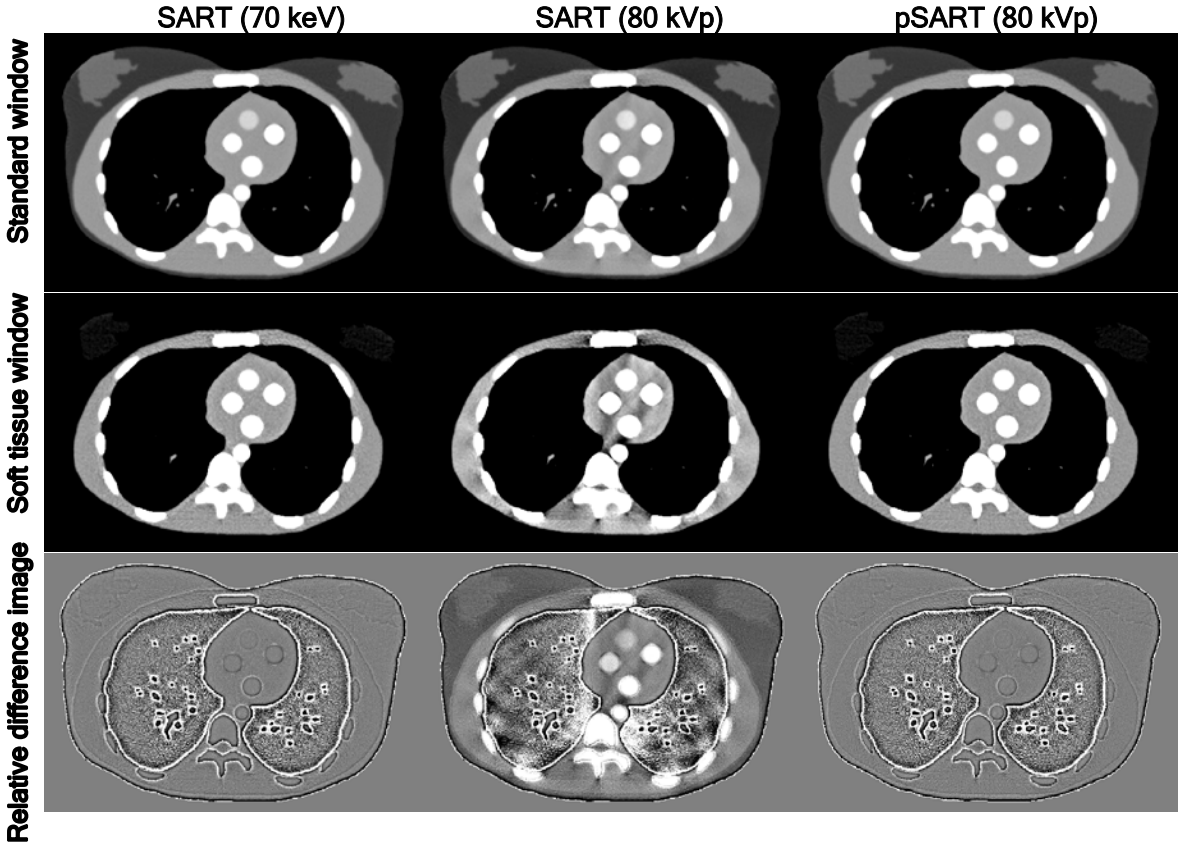

Figure 5-10: Reconstruction results of the anthropomorphic thorax phantom. The images from the first column to the third column were reconstructed by the SART (70 keV), SART (80 kVp), and pSART (80 kVp), respectively. The images from the first row to the second row are shown in different windows, i.e., fat window (-25/350) and soft tissue window (50/100). The last row shows the relative difference images with window level 0%/20%. All of them were initialized with zero values and used 200 iterations. The images were 512 x 350 with a voxel size of 0.56 x 0.56 mm^2.

For quantitative comparison, Figure 5-11 shows the measured CT numbers of different materials in the images reconstructed by SART (80 kVp) and pSART (80 kVp) against the theoretical CT numbers. In Figure 5-11a, the CT numbers of fat and breast of the SART algorithm were about 20 HU lowers than the expected values. The soft tissue was close to the expected value because of the water correction, but still deviated slightly from

the expected value. In contrast, the results of pSART showed good agreement with the expected values. In Figure 5-11b, the results of various iodinated inserts were plotted, and the iodine concentration scale was added to the right-y axis for reference. For SART, Iodinated inserts were constantly overestimated, and the discrepancy could be as large as 8 mg/ml for the 15 mg/ml insert. Therefore, iodine calibration was indispensable to the SART algorithm. In comparison, as the attenuation properties of iodine had been modeled into the pSART algorithm, the measured values of pSART were in accordance with the expected values for all inserts. Thus, no iodine calibration was required. The quantitative results of various density bones were presented in Figure 5-11c, and the bone density scale was added to the right-y axis for reference. For the SART, the bones were also constantly over-estimated, and the inaccuracy in the bone density estimation could be as large as 400 mg/cm^3 for the 1400 mg/cm^3 bone. However, the proposed algorithm accurately reconstructed the density values of all bones.

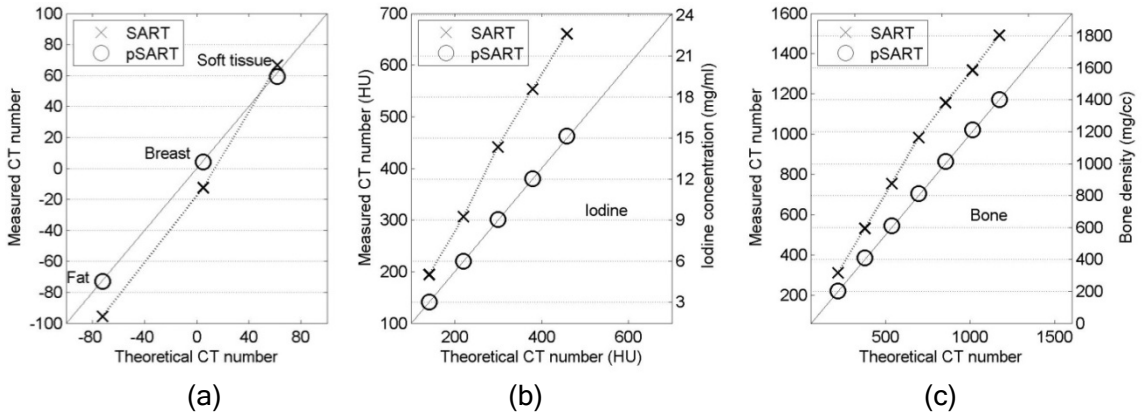

Figure 5-11: Measured CT numbers of different materials from images reconstructed by SART (crosses) and pSART (circles) were plotted against the theoretical CT numbers for (a) fat, breast, and soft tissue, (b) iodinated inserts of different concentrations, and (c) bones of different densities.

5.3.3 Phantom Measurement with Clinical CT

Reconstruction results of the Mercury phantom using a clinical CT scanner are shown in Figure 5-12. With SART, due to the poly-energetic spectrum, strong streak artifacts (the upper arrow in Figure 5-12a) between the Teflon insert and the 8.5 mg/ml Iodine insert were visible in the reconstructed image. Ring artifacts caused by the iodine inserts (the lower arrow in Figure 5-12a) also deteriorated the image quality. The quantitative results (Table 5-7) showed that the relative errors across the materials spread in a large range, i.e., [-2.0%, 4.1%]. The errors of the estimated concentrations of the iodine inserts could be as large as 1.9 mg/ml for the 8.5 mg/ml iodine insert (Table 5-8). In contrast, the image reconstructed by pSART (Figure 5-12b) was free of artifacts. The errors across the materials were reduced to a small range [-0.4%, 0.3%] and the iodine concentrations were accurately determined with absolute errors less than 0.2 mg/ml.

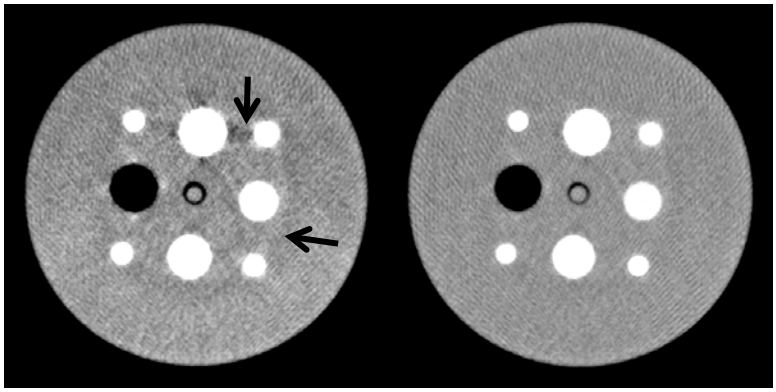

(a) SART (b) pSART

Figure 5-12: Images reconstructed by (a) water-corrected SART and (b) pSART from the same projection dataset, which was acquired with the 22 cm diameter Mercury phantom and 100 kVp spectrum. Window level = -100 HU and window width = 100 HU. The images were 512 x 512 with a voxel size of 0.5 x 0.5 mm^2.

Table 5-7: Relative errors in terms of the attenuation coefficient for different materials in the cylindrical phantom.

	Polyethylene	Polystyrene	Acrylic	Teflon	Iodine 2.2 mg/ml	Iodine 4.3 mg/ml	Iodine 6.4 mg/ml	Iodine 8.5 mg/ml
SART	-2.0%	-1.6%	-0.7%	2.0%	1.4%	2.3%	3.2%	4.1%
pSART	-0.3%	-0.2%	-0.2%	0.3%	-0.2%	-0.2%	-0.3%	-0.4%

Table 5-8: Iodine concentrations evaluated by SART and pSART.

	Iodine 2.2 mg/ml	Iodine 4.3 mg/ml	Iodine 6.4 mg/ml	Iodine 8.5 mg/ml
SART	2.8	5.3	7.8	10.4
pSART	2.1	4.2	6.2	8.3

5.4 Discussion

We developed an efficient poly-energetic SART reconstruction algorithm (pSART). A cylindrical phantom was used to investigate the reconstruction characteristics of the

proposed algorithm. The simulation results indicated that beam-hardening artifacts were completely removed, and all materials converged to the expected attenuation coefficients with absolute relative errors less than 0.1% for different phantom sizes (16, 23, 30, 37 cm) and spectra (80, 100, 120, and 140 kVp). The base material transition test indicated the importance of incorporating the correct attenuation information for the materials presented in the scanned objects. The convergence test results indicated that the reconstructions with low kVp data or high reference energies converged faster and required less number of iterations. Finally, the spectrum mismatch test showed that the range of relative errors across materials only increased from [-0.1%, 0.1%] (derived with the correct spectrum) to [-0.9%, 1.5%] for the spectra with NRMSDs of ±1.6% expected from experimental measurements. This error range was smaller than that of SART with the correct spectrum (i.e., [-1.9%, 2.1%]), which indicated that pSART could moderately tolerate spectral inaccuracies associated with experimental limits.

A realistic anthropomorphic phantom with detail anatomical structures was used to quantitatively investigate the reconstruction ability of pSART in comparison with SART. The reconstruction results showed that pSART could completely eliminate the beam-hardening artifacts and the CT numbers could be accurately reconstructed for all body tissues, bones with different densities, and iodinated inserts with different concentrations. The experiment performed on a clinical CT scanner showed that, compared with SART, pSART was able to reconstruct an artifact-free image. The quantitative results further showed that the absolute

relative errors of the voxel values estimated by pSART were less than 0.4%, which enables one to accurately determine the iodine concentrations with absolute errors less than 0.2 mg/ml.

There are three important features that distinguish our algorithm from prior efforts. (1) Diverse base materials, including fat, breast, soft tissue, bone, and iodine, are modeled into the reconstruction process, and the subtle differences of bones of different densities and iodine voxels of different concentrations are accurately modeled by our algorithm. Thus we completely eliminate beam hardening artifacts and also significantly improve the CT number accuracy. (2) Our algorithm does not require advanced segmentation techniques or registration techniques to precisely segment the images into regions of soft tissue, bone, and iodine. We only need to coarsely segment the images into two types of regions, i.e., non-bone regions and non-iodine regions, which reduces the computational complexity and is easily achieved by the current anatomical based segmentation methods [116, 118]. As no registration is involved, our method does not suffer from patient motion artifacts. (3) When using low kVp spectra and high reference energies, the reconstruction efficiency of the poly-energetic algorithms (e.g., pSART) in terms of convergence speed surpasses that of their corresponding mono-energetic algorithms (e.g., SART).

In previous literature [34-36], if K-edge materials are absent, the material in each voxel can be decomposed into two bases (i.e., photoelectric component and Compton component) or two distinct materials (e.g., water and bone). This decomposition approach

can quantitatively reconstruct an object of unknown composition. However, as it doubles the solution space, the object has to be scanned by a dual energy scanner to obtain more information, thus increases the cost and the complexity of the scanning technology. In comparison, pSART assumes that the scanned object is composed of known base materials. The well-defined attenuation properties of the base materials are incorporated into the reconstruction process as prior information. After segmenting the images into non-iodine region and non-bone region, the attenuation property of each voxel can be uniquely indexed by its attenuation at a reference energy (E_0). As such, the size of the solution space in this work is the same as that of the SART algorithm. Overall, pSART can be applied on a single spectrum CT scanner to reconstruct artifact-free images. In a separate study (not present here), we have seen that the accuracy of the voxel values across diverse body tissues can be improved by incorporating more base materials as prior information.

One limitation of the proposed algorithm is that the voxels containing coronary artery calcification cannot be easily classified into non-iodine regions based on the patient anatomical structures. Thus those voxels are mistakenly interpreted as iodine. To avoid such misinterpretation, a future study may employ pre-contrast images to ensure that the ROIs selected for iodine concentration measurements do not contain noticeable calcifications. To further reduce noise in the reconstructed images, we can also extend this algorithm to the statistical poly-energetic reconstruction method [19, 32, 120], which can statistically model the Poisson distribution characteristics of the quantum noise. Besides, an edge-preserving

penalty term can be modeled in the maximum likelihood function to further reduce noise while possessing anatomical details. These improvements remain topics for future investigation.

5.5 Conclusions

We have presented an efficient poly-energetic SART algorithm for computed tomography. Simulation results showed that the proposed algorithm effectively eliminated beam hardening artifacts, reconstructed the accurate attenuation coefficients for precise quantitative imaging, and accelerated the reconstruction process. Future work will include extending this poly-energetic method to statistical methods, and incorporate other features, such as detector noise and regularization functions.

Chapter 6

A Segmentation-free Poly-energetic Dynamic Perfusion Imaging (pDP) Algorithm

In Chapter 5, we described an algorithm to quantify iodine in iodine-blood mixtures. However, that method cannot be directly applied to mixture of iodine with other tissues. For such imaging needs, it is possible to use the pre-contrast images as *a priori* information in the reconstruction process, if the patient motions are negligible or can be corrected by registration. In this chapter, we propose a segmentation-free poly-energetic dynamic perfusion imaging (pDP) algorithm. This algorithm assumes that the motion effect of the patient is negligible or can be corrected by registration. Pre-contrast images are employed as *a priori* information to derive linearized iodine projections from the post-contrast images. With the linearized iodine projections, iodine perfusion maps are reconstructed directly without the influence of iodine location, patient size, x-ray spectrum, or background tissue type. This work included a series of simulations on a dynamic iodine calibration phantom and a dynamic anthropomorphic thorax phantom to validate the proposed algorithm.

The work described in this chapter has been submitted to the journal of Medical Physics [122].

6.1 Introduction

In dynamic CT perfusion imaging [109, 110, 123], iodinated contrast agent is administrated to a patient through intravenous injection as a way to raise the radio opacity and to enhance the visibility of vascular structures and organs [1]. By recording the change of the CT numbers of the pre-selected ROIs during the passage of the iodine bolus, time-attenuation curves (TACs) and time-concentration curves (TCCs) can be obtained, from which blood flow (BF), blood volume (BV), and mean transit time (MTT) can be derived to help effectively diagnose different diseases. For example, cardiac myocardial perfusion imaging [48] can help detect coronary artery disease (e.g., infarcted or ischemic myocardium), assess left and right ventricular function, and evaluate for structural heart disease. Lung perfusion CT [57, 124] can help identify pulmonary emboli and differentiate between benign and malignant nodules. Researches in breast perfusion imaging [56, 125-127] shows that breast cancers could be distinguished from normal mammary glands based on the perfusion values.

The quality and accuracy of the dynamic perfusion imaging in the clinical setting has been limited by the beam hardening (BH) effect. When x-rays pass through materials, low energy photons are preferentially absorbed, which increases the mean energy of the x-rays. This phenomenon leads to various artifacts in reconstructed images, such as cupping and streaking [1]. Those artifacts can result in falsely decreased attenuation of affected tissue that may be misinterpreted as a perfusion defect [110]. As such, BH influences the accuracy of the

voxel values, which makes the quantitative evaluation of iodine perfusion challenging [128-130].

Currently, the CT perfusion imaging algorithm widely used in clinical practice is based on water-corrected [23-26] Filtered Backprojection (FBP) algorithms [109, 131]. This approach requires pre-calibrated iodine concentration curves [123, 132] across different spectra and phantom sizes, so that the errors of measured TACs or TCCs [110, 123] can be reduced. This approach takes the advantage of FBP's fast speed, but is susceptible to streak artifacts induced by high attenuation materials, such as bone, iodine, and metal.

Some efforts have been made to account for the attenuation properties of bone and iodine [29, 33], but with limited success. For example, Joseph and Ruth [29] proposed an image-based beam hardening correction algorithm to incorporate the attenuation properties of water, bone and iodine in terms of effective density. However, a pre-requisite of this method is to accurately segment these three base materials into distinct regions. Stenner et al [33] developed a method to distinguish the three regions by measuring the voxel dynamics, but they used a series of threshold-based segmentation techniques, and the voxels containing low concentration or low dynamic iodinated contrast agent could be potentially mis-interpreted as soft tissue or bone minerals. Besides, both of the two methods are limited to myocardial perfusion exam, as they only modeled the attenuation properties of blood-iodine mixture. Errors may arise in other perfusion exams, such as lung or breast perfusion

exams (see our simulation results with a dynamic anthropomorphic thorax phantom in Section 6.3.2).

In this work, a new poly-energetic dynamic perfusion imaging algorithm (pDP) is proposed. Our algorithm does not require segmentation. Assuming minimal or correctable patient motions, pre-contrast images are used as *a priori* information to derive linearized iodinated projections from post-contrast projections. With the linearized iodinated projections, artifact-free iodine maps can be reconstructed directly. As diverse base materials (e.g., lung, fat, breast, soft tissue, bone, metal implant, and iodine) are incorporated, pDP enables quantitative iodine map reconstruction independent of various influential factors such as iodine location, patient size, spectrum, and background tissue type.

6.2 Methods

6.2.1 Algorithm

A flow chart of the proposed pDP algorithm is shown in Figure 6-1. Here, r=1,…, N_R is the *r-th* ray from the x-ray source to the detector element, v=1,…, N_V is the *v-th* voxel of the target volume, and N_R and N_V are the total numbers of the x-ray paths and target voxels, respectively. With the pre-contrast measurements p_r^{pre}, the pre-contrast images t_v^{pre} are first reconstructed using poly-energetic iterative FBP (piFBP) [133]. Section 6.2.1 summarizes the theoretical bases and provides more details of this algorithm. With the post-contrast measurements p_r^{post}, intermediate post-contrast images $\tilde{t}_v^{post}$ are reconstructed as references to register pre-contrast images t_v^{pre} as a way to offset patient motions and to obtain motion-

free pre-contrast images $\tilde{t}_v^{pre}$, with which the accumulated effective lengths l_{rm}^{post} of all body tissues are computed based on the acquisition parameters of p_r^{post} and are used as *a priori* information to derive the linearized iodine projections ($l_{r,7}^{post}$). Here, m=1,…, N_M is the base material index, N_M is the total number of the base materials, and the material index of iodine is m=7. In this way, the linearized iodine projections $l_{r,7}^{post}$ can be reconstructed into artifact-free iodine maps (t_v^{iodine}) by a standard FBP algorithm. Section 6.2.1 describes the post-contrast iodine map reconstruction method in detail.

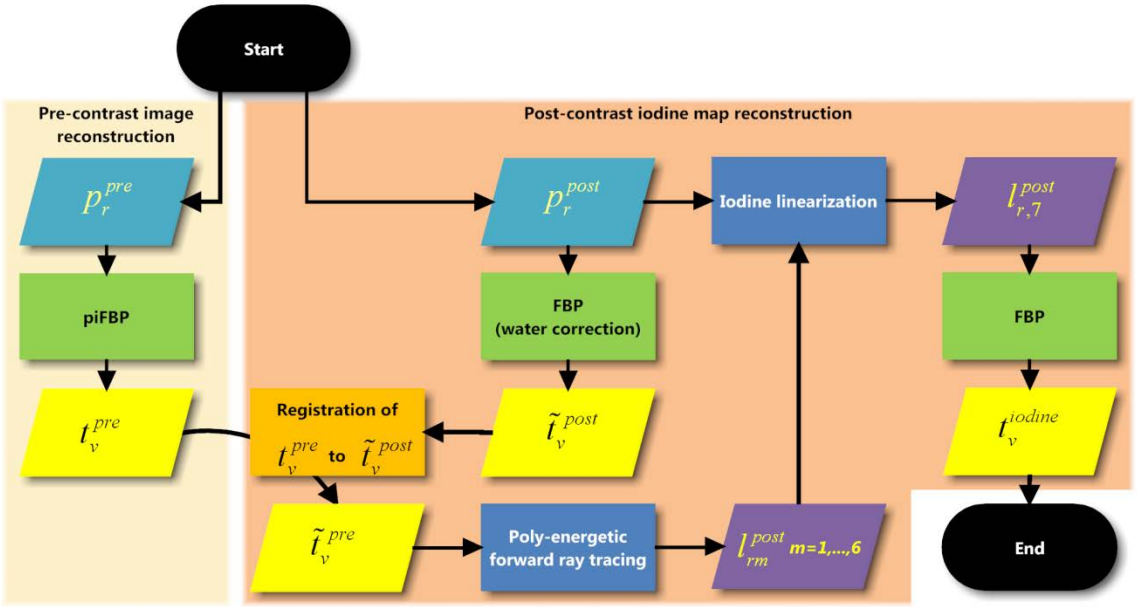

Figure 6-1: Flow chart of the proposed pDP algorithm.

6.2.1.1 Pre-contrast image reconstruction

The forward projection model for the poly-energetic x-ray beam [19] is given by

$$\bar{p}_r^{pre} = -\ln\left(\int I(\varepsilon)\exp[-\int_{L_r}\mu(\vec{x},\varepsilon)dl]d\varepsilon\right), \qquad 6\text{-}1$$

where $\bar{p}_r^{pre}$ (r=1,…, N_R) is the estimated logarithmic measurement along the *r-th* ray line L_r in the pre-contrast phase, $I(\varepsilon)$ is the spectrum (normalized to unit area), and $\mu(r,\varepsilon)$ is the unknown spatial- and energetic-related attenuation map of the object. In order to reduce the free degrees of the attenuation map $\mu(r,\varepsilon)$ and to quickly evaluate this nonlinear double integral, we propose the following adaptive base material decomposition method.

We assume that the object is comprised of N_M known base materials, and the mixture in each voxel can be decomposed to iodine and two other base materials. The base material set can be chosen based on the CT exams. For example, in thorax perfusion CT exam, the base material set can include air (m=0), lung (m=1), fat (m=2), breast (m=3), soft tissue (m=4), bone (m=5, 1920 mg/cc water-calcium solution), metal implant (m=6, e.g., titanium), and iodine (m=7). The attenuation coefficient curves [46] of the base materials in the pre-contrast phase are plotted in Figure 4-1.

With the poly-energetic iterative FBP algorithm (piFBP) described in Chapter 4, the images in the pre-contrast phase can be reconstructed as

$$\begin{cases} \mathbf{t}^{pre(0)} = \mathcal{B}\mathbf{p}_w^{pre} \\ \mathbf{t}^{pre(k+1)} = \mathbf{t}^{pre(k)} + c\mathcal{S}\mathcal{B}(\mathbf{p}^{pre} - \mathcal{F}\mathbf{t}^{pre(k)})' \end{cases} \quad 6\text{-}2$$

where $\mathbf{B}$ is the Filtered Backprojection (FBP) operator, $\mathbf{p}_w^{pre}$ is the column vector of the water corrected logarithmic poly-energetic measurements, k is the iteration index ($k \geq 0$), and c is the relaxation parameter. In this work, the relaxation parameter c was set to one. As BH artifacts are mainly low frequency signals, a smoothing operator $\mathbf{S}$ was added to suppress the noise of the correction volume and to improve the convergence stability. In this work, a

smoothing kernel of 5 x 5 pixels Gaussian low pass filter (mean=0 and sigma=1.05) was favored to provide sufficient noise suppression.

6.2.1.2 Post-contrast iodine map reconstruction

The enhancement of the post-contrast projections with respect to the pre-contrast ones is mainly due to the introduced iodine contrast agent. As the attenuation property of the iodine solvent is similar to that of soft tissue or blood, we can simply assume the increase of the voxel values is only caused by iodine element, i.e.,

$$t_v^{post} = \tilde{t}_v^{pre} + t_v^{iodine}, \tag{6-3}$$

where $\tilde{t}_v^{pre}$, t_v^{iodine}, and t_v^{post} are the *v-th* voxel values of the motion corrected pre-contrast images, the iodine maps, and the post-contrast images, respectively. Based on Eq. 4-5 and Eq. 6-3, the energy-dependent attenuation coefficient for the *v-th* voxel of the post-contrast images can be expressed as

$$\mu(t_v^{post}, \varepsilon) = \sum_{m=0,\ldots,5} \chi_{[\mu_m, \mu_{m+1})}(t_v)\left[\frac{\mu_{m+1}(\varepsilon_0) - \tilde{t}_v^{pre}}{\mu_{m+1}(\varepsilon_0) - \mu_m(\varepsilon_0)}\mu_m(\varepsilon) + \frac{\tilde{t}_v^{pre} - \mu_m(\varepsilon_0)}{\mu_{m+1}(\varepsilon_0) - \mu_m(\varepsilon_0)}\mu_{m+1}(\varepsilon)\right] + \frac{t_v^{iodine}}{\mu_7(\varepsilon_0)}\mu_7(\varepsilon)$$
. 6-4

With the above equation, the linear integral along the *r-th* ray can be approximated by the accumulated effective lengths ($l_{rm}^{post}, r = 1, \ldots, N_R$) of the base materials (*m=0,…,7*) as

$$\int_{L_r} \mu(t(\vec{x}), \varepsilon) dl \approx \sum_{v=1,\ldots,7} a_{rv}\mu(t_v^{post}, \varepsilon) = \sum_{m=1,\ldots,6} l_{rm}^{post}\mu_m(\varepsilon) + l_{r,7}^{post}\mu_7(\varepsilon). \tag{6-5}$$

As l_{rm}^{post} (m=1,…,6) can be calculated with $\tilde{t}_v^{pre}$ (Eq. 4-8) based on the post-scan acquisition parameters, the proposed method does not require the post-contrast projections to be geometrically identical to the pre-contrast projections. The effective length of iodine ($l_{r,7}^{post}$) is defined as

$$l_{r,7}^{post} = \sum_{v=1,\ldots,N_V} a_{rv} \times \frac{t_v^{iodine}}{\mu_7(\varepsilon_0)}. \tag{6-6}$$

With $l_{rm}^{post}(m = 1, \ldots,6)$ and p_r^{post}, the accumulated lengths of iodine ($l_{r,7}^{post}$) can be numerically computed by solving the following nonlinear equations using bisection method [134]

$$\begin{aligned} p_r^{post} &= -\ln\left(\int I(\varepsilon)\exp[-\int_{L_r}\mu(t^{post}(\vec{x}),\varepsilon)dl]d\varepsilon\right) \\ &\approx -\ln\left(\sum_{e=1,\ldots,N_E} I_e \exp[-\sum_{m=1,\ldots,6} l_{rm}^{post}\mu_m(\varepsilon) - l_{r,7}^{post}\mu_7(\varepsilon)]\Delta e\right). \end{aligned} \tag{6-7}$$

To suppress noise, we apply a projection space denoising operation to $l_{r,7}^{post}$ by using a 5 x 5 pixels Gaussian low pass filter (mean=0, sigma=0.8). As $l_{r,7}^{post}$is linearly related to t_v^{iodine} (Eq. 6-6), standard FBP algorithm can be used directly to reconstruct the iodine map. The iodine concentration of the *v-th* voxel can be further computed as

$$c_v = \frac{t_v^{iodine}}{\mu_7(\varepsilon_0)} \times 4933\, mg/cc, \tag{6-8}$$

where 4933 mg/cc is the density of the iodine element. With $\tilde{t}_v^{pre}$ and t_v^{iodine}, synthesized post-contrast images can then be computed by Eq. 6-3. As the attenuation curve of iodine is incorporated, the BH effect due to iodine can be effectively eliminated.

Note that the previous algorithms [29, 33, 110, 123] are limited to myocardial perfusion, as they assume that iodine can only be mixed with blood. In contrast, by allowing for any types of tissue-iodine mixtures, our method can be applied to other organ perfusion exams, such as in lungs or breasts. By choosing suitable base materials, we can further extend the proposed algorithm to cerebral, renal, and hepatic perfusion exams. For example, for the cerebral perfusion imaging exams, the base materials can include fat, white matter, gray matter, bone, and tooth. Thus, accurate artifact-free pre-contrast images can be reconstructed and used as *a priori* information to linearize the iodine projections.

6.2.2 Validations

We simulated a fan beam with an equiangular arc detector. The simulation parameters are listed in Table C-1 (Appendix C). Quantum noise corresponding to 4.0×10^5 photons per detector pixel was added to the projection data. In this work, no inhomogeneous bow-tie filtering and scattering were taken into consideration. All simulations were conducted on Duke Blue Devil GPU Cluster with NVIDIA Tesla C1060 CPUs, which consists of 30 multiprocessors (each with eight SIMD processing cores) and 4 GB of memory.

6.2.2.1 Dynamic iodine calibration phantom

A size-variable dynamic iodine calibration phantom (Figure 6-2) was designed to compare the conventional FBP-based perfusion algorithm and the proposed pDP algorithm. In the pre-contrast phase (Figure 6-2a), this phantom was composed of uniform soft tissue. In the post-contrast phase (Figure 6-2b), five groups of iodine inserts with different

concentrations (2, 6, 10, 14, 18 mg/cc) emerged from the soft tissue background. For each group, five iodine inserts with the same concentration were positioned at different radial distances. The size of this phantom was scaled to 16, 23, 30, and 37 cm diameters to simulate patients of different sizes. With this phantom, three tests, i.e., an iodine location test, a phantom size test, and a x-ray spectrum test, were performed to investigate the reconstruction stability of the algorithm. The parameters used in the three simulation tests are summarized in Table 6-1.

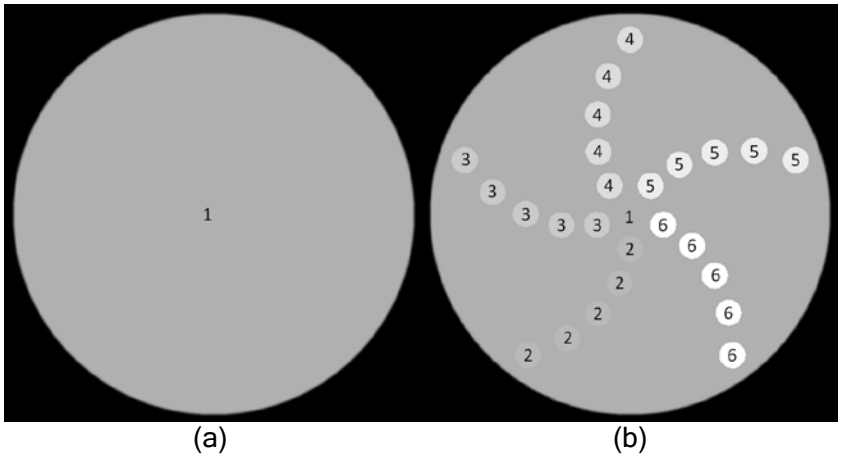

Figure 6-2: Definition of the dynamic calibration phantom (1024 x 1024 pixels). (a) In the pre-contrast phase, this phantom was only composed of uniform (1) soft tissue. (b) In the post-contrast phase, this phantom was composed of (1) soft tissue, (2) 2 mg/cc iodine insert group, (3) 6 mg/cc iodine insert group, (4) 10 mg/cc iodine insert group, (5) 14 mg/cc iodine insert group, and (6) 18 mg/cc iodine insert group.

Table 6-1: Parameter summary of the simulation tests for the dynamic iodine calibration phantom.

Simulation tests	Varying parameters	Fixed parameters	Individual parameters
Iodine location test	Radial distance of the iodine inserts	Spectrum: 80 kVp Phantom size: 30 cm	FBP: water correction pDP: E_0=70 keV
Phantom size test	Phantom size: 16, 23, 30, and 37 cm	Spectrum: 80 kVp	FBP: water correction pDP: E_0=70 keV
X-ray spectrum test	X-ray spectrum: 80, 100, 120, 140 kVp	Phantom size: 30 cm	FBP: water correction pDP: E_0=70 keV

6.2.2.2 Dynamic anthropomorphic thorax phantom

In order to further validate our reconstruction algorithm, real CT data from the database of The Cancer Imaging Archive (TCIA, http://www.cancerimagingarchive.net/) were used to create a more complex and realistic dynamic anthropomorphic thorax phantom (Figure 6-3). The phantom was assumed idealized for tissue registration and contrast enhancement.

In the pre-contrast phase (Figure 6-3a), this phantom was composed of diverse materials, i.e., (1) lung, (2) fat, (3) breast, (4) soft tissue, (5) bone (1000 mg/cc), (6) metal implant (titanium). In the post-contrast phase (Figure 6-3b), iodine perfusion resulted in different tissue-iodine mixtures, i.e., (7) lung-iodine mixture, (8) fat-iodine mixture, (9) breast-iodine mixture, and (10) soft tissue-iodine mixture. In order to simulate the dynamic wash-in and wash-out kinetics, a gamma-variate function [135] (Figure 6-4) was employed to govern the concentration changes of the iodinated contrast agent as

$$c(t) = c_{\max}(t/t_{\max})^{a} \exp[a(1-t/t_{\max})] \quad 6\text{-}9$$

The parameter a affects the rise and fall times of the function and was set to 1 in this work; the peak time t_{max} was set to the 8 seconds for all tissues; the maximum iodine concentration c_{max} at the peak time was set to 14 mg/ml for all tissues. In addition, a common set of regions of interest surrounding the left chamber (Figure 6-5) was used to assess the effect of BH artifacts induced by iodinated contrast agent in both heart chambers and aorta. With this dynamic anthropomorphic thorax phantom, poly-energetic projections were simulated from 0s to 20s with a 2s interval [33]. The projections were reconstructed by the conventional FBP algorithm and the proposed pDP algorithm. The simulation results were compared quantitatively.

Note that as this dynamic phantom was mainly used to validate the proposed algorithm, a single TAC was applied to all body tissues. This choice enabled the comparison of the impact of iodine on the reconstruction values across different background tissues.

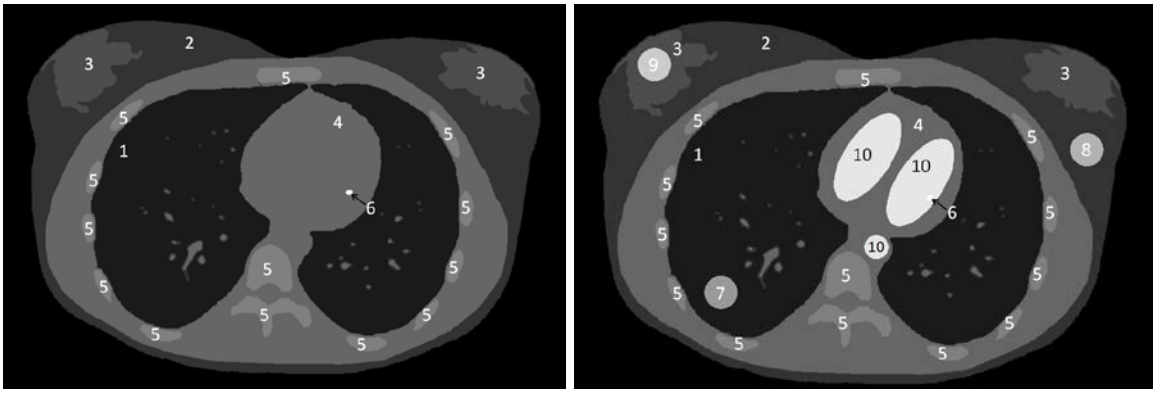

Figure 6-3: Definition of the dynamic anthropomorphic thorax phantom (2048 x 1400 pixels, 0.15 x 0.15 mm2). (a) In the pre-contrast phase, this phantom was composed of

(1) lung, (2) fat, (3) breast, (4) soft tissue, (5) bone (1000 mg/cc), and (6) metal implant (titanium). (b) In the post-contrast phase, iodine perfusion resulted in different iodine-body tissue mixtures, i.e., (7) lung-iodine mixture, (8) fat-iodine mixture, (9) breast-iodine mixture, and (10) soft tissue-iodine mixture. The TAC of those different body tissue-iodine mixtures is defined in Figure 6-4.

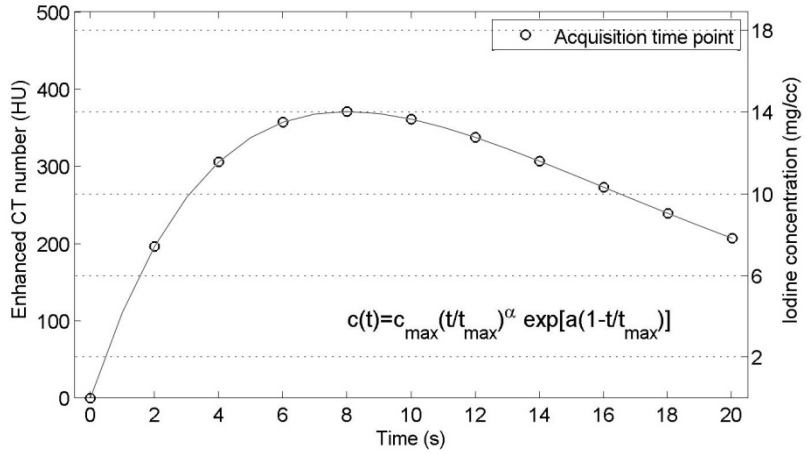

Figure 6-4: The TAC of the different body tissue-iodine mixtures. The iodine concentration scale was added to the right-y axis for reference. Ten time points were sampled from 0s to 20s with 2s interval.

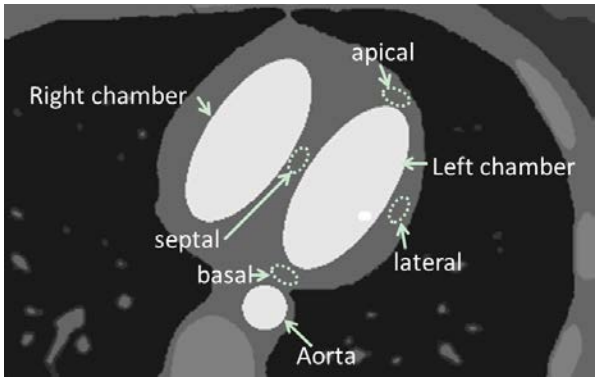

Figure 6-5: Anatomical structures in the heart region. A set of ROIs (i.e., apical, septal, basal, and lateral) was used to evaluate the BH artifacts induced by iodine in both heart chambers and aorta.

6.3 Results

6.3.1 Dynamic Iodine Calibration Phantom

Figure 6-6 shows the reconstruction results of the dynamic iodine calibration phantom in the post-contrast phase. The images in the first column were reconstructed by FBP (70 keV). Because of the mono-energetic spectrum, BH artifacts were not noticeable. The images in the first column were used as benchmarks for the rest of the comparisons. The percent relative difference image in the second row shows uniform zero values. The iodine map shown in the last row was obtained by subtracting the post-contrast image from the pre-contrast image, and it correctly retrieved all iodine inserts.

The post-contrast images reconstructed by FBP (80 kVp) are shown in the second column of Figure 6-6. Dark streak artifacts were readily visible. The percent relative difference image in the second row shows that iodine inserts were constantly over-estimated for all concentrations, which affects the accuracy of the quantitative perfusion assessment. By subtracting the post-contrast image from the pre-contrast image, we obtained the iodine map as presented in the last row. The BH artifacts were prominent in a narrow window level (0 HU/40 HU). As expected, the strength of the artifacts was positively correlated with the iodine concentration but inversely correlated with the distance between the iodine inserts. In addition, the strength of the artifacts was also positively correlated with the radial distance. For instance, for the 10 mg/cc iodine inserts, the shape of the iodine inserts near the center was round, but when approaching the phantom border, the shape was gradually deformed

to an ellipse, the long axis of which was parallel to the shortest intersection line between the x-ray path and the phantom. This phenomenon was due to the cupping effect [1]. For the iodine inserts close to the center, the x-rays from different directions were equally attenuated, so that the BH effect was isotropic and the shape of the iodine inserts could be preserved. However, for the iodine near the phantom boarder, BH effect was no longer isotropic. The directions with shorter intersection lines between the x-ray path and the phantom could induce stronger BH artifacts, because of the large amount of un-attenuated low energy photons. Water correction could not effectively eliminate this iodine-induced cupping effect.

The images in the last column of Figure 6-6 were reconstructed by pDP (80 kVp). In comparison with FBP (80 kVp), the streaks caused by the iodine inserts were totally eliminated in the post-contrast image. The relative difference image in the second row had uniformly negligible values. The iodine map in the last row was nearly identical with the iodine map obtained by FBP (70 keV).

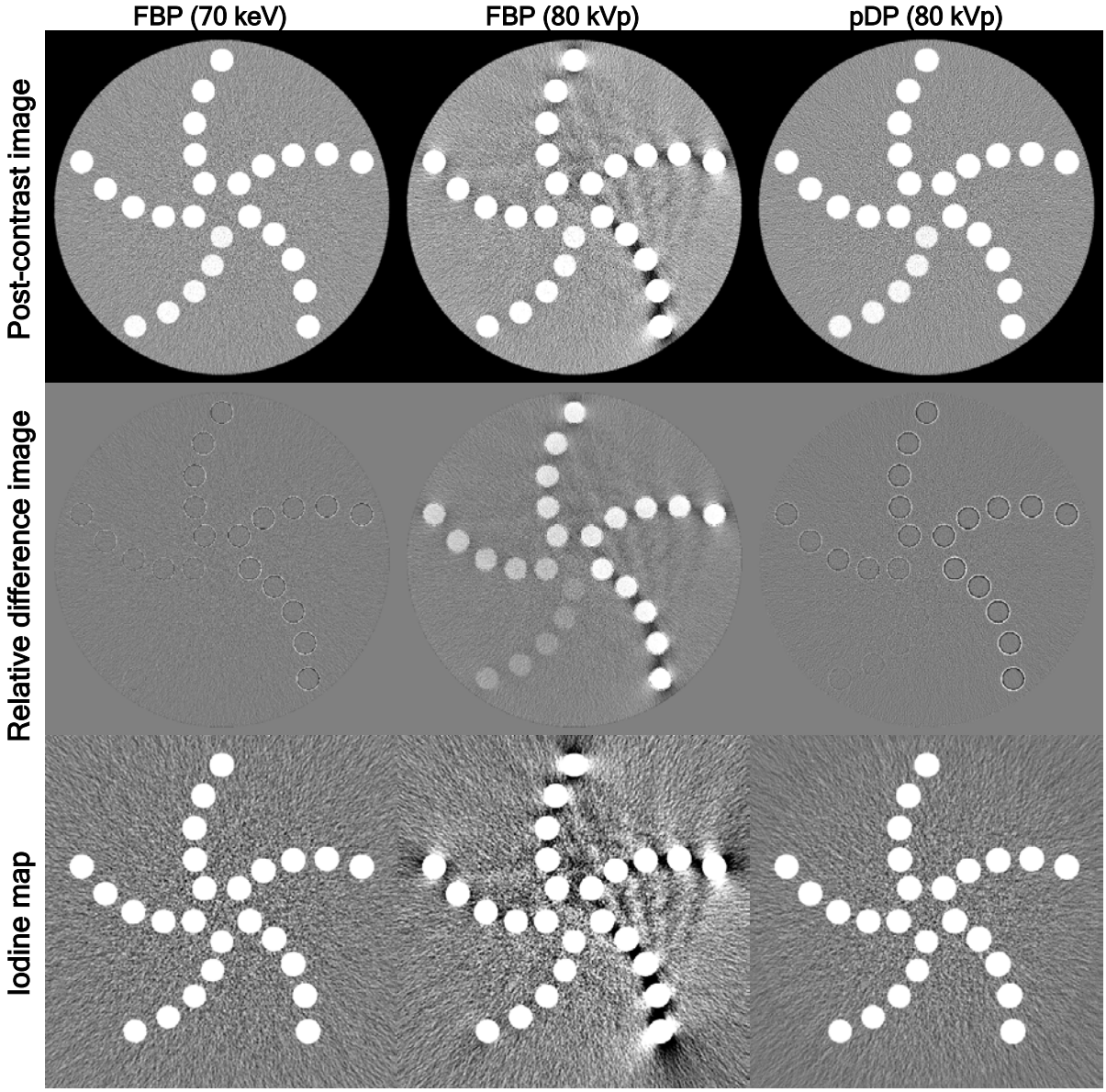

Figure 6-6. Reconstruction results of the dynamic iodine calibration phantom. The images from the first column to the third column were reconstructed by FBP (70 keV), FBP (80 kVp), and pDP (80 kVp), respectively. The images from the first row to the third row were post-contrast images (50/100), relative difference images (0%/20%), and iodine maps (0/40), respectively.

Figure 6-7 shows the location test results of the dynamic iodine calibration phantom (30 cm and 80 kVp). To facilitate comparison, the CT numbers of the iodine inserts in the same concentration group were subtracted from the value of the innermost iodine insert to yield the relative CT numbers, which were then plotted against the radial distance. For FBP (Figure 6-7a), the maximum intragroup difference of the iodine inserts was more than 50 HU. With regard to algorithm pDP (Figure 6-7b), the maximum intragroup difference was reduced below 3 HU, which indicated that the cupping effect was eventually eliminated.

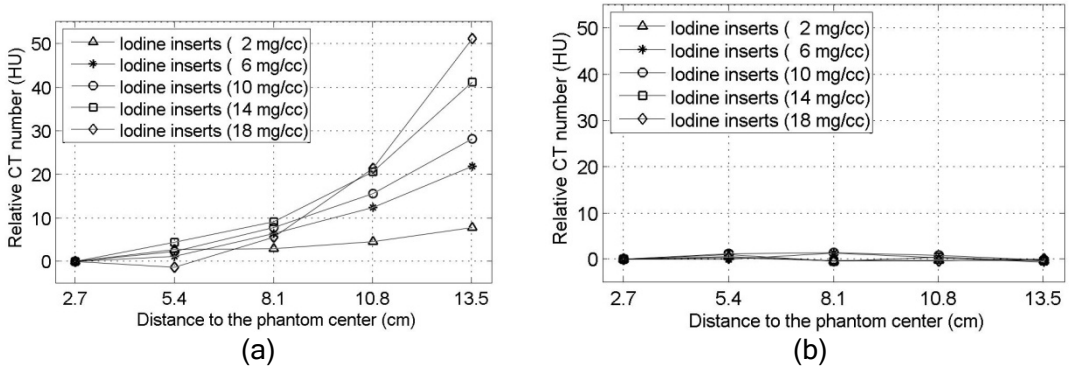

Figure 6-7: Location test results of the dynamic iodine calibration phantom (30 cm and 80 kVp). For the iodine inserts within the same group, their relative CT numbers with respect to the iodine insert nearest to the phantom center were plotted against the radial distance for algorithms (a) FBP and (b) pDP.

In the phantom size test, by varying the phantom size (16, 23, 30, 37 cm) under the same spectrum (80 kVp), a series of projection datasets were simulated and then reconstructed by FBP and pDP. For each reconstructed images, the CT numbers of the iodine inserts in the same group were averaged and plotted against their corresponding theoretical iodine concentrations (Figure 6-8). Ideally, the theoretical iodine concentration curve should be y=26.46x+58.33, where x (mg/ml) represents the iodine concentration, 26.46 (HU·ml/mg) is

the iodine concentration factor, 58.33 (HU) is the CT number of unenhanced soft tissue, and y (HU) represents the CT number. The theoretical curve was plotted in solid line as a reference. The FBP results were plotted in dashed line. Due to the BH effect, all the iodine concentration curves tended to be over-estimated and the slopes of those curves increased with decreased phantom size. In comparison, the curves derived from the pDP algorithm (dotted line in Figure 6-8) perfectly overlapped with the theoretical curve. Linear regression method was performed to compute the iodine concentration curves with a correlation coefficient of greater than 0.999 (Table 6-2). The high agreement of our proposed algorithm indicated our algorithm was independent of the patient size.

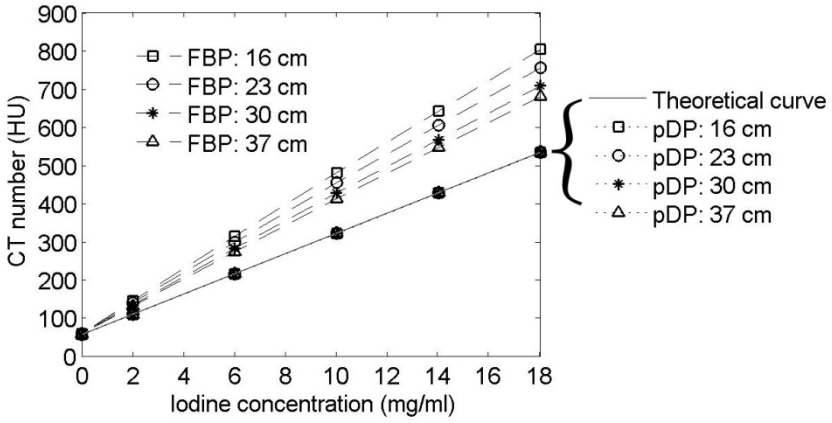

Figure 6-8: Attenuation-concentration curves derived from the phantom size test. By varying the phantom size (square: 16 cm; circle: 23 cm; star: 30 cm; triangle: 37 cm), iodine concentration curves were plotted for different reconstruction algorithms (solid line: FBP; dotted line: pDP). All simulations in this test used the 80 kVp spectrum.

Table 6-2: Linear regression results of the attenuation-concentration curves derived from the phantom size test and spectrum test. The parameters x (mg/ml) and y(HU) represent the iodine concentration and the CT number, respectively.

Simulation tests	Spectrum / Phantom size	FBP	pDP
Phantom size test	80 kVp / 16 cm	y=41.23x+64.43	y=26.41x+58.06
	80 kVp / 23 cm	y=38.59x+64.48	y=26.47x+58.08
	80 kVp / 30 cm	y=35.99x+63.69	y=26.51x+57.61
	80 kVp / 37 cm	y=34.45x+63.98	y=26.54x+57.31
Spectrum test	80 kVp / 30 cm	y=35.99x+63.69	y=26.51x+57.61
	100 kVp / 30 cm	y=27.12x+62.09	y=26.50x+58.15
	120 kVp / 30 cm	y=21.97x+61.28	y=26.51x+58.40
	140 kVp / 30 cm	y=18.45x+60.87	y=26.50x+58.67

By varying the x-ray spectrum (80, 100, 120, 140 kVp), iodine concentration curves for algorithms FBP and pDP were computed and plotted in Figure 6-9. For FBP, only the curve derived from the 100 kVp spectrum was close to the theoretical trend and that was only for the phantom at 30 cm diameter. In comparison, the curves derived from pDP accorded with the theoretical curves very well across x-ray spectrum. The accuracy of the agreements can be further quantitatively reflected by the linear regression results in Table 6-2.

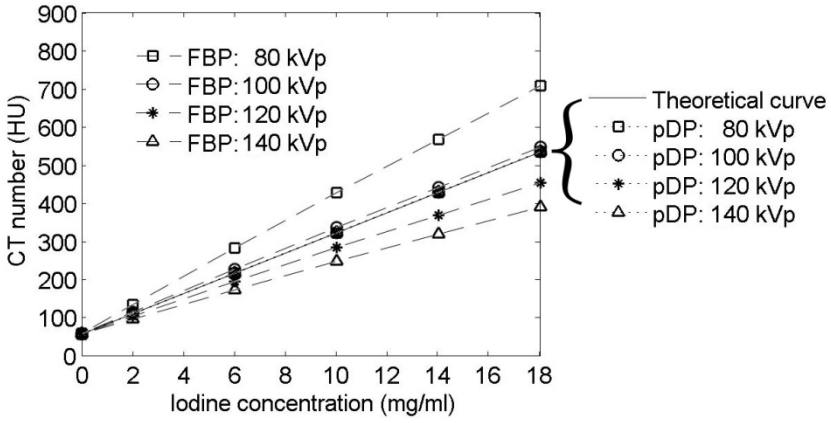

Figure 6-9: Iodine concentration curves derived from the spectrum test. By varying the x-ray spectrum (square: 80 kVp; circle: 100 kVp; star: 120 kVp; triangle: 140 kVp), iodine concentration curves are plotted for different reconstruction algorithms (solid line: FBP; dotted line: pDP). All simulations in this test used the 30 cm diameter phantom.

6.3.2 Dynamic Anthropomorphic Thorax Phantom

The reconstruction results of the dynamic anthropomorphic thorax phantom are shown in Figure 6-10. The images reconstructed by FBP with mono-energetic spectrum (70 keV) are presented in the first column as benchmark results. The images reconstructed by FBP and pDP from the same poly-energetic projection dataset (80 kVp) are presented in the second and third columns, respectively. The reconstructed images and relative difference images of the pre-contrast phase are shown in the first two rows; the reconstructed images and relative difference images of the post-contrast phase with the peak iodine concentration are shown in the third and fourth rows. The iodine maps are shown in the last row.

In the first column of Figure 6-10, due to a mono-energetic spectrum, the images reconstructed by FBP (70 keV) were free of BH artifacts in the pre- and post-contrast images. The second column depicts the reconstruction results of FBP (80 kVp), where BH artifacts

severely deteriorated the image quality. For instance, the metal implant in the pre-contrast image resulted in strong streaks in the heart region and obscured the heart detail. Bones around thoracic cage resulted in visible artifacts to the neighboring soft tissue. In the post-contrast images, other than the mentioned artifacts, the iodinate inserts lowered the attenuations of the breast tissue and the high concentrations of contrast in the left chamber blood pool and descending aorta severely impacted the attenuation density in myocardium. The relative images of the pre- and post-contrast images visually show the error distributions. Fat and breast tissues tended to be under-estimated, but bones and iodinated regions tended to be over-estimated. The iodine map in the last row was contaminated by the bright and dark streaks and the shape of some iodine inserts were not correctly reconstructed.

The images in the last row were reconstructed by pDP (80 kVp). In comparison with FBP (80 kVp), the artifacts induced by the bones, the metal implant, and the iodinated contrast agent were completed eliminated in both pre- and post-contrast images. The image appearance was almost the same with that reconstructed by FBP (70 keV). The relative difference images yielded uniformly negligible values. The iodine map in the last row correctly reflected the iodine distribution. The values of the voxels originally containing bones were slightly less than zero probably caused by noise.

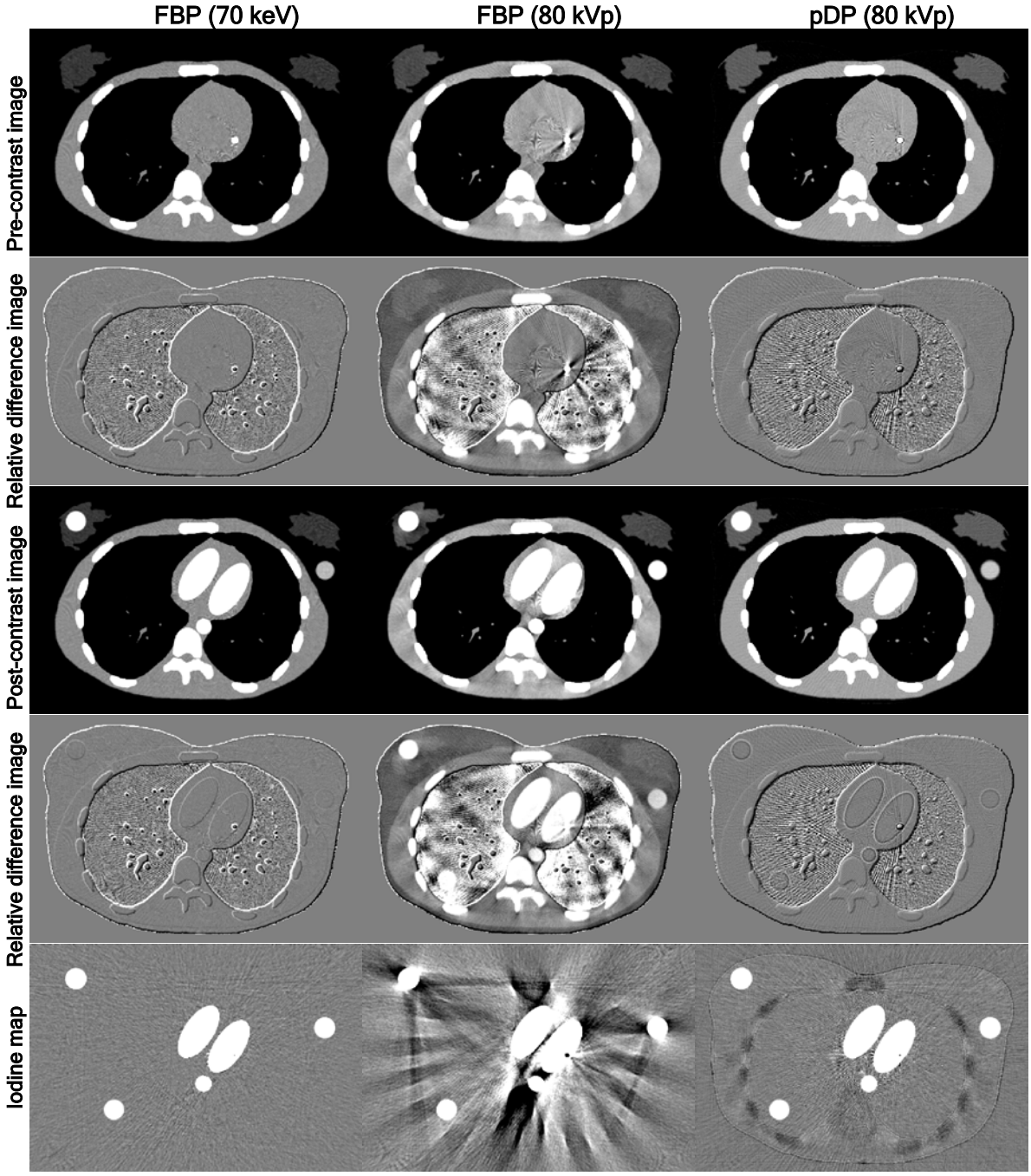

Figure 6-10: Reconstruction results of the dynamic anthropomorphic thorax phantom.

Figure 6-11 depicts the CT number error profiles of the iodine TACs/TCCs in different iodinated regions, i.e., lung, fat, breast, and heart. For FBP (Figure 6-11a), as the average diameter of the dynamic anthropomorphic thorax phantom was approximately 30 cm, iodine concentration curve y=35.99x+63.69 (Table 6-2) was applied to reduce the errors of the CT numbers and the iodine concentrations. However, only the error profile of the iodinated heart was close to zero values, which benefited from the same background tissue with the iodine calibration phantom. Because the shape and the structure of the thorax phantom were different from those of the iodine calibration phantom, discrepancies were still observable. Among all the body tissues, as the attenuation property of the lung tissue deviated most from that of soft tissue, the error profile of lung yielded highest deviations. The error profile of breast tissue also had a similar error magnitude with that of lung, which was caused by the cupping effect (Figure 6-11a). If iodine concentration curves were not applied, those curves would have had even larger errors. For FBP, the maximum error was more than 40 HU, i.e., 1.1 mg/cc in iodine concentration. Improvement in the error profiles was evident by using pDP algorithm, and all error profiles were close to zero values.

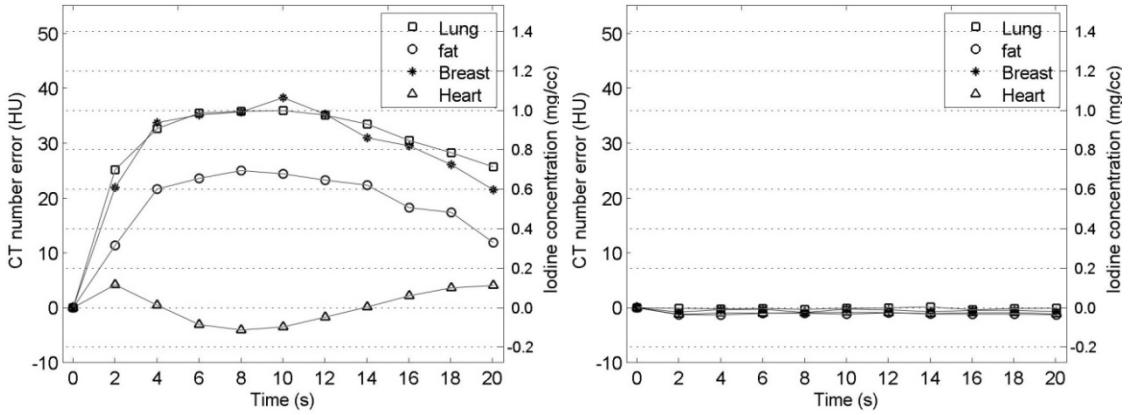

Figure 6-11: CT number error profiles of the TACs/TCCs for the iodine inserts in lung (square), fat (circle), breast (star), and heart (triangle) as defined in the dynamic anthropomorphic thorax phantom (Figure 6-3(b)) for (a) FBP and (b) pDP.

Figure 6-12 depicts the CT number error profiles of the four ROIs as defined in the dynamic anthropomorphic phantom. For FBP (Figure 6-12a), large deviations caused by BH effect could be observed in the basal wall of the left heart chamber and the maximum deviation was as large as -42 HU. The lateral wall also had relative large deviation, which was probably due to the metal artifacts. The BH enhancement of the other two ROIs was relatively small. By contrast, the BH across all ROIs disappeared with the case of pDP (Figure 6-12b).

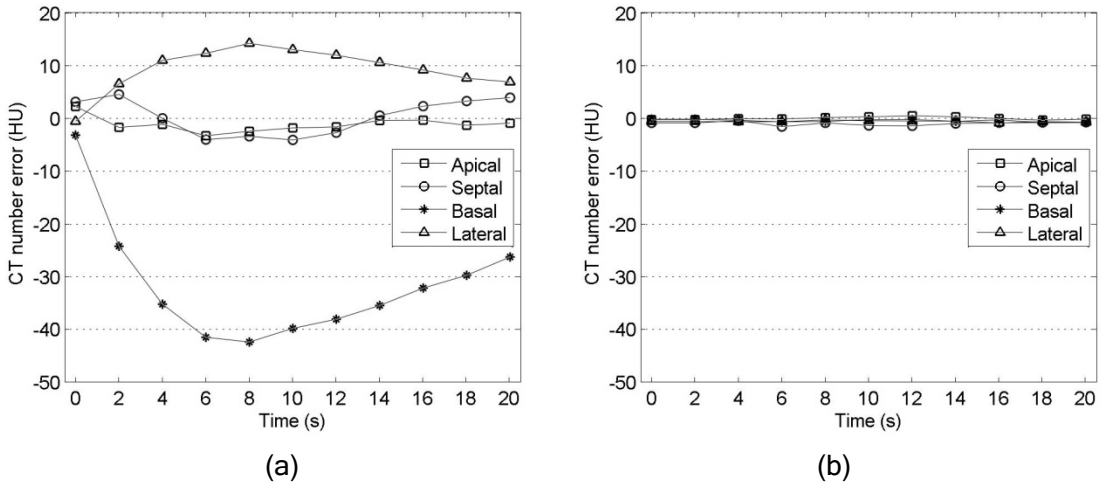

Figure 6-12: CT number error profiles due to BH enhancement in the four ROIs as defined in Figure 6-5. in the dynamic anthropomorphic thorax phantom for algorithms (a) FBP and (b) pDP.

6.4 Discussion

We developed a novel segmentation-free poly-energetic dynamic perfusion imaging algorithm (pDP). There are four important features that distinguish our algorithms from the others [29, 33]. First, pDP can model the attenuation properties of diverse base materials (e.g., lung, fat, breast, soft tissue, bone, implant metal, and iodine) within the reconstruction process. Thus we can effectively eliminate the beam hardening artifacts, greatly reduce metal artifacts, and also significantly improve the accuracy of the reconstruction results. Second, for each post-contrast phase, the iodine projections can be obtained by linearization and be used directly to reconstruct artifact-free iodine maps. As the reconstructed iodine maps can realistically reflect the iodine concentrations, it is not necessary to pre-compute the iodine concentration curves for different spectra and different size phantoms. Third, not limited to

blood-iodine mixtures, the proposed perfusion algorithm can be applied to lung, fat, and breast perfusion exams. Finally, as no segmentation is required in our method, misinterpretations of the voxel types due to the threshold-based segmentation method can be avoided.

In this work, two phantoms were used to validate the proposed algorithm, i.e., a dynamic iodine calibration phantom and a dynamic anthropomorphic thorax phantom. The dynamic iodine calibration phantom was used to investigate the reconstruction stabilities of the iodinated contrast agent in terms of various influential factors (i.e., iodine location, phantom size, and x-ray spectrum). The simulation results showed that, for the widely used FBP-based perfusion algorithm, the errors of the iodine concentration factor (HU·ml/mg) were in a large range (i.e., [-8.01, 14.77]), which indicated that the iodine concentration curve highly depended on these influential factors, making it necessary to apply the pre-calibrated iodine concentration curve to reduce the errors. In contrast, the proposed method accurately modeled the attenuation properties of iodine, so that the error range was reduced to [-0.05, 0.08], effectively eliminating the BH effect.

A realistic dynamic anthropomorphic thorax phantom was utilized to further investigate the reconstruction performance of the proposed algorithm. The simulation results showed that, for FBP, the reconstructed images suffered from severe BH artifacts caused by bone, iodine, and metal implant. The strong artifacts seriously affected the accuracy of the CT numbers. For example, the deviation of the time-attenuation curves of the

soft tissue around the left heart chamber was as large as -40 HU. Though iodine concentration curve was applied to the iodine inserts, the errors of the voxel values was still larger than 40 HU, which was equivalent to a 1.1 mg/ml deviation in iodine concentration. There are two major reasons for this large discrepancy. First, the strong cupping artifacts could significantly affect the iodinated tissues near the periphery the patient body. Second, as the iodine concentration curves were mainly derived from iodinated blood or soft tissue, the errors could be introduced when applying those curves to other iodinated tissues. For pDP, the BH artifacts due to bone and iodine were completely eliminated and the metal artifacts were also greatly reduced. The quantitative results showed that the time-attenuation curves of both soft tissue ROIs and different iodinated tissues could be accurately derived.

One limitation of the proposed algorithm is that it requires that the scanned organs are relatively stationary or the possible motions can be corrected by the registration algorithms. In general, the motion is either voluntary respiratory motion or involuntary cardiac motion. The respiratory motion can be minimized by breath holding, respiratory-gating technique [136, 137], or respiratory correlated reconstruction technique [138]. The impact of the cardiac motion can be reduced by the ECG-gating technique [139-141], which ensures that the acquisition and reconstruction window is selected at the same interval of the ECG. For the cerebral perfusion, as head can be immobilized by forehead and chin straps, the patient motions are generally negligible.

Two smoothing kernels were used in this work. In this study, it was not necessary to optimize these filters, as the purpose of this work was to eliminate beam hardening effect and not to improve the noise properties of the images as affected by the choice of the smoothing kernels. In the future, we intend to utilize adaptive smoothing kernels to reduce image noise while keeping sharp edges or anatomical structures intact. Furthermore, we plan to statistically model the Poisson distribution of the quantum noise [50, 92, 131] into the reconstruction algorithm to further suppress image noise.

6.5 Conclusions

We have presented a poly-energetic dynamic perfusion imaging algorithm (pDP). Simulation results show that the proposed algorithm can effectively eliminate BH artifacts and accurately reconstruct the iodine map regardless of the phantom size, spectrum, location, and background tissue type. Future work will include noise reduction potentials of the proposed algorithm.

Chapter 7

Conclusions and Future Directions

7.1 Summary of the Major Findings

X-ray computed tomography (CT) is an important imaging modality in medical applications, and will continue to be in the future. Its usage has dramatically increased over the last two decades. As CT scans become more ubiquitous, it becomes more important that the CT quality can be standardized and robust. For example, to enable robust quantitative imaging, the ever present beam hardening artifacts (BHAs) should be better mitigated with advanced reconstruction algorithms. Therefore, the main goal of this thesis work was to offer new reconstruction algorithms based on fundamental x-ray physics to enhance quantitative CT images.

A key requirement to minimize BHAs is full knowledge of x-ray spectrum. In Chapter 3, an accurate estimation technique of x-ray spectrum for clinical CT systems was developed. Compared with previous transmission measurement techniques, the proposed method can reconstruct incident spectra across a wide range of angular trajectories by using a single cylindrical phantom and a single axial scan. The average absolute mean energy differences (MEDs) and the normalized root mean square differences (NRMSDs) from the actual spectra across kVp settings and angular trajectories were less than 0.61 keV and 3.41%,

respectively, which indicated the high assessment accuracy and stability of the proposed technique.

With an accurate estimation of the x-ray spectra, a fast poly-energetic iterative FBP (piFBP) algorithm was proposed in Chapter 4 by incorporating the physical properties of the x-ray beams, the materials in the human body, and the detectors. Compared with FBP, for an anthropomorphic phantom (25 cm in diameter) using a 80 kVp spectrum, the algorithm yielded a reduction in the maximum value of the beam-hardening indices (BIdx's) of body tissues from 15.9 to 0.3. The corresponding value for an implant metal (i.e., Titanium) was 23.3 to 1.3. We believe the fast reconstruction speed and excellent performance of the proposed algorithm make it suitable for clinical applications on the current single spectrum CT scanners.

Chapter 4 dealt with non-iodinated examinations. However, a large majority of CT examinations are done with iodine. Among those, in myocardial CT perfusion, iodinated contrast agent is administered to the patient through intravenous injection to increase the absorption of x-rays and to enhance the visibility of cardiovascular structures. Iodine is a high-attenuation material and can result in substantial BHAs. As Iodine has a prominent K-edge within the x-ray energy spectrum and possesses different attenuation properties for body tissues, a poly-energetic SART (pSART) reconstruction algorithm was proposed in Chapter 5 to account for the special attenuation properties of the blood-iodine mixtures of various concentrations. The simulation results from an anthropomorphic phantom (23 cm in

diameter) with an 80 kVp spectrum showed that the maximum error of concentrations of the iodinated inserts was significantly reduced from 7.50 mg/ml for SART to 0.03 mg/ml for pSART.

In Chapter 6, another perfusion algorithm (i.e., segmentation-free poly-energetic dynamic perfusion imaging algorithm [pDP]) was proposed, which can account for the attenuation properties of the mixtures of iodine and various body tissues. Therefore, pDP could be applied to all perfusion exams, such as myocardial perfusion exam, lung perfusion exam, breast perfusion exam, and head perfusion exam, etc. The maximum error of iodine concentrations were reduced from 1.10 mg/ml (FBP) to 0.05 mg/ml (pDP). One limitation of pDP was that the scanned patient must be motionless or the motions can be corrected, as the pre-contrast measurements were used as *a priori* information.

7.2 Future Work

The proposed spectral estimation technique can estimate the post-bowtie x-ray spectra across angular trajectories of the imaging field of view. However, due to the various sources of noise, small variations are observable for different kVp settings (Figure 3-14). In order to reduce variations and to obtain more accurate spectra, the following two approaches can be applied based on the available information about the bowtie filters.

1) If the knowledge of the bowtie filters (such as the attenuation properties and the geometry information) is known, that knowledge can be incorporated into the system matrix (Eq. 3-3) to reconstruct the unique pre-bowtie spectrum.

2) Otherwise, the smoothness and continuity properties of the bowtie filter can be used as a regularization term in Eq. 3-6 to reduce the spectrum variation.

As regards to the poly-energetic reconstruction, the following can be of value for future studies.

1) The proposed algorithms were only implemented and validated in axial mode. It is necessary to extend those algorithms to helical mode to cover both CT acquisition geometries.
2) It is feasible to track the transformation of the spectra across all angular trajectories based on the proposed poly-energetic ray-tracing method. This spectrum information can be further incorporated with additional physics components mentioned in Chapter 1 (e.g., scattering) to improve the spatial resolution, to reduce Compton scatter effect, and to suppress noise.
3) Based on the proposed algorithms, consistent and simplified image quality assessment techniques can be developed, so that the image quality parameters, such as material contrast and modulation transfer function (MTF) would not be affected by the currently influential factors, such as patient size and x-ray spectrum.
4) With the new image quality assessment techniques, new image quality optimization techniques can be established to reduce radiation dose while maintaining the image quality for diagnosis.

Appendix A Quantum Noise Analysis of A Clinical CT Scanner

This appendix aims to validate the statistical properties of the quantum noise and to determine the post-bowtie photon numbers across the detector angle of a clinical CT scanner (Siemens Somatom Definition Flash, Siemens Healthcare, Germany).

A.1 Statistical Model

Previous investigations [2] have revealed that there are two principal noise sources, i.e., x-ray quantum noise and system electronic noise. The former is caused by the fluctuation of photon number and follows Poisson distribution. The latter is due to the electronic fluctuations within the electronic components, such as the detector photodiode, and follows normal distribution. At large mAs settings, electronic noise is usually negligible. In this study, as the current intensities were larger than 17 mAs, we assumed negligible electronic noise and a monochromatic x-ray spectrum. The method described in paper [87] was adopted for the following quantum noise analysis.

The quantum noise in the transmission data can be expressed as

$$N_i = Poisson(\lambda_i), \tag{A-1}$$

where λ is the average number of incident x-ray photons and the sub-index indicates the *i-th* detector element. The mean measurement of the line integral ($\bar{p}_i$) can be expressed in logarithmic format as

$$\overline{p}_i = \ln\left(\frac{N_{0i}}{N_i}\right), \qquad \text{A-2}$$

where index N_{oi} indicates the averaged post-bowtie photon number to the *i-th* detector element without being attenuated by patient body. By using the Taylor expansion, it was shown by Macovski [142] that the relationship between the mean ($\overline{p}_i$) and variance (σ_{p_i}) of the line integral can be expressed with the following simple formula:

$$\sigma_{p_i}^2 = \frac{\exp(\overline{p}_i)}{N_{0i}}. \qquad \text{A-3}$$

The above equation indicates that, for a given mAs, by measuring the statistical properties of the quantum noise of the line integrals, we can determine the post-bowtie photon numbers across all angular trajectories.

A.2 Phantom Experiment

A phantom experiment was performed using an anthropomorphic phantom (Figure A-1, Kyoto Chest Phantom, Kyoto Kagaku Co., Ltd, Japan) on a clinical CT scanner (Siemens Somatom Definition Flash, Siemens Healthcare, Germany). The data acquisition protocols included a tube voltage of 120 kVp and a rotation speed of 0.5 s per rotation. Four different mAs values were used, i.e., 17, 40, 60, 80 mAs. For each mAs value, the CT scanner rotated 100 times in axial mode. Each rotation was composed of 1152 projection views evenly spaced on a circular orbit. Each projection view contained 736 data elements corresponding to the 736 detector elements. The detector bin spacing was 1.286 mm. The detector arrays were on

an arc concentric to the x-ray source with a distance of 1085.6 mm. The distance from the x-ray source to the rotation center was 595.0 mm.

With the measurement results, we computed the statistical properties of the quantum noise and determined the experimental curves of the post-bowtie photons across the detector angle with Eq. A-3. Based on the pre-bowtie spectrum (120 kVp) and the bowtie filters provided by the manufacture (Siemens Healthcare, Germany), the reference curves of the post-bowtie photon numbers were derived. For each mAs setting, the reference curve was further scaled by a multiplying factor, so that the mean photon number of the scaled curve equaled the mean number of the corresponding estimated post-bowtie photons. The averaged normalized root mean square differences (NRMSDs) across detectors were computed to quantitatively evaluate the accuracy of the experimental results.

Figure A-1: A photo of the anthropomorphic Kyoto phantom.

A.3 Results

Based on the quantum noise analysis, the post-bowtie photon numbers across detectors (i.e., angles) at different mAs settings are plotted in Figure A-2. The experimental curves derived from the measured noise (red curves) had a good agreement with the reference curves (black curves). The averaged NRMSDs spread within a small range of [3.5%, 4.8%]. The small deviations could be caused by various factors, such as poly-energetic spectrum, the variation of the detector modules, the mismatch of the rotational angle between repeated scans, or the electronic noise.

With the experimental results, the linear relationship between the maximum post-bowtie photon numbers and mAs values was further computed by linear regression as

$$N_{\max} = 1209 \times mAs . \qquad \text{A-4}$$

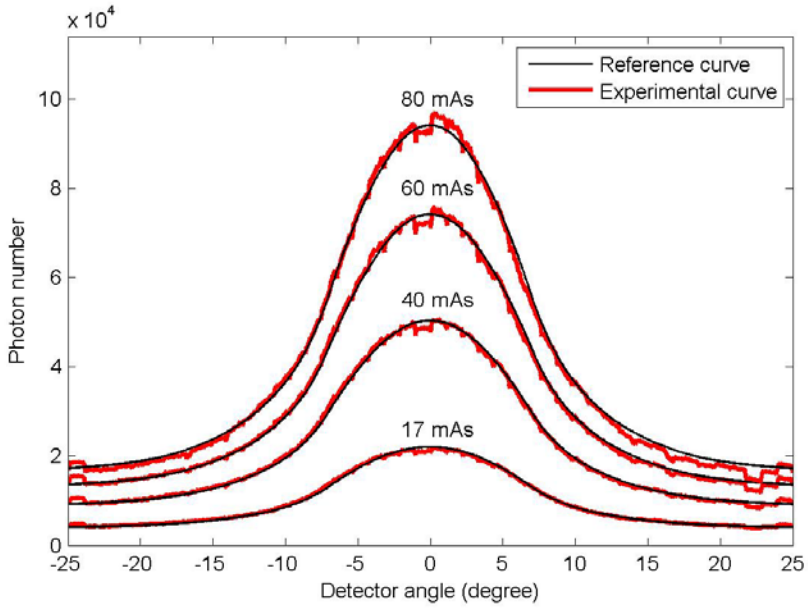

Figure A-2: An illustration of the post-bowtie photon numbers (N_i) across detectors from 100 repeated measurements at four different mAs settings. The experimental (based on noise measurements, Eq. A-3) and reference curves are plotted in red and black colors, respectively.

Table A-1: The averaged normalized root mean square differences (NRMSDs) at the four different mAs levels.

mAs	17 mAs	40 mAs	60 mAs	80 mAs
Averaged NRMSD	3.9%	3.5%	3.6%	4.8%

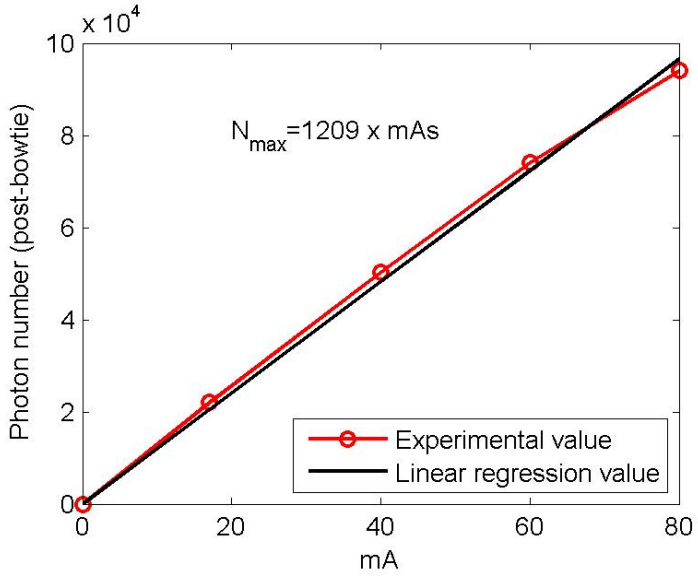

Figure A-3: The linear regression results of the maximum post-bowtie photon number at the four different mAs levels.

A.4 Discussion and Conclusions

We validated the mean-variance relationship of formula Eq. A-3 across detectors at different mAs settings. The averaged NRMSDs with respect to the reference post-bowtie photon numbers derived from the measured noise values were less than 4.8%. This result is accurate enough for the simulation purpose. If the poly-energetic spectrum and the statistical properties of electron noise are accounted for [143], the NRMSDs can be further reduced.

Appendix B Impact of the Detector Systematic Error

The purpose of this appendix is to report a supplemental study on the impact of the detector systematic error to the reconstruction algorithms (i.e., FBP and piFBP).

B.1 Detector Systematic Error

The systematic error (r_i) of the *i-th* detector channel can be defined as a scaling error, i.e.,

$$\tilde{Y}_i = (1 + r_i) Y_i , \qquad \text{B-1}$$

where Y_i is the expected photon number and $\tilde{Y}_i$ is the actual measured photon number contaminated with the systematic error r_i. Several sources can contribute to this systematic error, such as detector offset (induced by dark currents), detector gain, or radiation damage [1]. Air scans are often performed to measure the systematic errors for calibration. If not corrected, such errors, present in all projections, may result in artifacts.

B.2 Simulations

An virtual oval phantom (Figure 4-2) consisting of lung, fat, breast, soft tissue, and bone (1200 mg/cc) was used for our simulation. Generally, the detector systematic errors often follow a Gaussian distribution (mean=0) with the magnitude of the standard deviation across different detector channels less than 1.0% [1]. Based on this upper boundary, three

poly-energetic projection datasets were simulated with the standard deviation magnitudes of the systematic errors of 0.0%, 0.5% and 1.0%, respectively. The beam hardening index (BIdx) and noise index (NIdx) defined in Chapter 4 (Eq. 4-22 and Eq. 4-23) were used to quantify the image quality of the reconstructed images.

All the simulations used the same 80 kVp spectrum and the projections were reconstructed by both FBP and piFBP. The CT geometry was the same as that of the clinical CT scanner (Siemens Somatom Definition Flash, Siemens Healthcare, Germany) described in Table C-1 (Appendix C).

B.3 Results

The reconstruction results are shown in Figure B-1. Compared with FBP, piFBP eliminated the beam hardening artifacts. This improvement is quantitatively reflected in Table B-1. The BIdx range was reduced from [-1.8, 10.4] for FBP to [-0.2, 0.1] for piFBP. With the increase of the systematic error, ring artifacts gradually appeared in the images reconstructed by FBP and piFBP. The quantitative results in Table B-1 indicated that the BIdx's of FBP and piFBP were almost unaffected by the systematic errors. For each algorithm, the largest discrepancy of BIdx's for different levels of systematic errors was less than 0.2. That is because BIdx mainly characterizes the deviation of the mean voxel values, and the influence of the ring artifacts was masked by the average calculation. In contrast, the maximum value of NIdx's increased from 1.4 for no systematic error (0.0%) to 4.7 for the

systematic error of 1.0%. This strong correlation was due to the fact that the NIdx quantifies the variation of the voxel values.

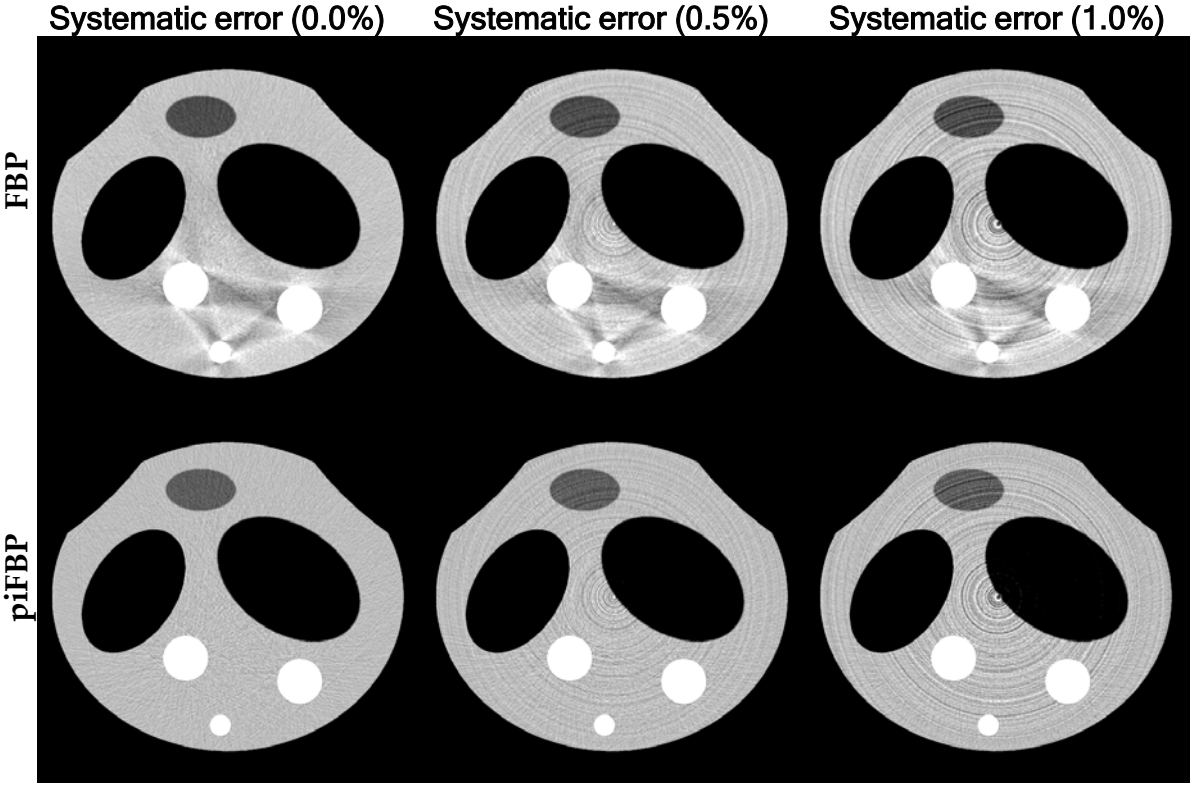

Figure B-1: Reconstructed images (window level = 25 HU; window width = 150 HU) with systematic error of different levels, i.e., (a) 0.0%, (b) 0.5%, (c) 1.0%.

Table B-1: Quantitative results (BIdx/NIdx) of the oval phantom for different systematic error levels, materials, and reconstruction algorithms.

Algorithm	Systematic error	Lung	Fat	Breast	Soft tissue	Bone
FBP	0.0%	-1.6/1.4	-1.8/0.4	-1.0/0.3	0.1/0.6	10.4/0.4
	0.5%	1.4/3.1	-1.7/0.7	-1.0/0.5	-0.1/0.9	10.4/0.4
	1.0%	1.6/3.6	-1.7/1.1	-1.0/1.3	-0.0/1.3	10.4/0.5
piFBP	0.0%	0.0/1.7	-0.1/0.5	-0.1/0.4	0.0/0.5	0.1/ 0.3
	0.5%	-0.2/3.1	-0.1/0.7	-0.1/0.6	-0.1/0.9	0.1/ 0.4
	1.0%	0.1/4.7	-0.2/1.0	-0.1/1.0	-0.2/1.3	0.1/ 0.5

B.4 Discussion and Conclusions

The simulations in this appendix validated the robustness of the proposed algorithm, piFBP, in terms of beam hardening artifacts against systematic errors. For two different magnitudes of systematic errors, the variation of BIdx's was less than 0.2. Even though beam hardening artifacts were eliminated, the ring artifacts were introduced and the NIdx's had a strong positive correlation with the magnitude of the systematic errors.

Appendix C GPU-based Simulation Platform

Based on manufacturer-provided information of the Somatom Definition Flash (SDF) scanner (Siemens Healthcare, Germany), this work involves the development of a GPU-based simulation platform, which is composed of two major components, i.e., a projection simulation component and a reconstruction component.

This simulation platform facilitated validating our poly-energetic reconstruction algorithms in four ways.

1) It enabled us to completely control the x-ray spectrum, such that mono-energetic projections could be simulated, with which images could be reconstructed and used as a benchmark (e.g., the oval phantom simulation in the validation section of Chapter 4).
2) Physical parameters (such as scatter radiation and focal spot size) could be eliminated, such that we could only focus on the beam hardening effect due to the poly-energetic spectrum.
3) The dynamic process of the iodinated contrast agent in various body tissues in CT perfusion exams could be accurately controlled and modeled for quantitative analysis (e.g., Chapter 6), which is difficult through a physical experiment.
4) As our simulation platform is driven by GPU, dozens of simulation tasks (e.g., about 50 simulations were performed in Chapter 4) could be automatically and sequentially

simulated in batch processing mode, which enabled us to investigate the influence of diverse influential factors (such as phantom size, spectral type, mismatch spectra, and anatomic region, etc.) to the reconstruction stability of the proposed algorithms.

C.1 Projection Simulation Component

Given a voxelized phantom (e.g., Figure 4-2), the projection simulation component can compute accurate poly-energetic projections based on Eq. 2-6. The following items detail the important features of our projection simulation component.

1) The CT geometry of the SDF scanner was modeled;
2) The pre-bowtie poly-energetic spectra provided by the manufacturer were incorporated;
3) The properties of the bowtie filter provided by the manufacturer (such as, material, shape and position) were modeled to account for the angle-dependent change of the post-bowtie spectra;
4) The energy-dependent attenuation properties of the materials of the scanned object were modeled [46];
5) The detector absorption ratio provided by the manufacturer was modeled;
6) Quantum noise corresponding to 4.0×10^5 photons per detector pixel was added to the projection data;
7) Separable footprint method [4, 144] was adopted to reduce the influence of the voxel size and detector size;

8) The projection simulation component was coded in GPU, such that a dataset of 2,304 projections could be generated within 2 seconds.

Typical simulation parameters used are listed in Table C-1. The accuracy of the projection simulation component is reflected in Chapter 3. For example, the simulated transmission measurements showed a good agreement with the experimental transmission measurements in Figure 3-9 and Figure 3-10. If the un-attenuated measurement is 1 (Eq. 3-1), the estimated error with polyethylene was only 0.002, which was determined by computing the standard deviation of the transmission measurements within the 1 mm interval centered at the intersection length of 137 mm (Figure 3-9).

Table C-1: Parameters used in the simulations.

Parameter name	Value
Source-to-detector distance (mm)	1085.6
Source-to-object distance (mm)	595.0
Number of detector bins	736
Detector size at iso-center (mm^2)	0.60 x 0.60
Total photon number per detector bin	4.0×10^5
Number of energy bins	280
Energy bin size	0.5 keV
Pixel size of the phantoms (mm^2)	0.20 x 0.20
Pixel size of the reconstructed images (mm^2)	0.40 x 0.40
Number of projections	2304

C.2 Reconstruction Component

The reconstruction component included five GPU-driven reconstruction algorithms, i.e., Filtered Backprojection algorithm (FBP) [1, 119], simultaneous algebraic reconstruction technique (SART) [119, 121], , poly-energetic iterative FBP (piFBP, Chapter 4), poly-energetic

SART (pSART, Chapter 5), and poly-energetic dynamic perfusion algorithm (pDP, Chapter 6).

To investigate the accuracy of our reconstruction component, we compared the image reconstructed by the SDF scanner (Figure C-1.a) and the image reconstructed by our FBP algorithm (Figure C-1.b) using the same experimental projection dataset. The voxel value differences in terms of CT number were less than 1.5 HU. This small difference might be due to the difference of the filters. Therefore, the FBP algorithm in the reconstruction component could be used as a benchmark algorithm in our simulations.

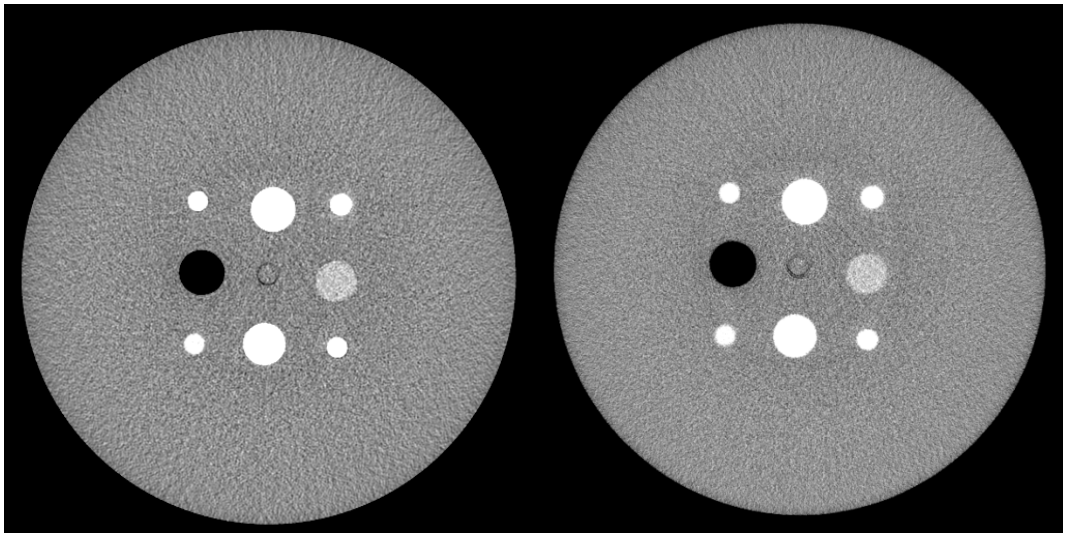

Figure C-1: Comparison of the image reconstructed by (a) SDF scanner and our own FBP algorithm using the same projection dataset acquired with Mercury phantom [85].

References

1. Hsieh, J. *Computed tomography: principles, design, artifacts, and recent advances*. 2009. SPIE Bellingham, WA.

2. Bushberg, J.T. and J.M. Boone, *The essential physics of medical imaging*. 2011: Lippincott Williams & Wilkins.

3. Nuyts, J., et al., *Modelling the physics in the iterative reconstruction for transmission computed tomography.* Physics in medicine and biology, 2013. **58**(12): p. R63.

4. Long, Y., J.A. Fessler, and J.M. Balter, *3D forward and back-projection for X-ray CT using separable footprints.* Medical Imaging, IEEE Transactions on, 2010. **29**(11): p. 1839-1850.

5. Thibault, J.-B., et al., *A three-dimensional statistical approach to improved image quality for multislice helical CT.* Medical physics, 2007. **34**: p. 4526.

6. Man, B.D. and S. Basu, *Distance-driven projection and backprojection in three dimensions.* Physics in Medicine and Biology, 2004. **49**(11): p. 2463-2475.

7. Zeng, K., et al. *Spatial resolution enhancement in CT iterative reconstruction*. in *Nuclear Science Symposium Conference Record (NSS/MIC), 2009 IEEE*. 2009. IEEE.

8. Little, K. and P. La Riviere. *An algorithm for modeling non-linear system effects in iterative CT reconstruction*. in *Nuclear Science Symposium and Medical Imaging Conference (NSS/MIC), 2012 IEEE*. 2012. IEEE.

9. Yu, H. and G. Wang, *Finite detector based projection model for high spatial resolution.* Journal of X-ray science and technology, 2012. **20**(2): p. 229-238.

10. Neitzel, U., *Grids or air gaps for scatter reduction in digital radiography: a model calculation.* Medical physics, 1992. **19**: p. 475.

11. Liu, X., et al., *A Scanning Sampled Measurement (SSM) Technique for Scatter Measurement and Correction in Cone Beam Breast CT.* Medical Physics, 2005. **32**: p. 2093.

12. Niu, T. and L. Zhu, *Scatter correction for full-fan volumetric CT using a stationary beam blocker in a single full scan.* Medical Physics, 2011. **38**: p. 6027.

13. Bertram, M., J. Wiegert, and G. Rose. *Potential of software-based scatter corrections in cone-beam volume CT*. in *Proc. SPIE*. 2005.

14. Seibert, J. and J. Boone, *X-ray scatter removal by deconvolution.* Medical physics, 1988. **15**: p. 567.

15. Mainegra-Hing, E. and I. Kawrakow, *Variance reduction techniques for fast Monte Carlo CBCT scatter correction calculations.* Physics in medicine and biology, 2010. **55**(16): p. 4495.

16. Zbijewski, W. and F.J. Beekman, *Comparison of methods for suppressing edge and aliasing artefacts in iterative x-ray CT reconstruction.* Physics in Medicine and Biology, 2006. **51**(7): p. 1877.

17. Angel, E., et al., *Monte Carlo simulations to assess the effects of tube current modulation on breast dose for multidetector CT.* Physics in medicine and biology, 2009. **54**(3): p. 497.

18. Knoll, G.F., *Radiation detection and measurement*. 2010: Wiley. com.

19. Elbakri, I.A. and J.A. Fessler, *Segmentation-free statistical image reconstruction for polyenergetic X-ray computed tomography with experimental validation.* Physics in Medicine and Biology, 2003. **48**(15): p. 2453.

20. Elbakri, I.A. and J.A. Fessler. *Efficient and accurate likelihood for iterative image reconstruction in X-ray computed tomography*. in *Medical Imaging 2003*. 2003. International Society for Optics and Photonics.

21. McDavid, W.D., et al., *Spectral effects on three-dimensional reconstruction from x rays.* Medical physics, 1975. **2**: p. 321.

22. Brooks, R.A. and G. Di Chiro, *Beam hardening in x-ray reconstructive tomography.* Physics in medicine and biology, 1976. **21**(3): p. 390.

23. McCullough, E.C., et al., *An evaluation of the quantitative and radiation features of a scanning x-ray transverse axial tomograph: the EMI scanner.* Radiology, 1974. **111**(3): p. 709-15.

24. Brooks, R.A. and G. Di Chiro, *Beam hardening in x-ray reconstructive tomography.* Phys Med Biol, 1976. **21**(3): p. 390-8.

25. McDavid, W.D., et al., *Correction for spectral artifacts in cross-sectional reconstruction from x rays.* Medical physics, 1977. **4**(1): p. 54.

26. Herman, G.T., *Correction for beam hardening in computed tomography.* Physics in medicine and biology, 2002. **24**(1): p. 81.

27. Rührnschopf, E.-P. and B. Scholz, *Method for hardening correction in medical imaging*, 2010, Google Patents.

28. Joseph, P.M. and R.D. Spital, *A method for correcting bone induced artifacts in computed tomography scanners.* J Comput Assist Tomogr, 1978. **2**(1): p. 100-8.

29. Joseph, P.M. and C. Ruth, *A method for simultaneous correction of spectrum hardening artifacts in CT images containing both bone and iodine.* Medical Physics, 1997. **24**(10): p. 1629-1634.

30. Hsieh, J., et al., *An iterative approach to the beam hardening correction in cone beam CT.* Med Phys, 2000. **27**(1): p. 23-9.

31. Yan, C.H., et al., *Reconstruction algorithm for polychromatic CT imaging: application to beam hardening correction.* IEEE Trans Med Imaging, 2000. **19**(1): p. 1-11.

32. Elbakri, I.A. and J.A. Fessler, *Statistical image reconstruction for polyenergetic X-ray computed tomography.* Medical Imaging, IEEE Transactions on, 2002. **21**(2): p. 89-99.

33. Stenner, P., et al., *Dynamic iterative beam hardening correction (DIBHC) in myocardial perfusion imaging using contrast-enhanced computed tomography.* Investigative radiology, 2010. **45**(6): p. 314-323.

34. Alvarez, R.E. and A. Macovski, *Energy-Selective Reconstructions in X-Ray Computerized Tomography.* Physics in Medicine and Biology, 1976. **21**(5): p. 733-744.

35. Stonestrom, J.P., R.E. Alvarez, and A. Macovski, *A framework for spectral artifact corrections in x-ray CT.* IEEE Trans Biomed Eng, 1981. **28**(2): p. 128-41.

36. Maaß, C., E. Meyer, and M. Kachelrieß, *Exact dual energy material decomposition from inconsistent rays (MDIR).* Medical Physics, 2011. **38**(2): p. 691.

37. Prince, J.L. and J.M. Links, *Medical imaging signals and systems*. 2006: Pearson Prentice Hall Upper Saddle River, NJ.

38. Flohr, T.G., et al., *Image reconstruction and image quality evaluation for a 64-slice CT scanner with z-flying focal spot.* Medical Physics, 2005. **32**(8): p. 2536.

39. Flohr, T.G., et al., *Novel ultrahigh resolution data acquisition and image reconstruction for multi-detector row CT.* Medical Physics, 2007. **34**(5): p. 1712.

40. Kyriakou, Y., et al., *Impact of the z-flying focal spot on resolution and artifact behavior for a 64-slice spiral CT scanner.* Eur Radiol, 2006. **16**(6): p. 1206-15.

41. Salvat, F., J.M. Fernández-Varea, and J. Sempau. *PENELOPE-2006: A code system for Monte Carlo simulation of electron and photon transport*. in *Workshop Proceedings*. 2006.

42. Hubbell, J., et al., *Atomic form factors, incoherent scattering functions, and photon scattering cross sections.* Journal of physical and chemical reference data, 1975. **4**(3): p. 471-538.

43. Petersilka, M., et al., *Strategies for scatter correction in dual source CT.* Medical physics, 2010. **37**: p. 5971.

44. Fuchs, T., M. Kachelrieß, and W.A. Kalender, *Direct comparison of a xenon and a solid-state CT detector system: measurements under working conditions.* Medical Imaging, IEEE Transactions on, 2000. **19**(9): p. 941-948.

45. Duan, X., et al., *Electronic noise in CT detectors: Impact on image noise and artifacts.* American Journal of Roentgenology, 2013. **201**(4): p. W626-W632.

46. Hubbell, J.H. and S.M. Seltzer, *Tables of X-ray mass attenuation coefficients and mass energy-absorption coefficients 1 keV to 20 MeV for elements Z= 1 to 92 and 48 additional substances of dosimetric interest*, 1995, National Inst. of Standards and Technology-PL, Gaithersburg, MD (United States). Ionizing Radiation Div.

47. Buzug, T., *Image Quality and Artifacts.* Computed Tomography: From Photon Statistics to Modern Cone-Beam CT, 2008: p. 403-469.

48. Blankstein, R., et al., *Cardiac myocardial perfusion imaging using dual source computed tomography.* The International Journal of Cardiovascular Imaging, 2009. **25**(S2): p. 209-216.

49. Goodsitt, M.M., et al., *Quantitative CT of lung nodules: Dependence of calibration on patient body size, anatomic region, and calibration nodule size for single-and dual-energy techniques.* Medical physics, 2009. **36**(7): p. 3107-3121.

50. Cann, C.E., *Quantitative CT for determination of bone mineral density: a review.* Radiology, 1988. **166**(2): p. 509-522.

51. Cann, C.E., *Quantitative CT applications: comparison of current scanners.* Radiology, 1987. **162**(1): p. 257-261.

52. Chen, B., et al., *Quantitative CT: technique dependence of volume estimation on pulmonary nodules.* Physics in medicine and biology, 2012. **57**(5): p. 1335.

53. Adams, J.E., *Quantitative computed tomography.* European journal of radiology, 2009. **71**(3): p. 415-424.

54. Das, M., et al., *Accuracy of automated volumetry of pulmonary nodules across different multislice CT scanners.* European radiology, 2007. **17**(8): p. 1979-1984.

55. Gerber, T.C., B. Kantor, and E.E. Williamson, *Computed tomography of the cardiovascular system*. 2007: Informa Healthcare.

56. Akashi-Tanaka, S., et al., *Whole-breast volume perfusion images using 256-row multislice computed tomography: visualization of lesions with ductal spread.* Breast Cancer, 2009. **16**(1): p. 62-7.

57. Lee, Y.H., et al., *Lung perfusion CT: the differentiation of cavitary mass.* Eur J Radiol, 2010. **73**(1): p. 59-65.

58. Jain, R., *Perfusion CT imaging of brain tumors: an overview.* AJNR Am J Neuroradiol, 2011. **32**(9): p. 1570-7.

59. Lin, Y., et al., *An angle-dependent reconstruction technique of x-ray spectrum from rotational transmission measurement of clinical CT Systems.* Submitted to Medical physics, (2013.

60. Li, X., et al., *Patient-specific radiation dose and cancer risk estimation in CT: Part I. Development and validation of a Monte Carlo program.* Medical physics, 2011. **38**: p. 397.

61. Jarry, G., et al., *A Monte Carlo-based method to estimate radiation dose from spiral CT: from phantom testing to patient-specific models.* Physics in Medicine and Biology, 2003. **48**(16): p. 2645.

62. Sidky, E.Y., et al., *A robust method of x-ray source spectrum estimation from transmission measurements: Demonstrated on computer simulated, scatter-free transmission data.* Journal of Applied Physics, 2005. **97**(12): p. 124701.

63. Storm, E., *Calculated bremsstrahlung spectra from thick tungsten targets.* Physical Review A, 1972. **5**(6): p. 2328.

64. Birch, R. and M. Marshall, *Computation of bremsstrahlung x-ray spectra and comparison with spectra measured with a Ge (Li) detector.* Physics in Medicine and Biology, 1979. **24**(3): p. 505.

65. Boone, J.M. and J.A. Seibert, *An accurate method for computer-generating tungsten anode x-ray spectra from 30 to 140 kV.* Medical physics, 1997. **24**(11): p. 1661-1670.

66. Hendee, W.R. and E.R. Ritenour, *Medical imaging physics*. 2003: John Wiley & Sons.

67. Matscheko, G. and R. Ribberfors, *A Compton scattering spectrometer for determining x-ray photon energy spectra.* Physics in medicine and biology, 1987. **32**(5): p. 577.

68. Yaffe, M., K. Taylor, and H. Johns, *Spectroscopy of diagnostic x rays by a Compton - scatter method.* Medical physics, 1976. **3**(5): p. 328-334.

69. Miyajima, S., *Thin CdTe detector in diagnostic x-ray spectroscopy.* Medical Physics, 2003. **30**(5): p. 771.

70. Maeda, K., M. Matsumoto, and A. Taniguchi, *Compton-scattering measurement of diagnostic x-ray spectrum using high-resolution Schottky CdTe detector.* Medical Physics, 2005. **32**(6): p. 1542.

71. Redus, R.H., et al., *Characterization of CdTe detectors for quantitative X-ray spectroscopy.* Nuclear Science, IEEE Transactions on, 2009. **56**(4): p. 2524-2532.

72. Miyajima, S., K. Imagawa, and M. Matsumoto, *CdZnTe detector in diagnostic x-ray spectroscopy.* Medical Physics, 2002. **29**(7): p. 1421.

73. Seelentag, W. and W. Panzer, *Stripping of X-ray bremsstrahlung spectra up to 300 kVp on a desk type computer.* Physics in medicine and biology, 1979. **24**(4): p. 767.

74. Waggener, R.G., et al., *X-ray spectra estimation using attenuation measurements from 25 kVp to 18 MV.* Medical physics, 1999. **26**(7): p. 1269-1278.

75. Duan, X., et al., *CT scanner x-ray spectrum estimation from transmission measurements.* Medical Physics, 2011. **38**(2): p. 993.

76. Archer, B.R. and L.K. Wagner, *A Laplace transform pair model for spectral reconstruction.* Medical physics, 1982. **9**(844).

77. Whiting, B.R., et al., *Properties of preprocessed sinogram data in x-ray computed tomography.* Medical Physics, 2006. **33**(9): p. 3290.

78. Whiting, B.R. *Signal statistics in x-ray computed tomography*. in *Medical Imaging 2002*. 2002. International Society for Optics and Photonics.

79. Chung, J., J.G. Nagy, and I. Sechopoulos, *Numerical algorithms for polyenergetic digital breast tomosynthesis reconstruction.* SIAM Journal on Imaging Sciences, 2010. **3**(1): p. 133-152.

80. Hebert, T. and R. Leahy, *A generalized EM algorithm for 3-D Bayesian reconstruction from Poisson data using Gibbs priors.* Medical Imaging, IEEE Transactions on, 1989. **8**(2): p. 194-202.

81. Green, P.J., *Bayesian reconstructions from emission tomography data using a modified EM algorithm.* Medical Imaging, IEEE Transactions on, 1990. **9**(1): p. 84-93.

82. Wiegert, J., et al. *Model based scatter correction for cone-beam computed tomography*. in *Medical Imaging*. 2005. International Society for Optics and Photonics.

83. Clackdoyle, R., et al., *Quantitative reconstruction from truncated projections in classical tomography.* Nuclear Science, IEEE Transactions on, 2004. **51**(5): p. 2570-2578.

84. Hsieh, J., et al., *A novel reconstruction algorithm to extend the CT scan field-of-view.* Medical physics, 2004. **31**: p. 2385.

85. Wilson, J.M., et al., *A methodology for image quality evaluation of advanced CT systems.* Medical Physics, 2013. **40**: p. 031908.

86. Badal, A. and A. Badano, *Accelerating Monte Carlo simulations of photon transport in a voxelized geometry using a massively parallel graphics processing unit.* Medical physics, 2009. **36**: p. 4878.

87. Wang, J., et al., *An experimental study on the noise properties of x-ray CT sinogram data in Radon space.* Phys Med Biol, 2008. **53**(12): p. 3327-41.

88. Lin, Y. and E. Samei, *A fast poly-energetic iterative FBP algorithm.* Physics in Medicine and Biology, 2014. **59**(7): p. 1655.

89. Kyriakou, Y., et al., *Empirical beam hardening correction (EBHC) for CT.* Medical physics, 2010. **37**: p. 5179.

90. Sukovle, P. and N.H. Clinthorne. *Basis material decomposition using triple-energy X-ray computed tomography*. in *Instrumentation and Measurement Technology Conference, 1999. IMTC/99. Proceedings of the 16th IEEE*. 1999.

91. Depypere, M., et al. *An iterative dual energy CT reconstruction method for a K-edge contrast material*. in *Proceedings of SPIE*. 2011.

92. Goodsitt, M.M., *Conversion relations for quantitative CT bone mineral densities measured with solid and liquid calibration standards.* Bone and mineral, 1992. **19**(2): p. 145-158.

93. Steenbeek, J., C. van Kuijk, and J. Grashuis, *Influence of calibration materials in single-and dual-energy quantitative CT.* Radiology, 1992. **183**(3): p. 849-855.

94. Cody, D.D., M.J. Flynn, and D.S. Vickers, *A technique for measuring regional bone mineral density in human lumbar vertebral bodies.* Medical physics, 1989. **16**: p. 766.

95. Rao, G.U., et al., *Systematic errors in bone-mineral measurements by quantitative computed tomography.* Medical physics, 1987. **14**: p. 62.

96. Lalush, D.S. and B.M. Tsui, *Improving the convergence of iterative filtered backprojection algorithms.* Medical physics, 1994. **21**: p. 1283.

97. Wallis, J.W. and T.R. Miller, *Rapidly converging iterative reconstruction algorithms in single-photon emission computed tomography.* Journal of nuclear medicine: official publication, Society of Nuclear Medicine, 1993. **34**(10): p. 1793.

98. Pan, X., et al., *Correction for photon attenuation in SPECT: analytical framework, average attenuation factors, and a new hybrid approach.* Physics in medicine and biology, 1993. **38**(9): p. 1219.

99. Chang, L.-T., *Attenuation correction and incomplete projection in single photon emission computed tomography.* Nuclear Science, IEEE Transactions on, 1979. **26**(2): p. 2780-2789.

100. Munshi, P., *Error analysis of tomographic filters. I: Theory.* NDT & E International, 1992. **25**(4): p. 191-194.

101. Munshi, P., et al., *Error analysis of Tomographic filters II: Results.* NDT & E International, 1993. **26**(5): p. 235-240.

102. Yu, Z., et al., *Fast Model-Based X-Ray CT Reconstruction Using Spatially Nonhomogeneous ICD Optimization.* Ieee Transactions on Image Processing, 2011. **20**(1): p. 161-175.

103. Lin, Y., et al., *An angle-dependent estimation of CT x-ray spectrum from rotational transmission measurements.* Submitted to Medical Physics, 2013.

104. Meyer, E., et al., *Frequency split metal artifact reduction (FSMAR) in computed tomography.* Medical physics, 2012. **39**: p. 1904.

105. Vedula, V. and P. Munshi, *An improved algorithm for beam-hardening corrections in experimental X-ray tomography.* NDT & E International, 2008. **41**(1): p. 25-31.

106. Ramakrishna, K., K. Muralidhar, and P. Munshi, *Beam-hardening in simulated X-ray tomography.* NDT & E International, 2006. **39**(6): p. 449-457.

107. Ko, S.M., et al., *Myocardial perfusion imaging using adenosine-induced stress dual-energy computed tomography of the heart: comparison with cardiac magnetic resonance imaging and conventional coronary angiography.* European radiology, 2011. **21**(1): p. 26-35.

108. Rocha-Filho, J.A., et al., *incremental value of adenosine-induced stress myocardial perfusion imaging with dual-source CT at cardiac CT angiography1.* Radiology, 2010. **254**(2): p. 410-419.

109. So, A. and T.Y. Lee, *Quantitative myocardial CT perfusion: a pictorial review and the current state of technology development.* J Cardiovasc Comput Tomogr, 2011. **5**(6): p. 467-81.

110. Valdiviezo, C., et al., *Quantitative and qualitative analysis and interpretation of CT perfusion imaging.* J Nucl Cardiol, 2010. **17**(6): p. 1091-100.

111. Neukirchen, C., M. Giordano, and S. Wiesner, *An iterative method for tomographic x-ray perfusion estimation in a decomposition model-based approach.* Medical Physics, 2010. **37**(12): p. 6125.

112. Wagner, M., et al., *A model based algorithm for perfusion estimation in interventional C-arm CT systems.* Med Phys, 2013. **40**(3): p. 031916.

113. Bastarrika, G., et al., *Adenosine-stress dynamic myocardial CT perfusion imaging: initial clinical experience.* Investigative radiology, 2010. **45**(6): p. 306-313.

114. Camici, P.G. and O.E. Rimoldi, *The clinical value of myocardial blood flow measurement.* Journal of Nuclear Medicine, 2009. **50**(7): p. 1076-1087.

115. Lin, Y. and E. Samei, *An efficient polyenergetic SART (pSART) reconstruction algorithm for quantitative myocardial CT perfusion.* Medical Physics, 2014. **41**(2): p. 021911.

116. Klinder, T., et al., *Automated model-based rib cage segmentation and labeling in CT images*, in *Medical Image Computing and Computer-Assisted Intervention–MICCAI 2007*. 2007, Springer. p. 195-202.

117. Bae, K.T., *Intravenous Contrast Medium Administration and Scan Timing at CT: Considerations and Approaches1.* Radiology, 2010. **256**(1): p. 32-61.

118. Kim, Y. and D. Kim, *A fully automatic vertebra segmentation method using 3D deformable fences.* Computerized Medical Imaging and Graphics, 2009. **33**(5): p. 343-352.

119. Slaney, M. and A. Kak, *Principles of computerized tomographic imaging.* SIAM, Philadelphia, 1988.

120. Fitzpatrick, J.M. and M. Sonka, *Handbook of Medical Imaging, Volume 2: Medical Image Processing and Analysis*. 2000: SPIE Press.

121. Andersen, A. and A. Kak, *Simultaneous algebraic reconstruction technique (SART): a superior implementation of the ART algorithm.* Ultrasonic imaging, 1984. **6**(1): p. 81-94.

122. Lin, Y. and E. Samei, *Development and evaluation of a segmentation-free poly-energetic dynamic algorithm for perfusion CT.* Submitted to Medical physics, 2013.

123. George, R.T., et al., *Quantification of myocardial perfusion using dynamic 64-detector computed tomography.* Investigative radiology, 2007. **42**(12): p. 815-822.

124. Goo, H.W., *Initial experience of dual-energy lung perfusion CT using a dual-source CT system in children.* Pediatr Radiol, 2010. **40**(9): p. 1536-44.

125. Xu, N., et al., *Clinical Study of Tumor Angiogenesis and Perfusion Imaging Using Multi-slice Spiral Computed Tomography for Breast Cancer.* Asian Pacific Journal of Cancer Prevention, 2013. **14**(1): p. 429-433.

126. Hirasawa, H., et al., *Perfusion CT of breast carcinoma: arterial perfusion of nonscirrhous carcinoma was higher than that of scirrhous carcinoma.* Acad Radiol, 2007. **14**(5): p. 547-52.

127. Li, S.P., et al., *Predicting response to neoadjuvant chemotherapy in primary breast cancer using volumetric helical perfusion computed tomography: a preliminary study.* Eur Radiol, 2012. **22**(9): p. 1871-80.

128. Harrison, R., *A note on beam hardening in iodine-subtraction imaging and its implications for quantitative measurements.* Physics in medicine and biology, 1985. **30**(12): p. 1335.

129. Miles, K. and M. Griffiths, *Perfusion CT: a worthwhile enhancement?* British Journal of Radiology, 2003. **76**(904): p. 220-231.

130. Rodriguez-Granillo, G.A., et al., *Signal density of left ventricular myocardial segments and impact of beam hardening artifact: implications for myocardial perfusion assessment by multidetector CT coronary angiography.* Int J Cardiovasc Imaging, 2010. **26**(3): p. 345-54.

131. Hsieh, J., Y. Wei, and G. Wang, *Fractional scan algorithms for low-dose perfusion CT.* Medical Physics, 2004. **31**(5): p. 1254.

132. Miles, K.A., et al., *Quantitative contrast-enhanced computed tomography: is there a need for system calibration?* European radiology, 2007. **17**(4): p. 919-926.

133. Lin, Y. and E. Samei, *A fast poly-energetic iterative FBP algorithm.* Accepted by Physics in Medicine and Biology, 2013.

134. Press, W.H., *Numerical recipes 3rd edition: The art of scientific computing*. 2007: Cambridge university press.

135. Madsen, M.T., *A simplified formulation of the gamma variate function.* Physics in Medicine and Biology, 1992. **37**(7): p. 1597.

136. Espiratory, R., *Predictive Respiratory Gating: A New Method to Reduce Motion Artifacts on CT Scans'*. Radiology, 1994. **190**: p. 847-852.

137. Mageras, G.S. and E. Yorke. *Deep inspiration breath hold and respiratory gating strategies for reducing organ motion in radiation treatment*. in *Seminars in radiation oncology*. 2004. Elsevier.

138. Sonke, J.-J., et al., *Respiratory correlated cone beam CT.* Medical physics, 2005. **32**: p. 1176.

139. Achenbach, S., et al., *Noninvasive coronary angiography by retrospectively ECG-gated multislice spiral CT.* Circulation, 2000. **102**(23): p. 2823-2828.

140. Hong, C., et al., *ECG-gated Reconstructed Multi–Detector Row CT Coronary Angiography: Effect of Varying Trigger Delay on Image Quality1.* Radiology, 2001. **220**(3): p. 712-717.

141. Shuman, W.P., et al., *Prospective versus retrospective ECG gating for 64-detector CT of the coronary arteries: comparison of image quality and patient radiation dose1.* Radiology, 2008. **248**(2): p. 431-437.

142. Macovski, A., *Medical imaging systems*. Vol. 20. 1983: Prentice-Hall Englewood Cliffs, NJ.

143. Ma, J., et al., *Variance analysis of x-ray CT sinograms in the presence of electronic noise background.* Med Phys, 2012. **39**(7): p. 4051-65.

144. Wu, M. and J.A. Fessler. *GPU acceleration of 3D forward and backward projection using separable footprints for X-ray CT image reconstruction*. in *Proc. Intl. Mtg. on Fully 3D Image Recon. in Rad. and Nuc. Med*. 2011.

Biography

Yuan Lin

Personal

- Born on March 7th, 1982 in Longkou, Shandong Province, China

Education

- PhD in Physics (expected), Duke University, Durham, NC, 2008 - 2014
- M.S. in Physics, Chinese Academy of Sciences, Beijing, China, 2005 - 2008
- B.S. in Applied Mathematics, Shandong University, Jinan, Shandong Province, China, 2001 – 2005

Journal Papers

1. **Y Lin** and E Samei, *A Segmentation-free Poly-energetic Dynamic CT Perfusion Imaging Algorithm (pDP)*, submitted to Med. Phys., 2014.
2. **Y Lin**, K Choudhury, et al, *Validation of An Image-based Technique to Assess the Perceptual Quality of Clinical Chest Radiographs with An Observer Study*, submitted to Med. Phys., 2014.
3. **Y Lin**, JC Ramirezb, et al, *An Angle-dependent Reconstruction Technique of X-ray Spectrum from Rotational Transmission Measurement of Clinical CT Systems*, Med. Phys., 2014 (in press).
4. N Kiarashia, **Y Lin**, et al, *Development and Application of a Suite of Dynamic 4D Breast Phantoms for Optimization and Evaluation of Contrast-based Breast Imaging Systems*, IEEE transactions on medical imaging, March 2014 (in press).
5. **Y Lin** and E Samei, *A Fast Poly-energetic Iterative FBP Algorithm (piFBP)*, Phys. Med. Biol., 2014. 59(7): p. 1655.

6. **Y Lin** and E Samei, *An Efficient Poly-energetic SART Reconstruction Algorithm for Quantitative Myocardial CT Perfusion (pSART)*, Med. Phys., 2014. 41(2): p. 021911.

7. **Y Lin** and H Luo, *An Image-based Technique to Assess the Perceptual Quality of Clinical Chest Radiographs*, Med. Phys., 39(11):7019-31, Nov 2012.

8. F Zhan, **Y Lin**, and B Wu, *Equivalence of Two Approaches for Quantum-classical Hybrid Systems*, J. Chem. Phys. 128, 204104, May 2008.

9. GS Jin, **Y Lin**, and B Wu, *Generating Multi-photon Greenberger-Horne-Zeilinger States with Weak Cross-Kerr Nonlinearity*, Phys. Rev. A 75, 054302, May 2007.

10. **Y Lin** and B Wu, *Ground State of Hard-Core Bosons in One-dimensional Periodic Potentials*, Phys. Rev. A 75, 023613, Feb 2007.

Conference Papers

1. **Y Lin**, K Choudhury, et al, *Validation of An Image-based Technique to Assess the Perceptual Quality of Clinical Chest Radiographs with An Observer Study*, submitted to Proc. SPIE 2014.

2. R Mahadevan, LC Ikejimba, **Y Lin**, et al, *A Task-based Comparison of Two Reconstruction Algorithms for Digital Breast Tomosynthesis*, submitted to Proc. SPIE 2014.

3. JB Solomon, JC Giraldo, **Y Lin**, *Towards Virtual Clinical Trials: A Framework for Clinically Relevant CT Simulations*, RSNA 2013.

4. **Y Lin**, S Ghate, et al., *3D Biopsy for Tomosynthesis: Simulation of Prior Information Based Reconstruction for Dose and Artifact Reduction*, Proc. SPIE 8313, Medical Imaging, 2012.

5. N Kiarashi, **Y Lin**, et al., *Development of a Dynamic 4D Anthropomorphic Breast Phantom for Contrast-based Breast Imaging*, Proc. SPIE 8313, Medical Imaging, 2012.

6. L Ikejimba, N Kiarashi, **Y Lin**, et al., *Task-based Strategy for Optimized Contrast Enhanced Breast Imaging: Analysis of Six Imaging Techniques for Mammography and Tomosynthesis*, Proc. SPIE 8313, Medical Imaging, 2012.

7. **Y Lin**, E Samei, *A Patient Image-based Technique to Assess the Image Quality of Clinical Chest Radiographs*, Proc. SPIE 7961, Medical Imaging, 2011.

8. **Y Lin**, X Wang, et al, *Quantification of Radiographic Image Quality Based on Patient Anatomical Contrast-to-noise Ratio: A Preliminary Study with Chest Images*, Proc. SPIE 7627, Medical Imaging, 2010.

9. **Y Lin** and B Wu, *Ground State of Hard-core Bosons in One-dimensional Periodic Potentials*, National Youth Symposium of Cold Atom and Quantum Information, 2007.

Patents

1. **Y Lin** and E Samei, *Quantitative Poly-energetic Reconstruction Schemes for Single Spectrum CT Scanners*, under processing at Office of Licensing & Ventures of Duke University, Case Number 4343, 2014.

2. **Y Lin** and E Samei, *An Angle-dependent Reconstruction Technique of X-ray Spectrum from Rotational Transmission Measurement of Clinical CT Systems*, under processing at Office of Licensing & Ventures of Duke University, Case Number 4344, 2014.